Theoretical study of developmental robustness: From gene network to cell community

(発生現象のロバストネスに関する理論的研究：
遺伝子ネットワークから細胞集団まで)

中島　昭彦

Publication list

[1] Akihiko Nakajima, Kunihiko Kaneko, Regulative differentiation as bifurcation of interacting cell population, *Journal of Theoretical Biology*, **253**, 779-787 (2008).

[2] Akihiko Nakajima, Takako Isshiki, Kunihiko Kaneko, Shuji Ishihara, Robustness under functional constraint: The genetic network for temporal expression in Drosophila neurogenesis, *submitted to Plos Computational Biology*.

[3] Akihiko Nakajima, Shuji Ishihara, Dynamics of the Cellular Potts Model Revisited: Relevance of the active cell movements to cell sorting, *in preparation*.

[4] Akihiko Nakajima, Shuji Ishihara, Analysis of the domain-growth kinetics of the Cellular Potts Model, *in preparation*.

Table of contents

Chapter 1

Introduction

Biological systems have fascinated scientists over many years. Their complexity has attracted not only biologists but also many physicists and mathematicians.

In the last decade, new attempts to understand biological systems have emerged. By combining experimental data and computational and theoretical analysis, scientists are trying to understand the system-level properties of biological systems. Through these attempts, several concepts have been proposed regarding the characteristics of biological systems. Among these is the concept of "robustness" [10,94,193] (basic concept dating back to [192]). The basic idea of the robustness can be summarized as follows:

- Neutrality of the phenotype against genotypic change
- Structural stability of dynamical systems

The meaning of "genotype" here depends on the subjects. They may correspond to the amino-acid (or DNA) sequence for protein folding or the architecture of molecular networks for signal transduction, pattern formation in development, etc. Structural stability is a property of dynamical systems, such as population dynamics of ecological systems and chemical oscillation, where they qualitatively show the same behavior against some parameter changes. The above two categorizations are not completely independent; they are both related to the insensitivity of the system against disturbances. These aspects of robustness discussed thus far are from a static point of view.

Among a variety of phenomena in the biological systems, multicellular development is a fascinating process where a fertilized egg gives rise to a complex organism. How can we understand the robust properties of this elaborate process? This is the underlying theme of this thesis.

Compared to the properties of unicellular organisms, additional new aspects arise for developmental systems. Developmental systems organize the sophisticated multicellular structures though pattern formation, growth-and-differentiation, and morphogenesis. For pattern formation and differentiation, cells have to coordinate their behaviors (cellular decisions) with other constituent cells. Hence, intercellular interactions should be incorporated in addition to intra-cellular dynamics governed by gene regulation networks. Moreover for morphogenetic processes, the dynamics and collective behaviors of cells are important and should be considered. Since morphogenesis is a highly dynamic process in space and time, to understand robust development, we need to go further from the static view of robustness to discuss its dynamical mechanisms via mutual interactions and dynamic and collective behaviors of cells and tissues.

Organization of this thesis

This thesis is organized as follows: We begin by studying the temporal expression patterning of neural stem cells in *Drosophila* neurogenesis (chapter 2). Similar to the formation of static spatial patterns, the study of robustness based on networks is necessary to understand the dynamic temporal patterning process in development. Here we show that the network architecture of the *Drosophila* temporal patterning network is organized to be optimal for the temporal sequential expression to be robust. From this study, we shown that the statistical view of robustness can be applied to this dynamical expression patterning in development.

In chapters 3 and 4, we go further from the static view of robustness to a more dynamic-based approach: in chapter 3, we study the robust differentiation strategy via intercellular signaling and in chapter 4, we raise the possibility of the importance of collective cellular motion in robust development. We selected a simple system, cell sorting process, which is considered as a basic mechanism employed in cells, for instance, in tissue boundary formation and segregation of different types of cells. By analyzing the kinetics of the cell-sorting process, we suggest the importance of a collective cellular movement for fast and robust cell segregation. We conclude the thesis by providing a brief summary of the results in Chapter 5.

Chapter 2

Robust temporal expression in *Drosophila* neurogenesis

2.1 Introduction

2.1.1 Temporal gene expression of *Drosophila* neuroblasts

Precise coordination of cell fate decisions is crucial in the development of multicellular organisms. In the developmental processes, where a series of events occurs at a specific place and time, gene regulatory networks are responsible for implementing the reliable biological functions [5, 102]. In order to obtain the system-level understanding of the processes, it is necessary to integrate the molecular machinery of each regulation with the architecture and dynamics at the regulatory network level. Biological functions achieved by gene networks are generally expected to possess robustness, i.e., insensitivity of system properties against a variety of perturbations that may be originated from fluctuations during development and mutations through evolution. Recent investigations have addressed the questions on how robust functions in gene or signaling networks are achieved through underlying network architecture and its dynamical properties [10, 29, 86, 103, 193]. An illustrative example in developmental systems on this subject is segmentation of *Drosophila* melanogaster, which has been studied both experimentally and theoretically [2, 142, 164]. The requisite regulations or architecture of this system have been discussed from the point of network level description [46, 76, 80, 142, 179], and it is suggested that the underlying gene network is designed to perform the process in a robust manner [74, 113, 191].

Besides spatial patterning, temporal patterning also plays important roles in

various developmental processes [22, 140, 183]. One of the most studied systems is the development of the *Drosophila* central nervous system (CNS), in which the sequential expression of genes coordinates cell-fate decisions. The neural stem cells called neuroblasts (NBs) express a series of transcription factors in a definite order: Hunchback (Hb), Krüppel (Kr), Pdm1/Pdm2 (Pdm), and Castor (Cas) [57, 79, 83, 134] (Fig. 2.1A to C). In addition, the fifth factor Seven-up (Svp) is expressed in the time window between Hb and Kr expression [84]. In association with this sequential expression, NBs divide asymmetrically to bud off a series of ganglion mother cells (GMCs). Each GMC undergoes an additional division to generate typically two postmitotic neurons. The sequentially expressed transcription factors in NBs control temporal specification of cell fate of neurons, thereby establishing the diversity of cell types in the *Drosophila* CNS.

Isolated NBs exhibit sequential expression in vitro and differentiate into various neurons in the same manner as in vivo [19, 56]. Hb expression is switched off by Svp in a mitosis-dependent manner, while the subsequent expression of Kr, Pdm and Cas proceeds in a mitosis-independent manner [84, 119]. These observations suggest that sequential expression of the genes is regulated cell-autonomously and occurs through mutual interactions among the factors.

In this study, we addressed the robustness of the gene network for sequential expression in the *Drosophila* CNS. One of the promising approaches to characterize robustness of biological systems is to compare the actual network with other possible network architectures with respect to function and robustness. Wagner considered how network architecture and robustness are related by studying circadian oscillation networks [193], although these networks lack the direct biological counterpart. Ma *et al.* studied the architecture of the *Drosophila* segmentation network [109], in which they had to arbitrarily eliminate components to reduce the size of the entire network. From theoretical and computational points of view, one advantage of studying temporal patterning in the *Drosophila* CNS is that the number of system components is so small that we can perform a comprehensive analysis of network architecture without any loss of biological relevance.

First, we explored the conditions necessary for gene regulatory networks to reproduce the observed expression patterns in both wild type (WT) and mutants. We did not confine ourselves to only known regulations for sequential expression, but rather searched all possible networks that could reproduce the observed expression patterns. Studying the common structure of the specified genetic networks, we detect requisite regulations and predict an unknown factor to reproduce known expression profiles. Second, we compared these functional networks with the actual *Drosophila* network in terms of network architecture and robustness of the

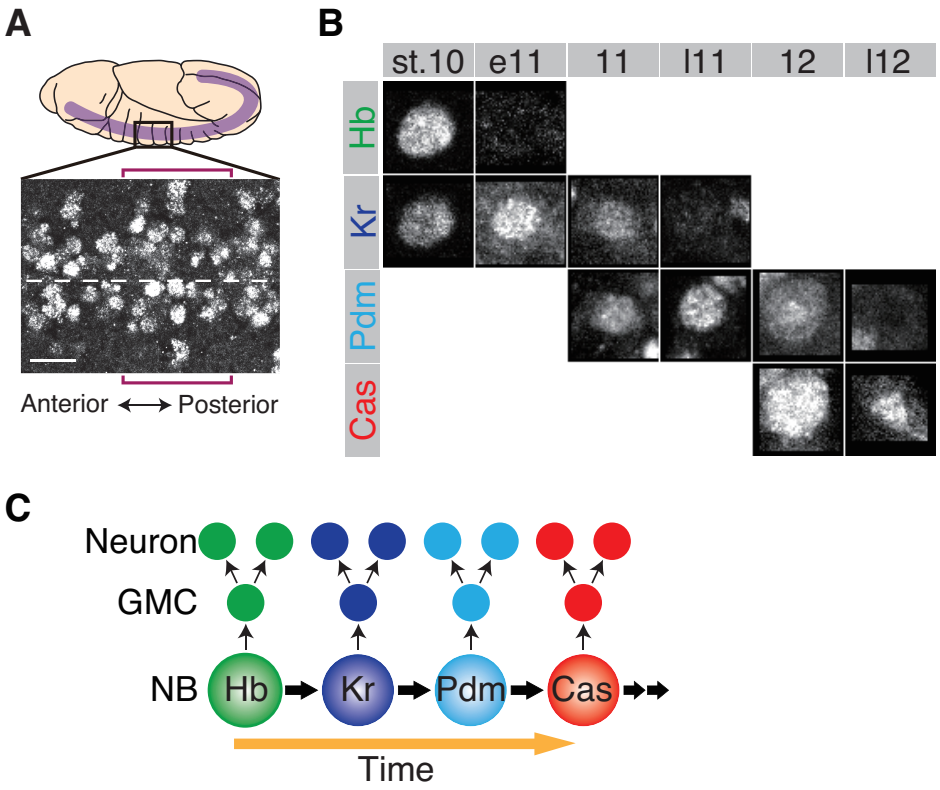

Figure 2.1: Sequential expression of temporal transcription factors within neuroblasts in the *Drosophila* CNS. (A) The relative position of neuroblasts (NBs) in *Drosophila* embryo. The picture is the ventral view of NBs and shows Cas expression in the NBs at developmental stage 12. The bracket indicates a single segment. Dashed line corresponds midline. Scale bar: $40\mu m$. (B) The expression levels of Hb, Kr, Pdm, and Cas in a single NB (NB 2-4 lineage) are shown from the developmental stage 10 to 12: early stage 10 (st. 10); early stage 11 (e11); mid stage 11 (11); late stage 11 (l11); mid stage 12 (12); late stage 12 (l12). (C) Schematic representation of the change of the expression pattern in a single NB. A part of the pictures in (B) are reprinted from [79]. The Other pictures are courtesy of Dr. Isshiki.

expression pattern. We found that the *Drosophila* network is highly robust and stable among possible functional networks. We discuss how the architecture of the *Drosophila* network implements robustness of sequential expression against both cell-to-cell variations and intracellular fluctuations.

2.2 Network architecture necessary for temporal patterning

2.2.1 Temporal patterning network of *Drosophila* neuroblasts

Experimentally reported expression profiles of the temporal transcription factors are summarized in Figure 2.2A for WT, loss-of-function, and overexpression embryos [30, 56, 57, 79, 84, 185]. These sequential expressions are considered to be produced (or at least modulated) by mutual regulations among the temporal transcription factors [79, 83]. We reconstructed the gene network for sequential expression in *Drosophila* NBs from the literature as shown in Figure 2.2B and C (for references, see Table 2.1).

2.2.2 Modeling gene network dynamics by Boolean description

First, we considered the necessary conditions for the network architecture to reproduce the sequential expression patterns of both WT and mutants. To investigate gene expression dynamics, we adopted a Boolean-type model [103] (see Appendix for details of the model and the following analysis),

$$X_i^{t+1} = f_i(\{X_j^t\}) = \begin{cases} 1 & (\sum_j J_{ij} X_j^t > 0) \\ 0 & (\sum_j J_{ij} X_j^t < 0) \\ \theta_i & (\sum_j J_{ij} X_j^t = 0) \end{cases}, \tag{2.1}$$

where represents the expression state of gene *i* ($i \in$ *hb*, *Kr*, *pdm*, *cas*) at the t-th time step and takes either 1 (ON) or 0 (OFF). Regulation from gene *j* to gene *i* is either positive ($J_{ij} > 0$), negative ($J_{ij} < 0$), or zero ($J_{ij} = 0$), which corresponds to activation, repression, or absence of regulation, respectively. The state of gene *i* at the next step (X_i^{t+1}) is 1 when the sum of the regulatory inputs is positive ($\sum_j J_{ij} X_j^t > 0$) or 0 when the sum is negative ($\sum_j J_{ij} X_j^t < 0$). When the sum equals zero ($\sum_j J_{ij} X_j^t = 0$), X_i^{t+1} takes the default expression state of the gene θ_i: $\theta_i \in \{0, 1\}$. In this study, the value of J_{ij} is supposed to take one of the discrete

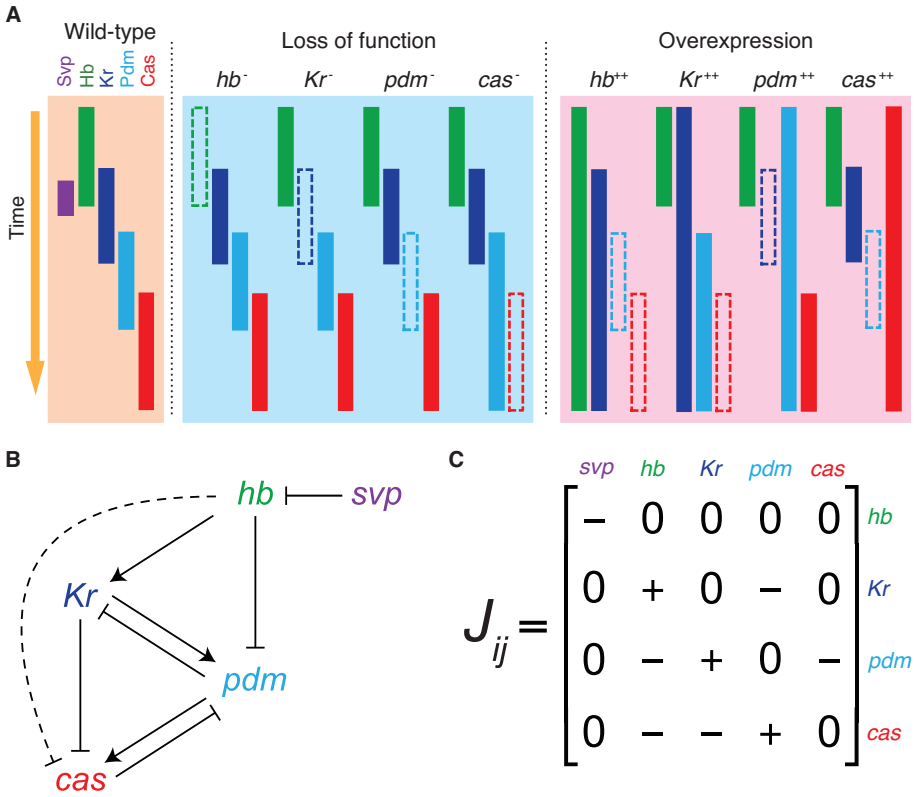

Figure 2.2: Sequential expression of temporal transcription factors within neuroblasts in the *Drosophila* CNS. (A) The expression profiles of WT, loss-of-function and overexpression mutants of the genes observed in the experiments (for references, see Table 2.2). (B) Reconstructed genetic network for sequential expression in *Drosophila* NBs. Repression from *hb* to *cas* (dashed line) was suggested to exist [57], although there is no direct verification. When the *Drosophila* network is invoked in this article, this regulation is also included. (C) Matrix representation of the *Drosophila* network.

Regulation		**References**
Activation	$hb \rightarrow Kr$	[79]
	$Kr \rightarrow pdm$	[79]
	$pdm \rightarrow cas$	[57]
Repression	$hb \rightarrow pdm$	[79, 83]
	$hb \rightarrow cas$	[57]
	$Kr \rightarrow cas$	[79]
	$pdm \rightarrow Kr$	[57]
	$cas \rightarrow pdm$	[57, 83]
	$svp \rightarrow hb$	[84, 119]

Table 2.1: List of the regulatory interactions of the genes in the NB temporal patterning network

Genotype	**References**
wt	[79, 84]
hb^-	[56, 79]
Kr^-	[79]
pdm^-	[57, 185]
cas^-	[57, 185]
hb o.e.[1]	[79]
Kr o.e.	[30, 79]
pdm o.e.	[57, 185]
cas o.e.	[57, 185]

1. o.e.: over expression

Table 2.2: List of references for the sequential expression pattern in the wild type and mutants of the genes in the NB temporal patterning network

values $J_{ij} \in \{1, 0, -5\}$. A large negative value of J_{ij} signifies that the expression of a gene is completely shut off in the presence of a repressor. Initial states of the genes are set to 0 except for Hb, which emulates the expression state of NBs in the first stage of the sequential expression [79, 83]. Thus far, the only known function of Svp during the early stage is downregulation of Hb. There is no evidence that Svp regulates or is regulated by other temporal transcription factors during the expression series: Kr $\rightarrow$ Pdm $\rightarrow$ Cas [84]. In addition, Hb is only regulated by Svp and not by the other three factors (Kr, Pdm, and Cas). Thus, in the model, we assumed a pulsed expression of Svp as an input to the system, resulting in downregulation of Hb at the next time step. The temporal expression dynamics of Kr, Pdm, and Cas follow Eq. (2.1) with assigned values of J_{ij} (Fig. 2.2C).

2.2.3 Search of temporal patterning networks

The regulatory networks of known factors do not reproduce the experiments

Based on above formulation, we investigated whether the reconstructed *Drosophila* gene network (Fig. 2.2B and C) is enough to reproduce the sequential expression observed in WT, as well as all of the known single loss-of-function and overexpression mutants: *hb*$^{-}$, *Kr*$^{-}$, *pdm*$^{-}$, *cas*$^{-}$, *hb*$^{++}$, *Kr*$^{++}$, *pdm*$^{++}$, and *cas*$^{++}$ (here, "++" means overexpression of the gene) (Fig. 2.2A, Table 2.2). At the moment, we cannot specify the values of the parameters θ_{Kr}, θ_{pdm}, and θ_{cas} from empirical data, thus each value could be arbitrarily chosen from $\theta_i \in \{0, 1\}$ ($i \in \{$*Kr*, *pdm*, *cas*$\}$). We studied all 2^3 combinations of $\{\theta_i\}$ and found that the dynamics coincide with the expression profile in WT, but do not in some of the mutants for each choice of the parameters (examples shown in Fig. 2.3). Depending on the parameter values, the expression dynamics changed to some extent, but none of the possible combinations reproduced the expression profiles of all of the mutants. For example, in the case of $\theta_{Kr} = 0$, $\theta_{pdm} = 0$, and $\theta_{cas} = 1$, the dynamics of the network for *hb*$^{-}$ and *Kr*$^{-}$ did not agree with the experiments (Fig. 2.3A), while in the case of $\theta_{Kr} = 1$, $\theta_{pdm} = 1$, and $\theta_{cas} = 1$, the dynamics of *hb*$^{-}$ and *pdm*$^{-}$ did not (Fig. 2.3C).

We then investigated whether other networks than the *Drosophila* network can reproduce the observed expression profiles by checking all the 3^{12} $(= 531,441)$ combinations of J_{ij} values. The dynamics agreed with the expression sequence in WT for a large number of networks ($39,391$ out of $531,441$), but any networks composed of *hb*, *Kr*, *pdm*, *cas*, and *svp* did not reproduce the expression in both WT and mutants.

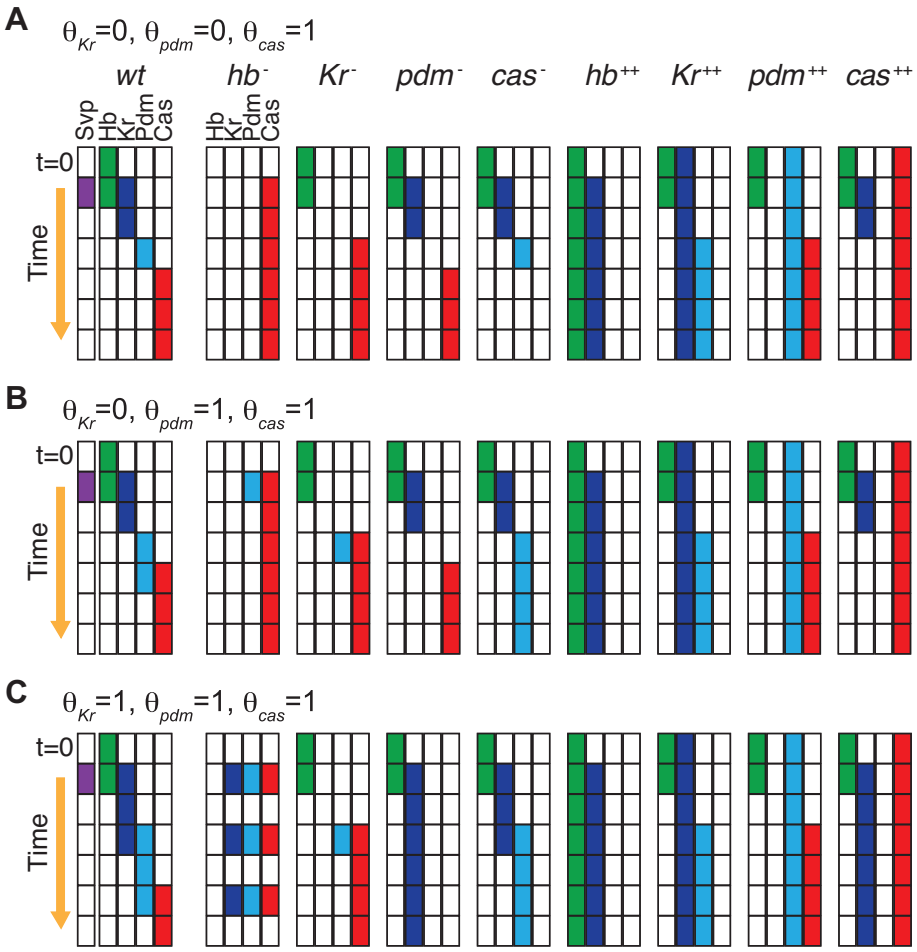

Figure 2.3: The reconstructed *Drosophila* network cannot reproduce the experimentally reported expression profiles. Sequential gene expression of reconstructed *Drosophila* network is simulated using Boolean model. The grids filled with colors represent ON states of the genes. The dynamics could be different depending on the choice of the default expression states . (A) $\theta_{Kr} = 0$, $\theta_{pdm} = 0$, and $\theta_{cas} = 1$, (B) $\theta_{Kr} = 0$, $\theta_{pdm} = 1$, and $\theta_{cas} = 1$, and (C) $\theta_{Kr} = 1$, $\theta_{pdm} = 1$, and $\theta_{cas} = 1$.

Introduction of a presumptive factor is sufficient to reproduce the expression profiles

Preceding results indicate the difficulty of reproducing the observed expression patterns only with known constituents. We therefore introduced an additional presumptive regulator (x). The expression state of *x* was assumed to start in the ON state and change into OFF, or *vice versa* at $t = \tau_{switch}$ ($0 \leq \tau_{switch} \leq \tau_{end}$) (see Appendix). Including this assumption we reinvestigated the dynamics of all 3^{15} ($= 14,348,907$) possible regulatory networks with all the possible switching timing of *x*. In the case that the expression of *x* switches OFF to ON, none of the networks conformed to the expected expression profiles. On the other hand, in the case that the expression of *x* switches ON to OFF, we found that 384 networks ($< 0.003\%$) reproduced the expression profiles of both WT and mutants. We refer to the detected networks as "the functional networks" in the rest of this study.

We compared the network architectures and found that the regulations shared among all the functional networks are coincident with experimentally verified regulations (colored as black in Fig. 2.4A). In addition, activation of *Kr* and repression of *cas* by a presumptive factor *x* appear in all of the functional networks (colored as brown in Fig. 2.4A). Therefore, we conclude that the genetic network composed of these common regulations is a minimum network that is necessary and sufficient to reproduce the expression profiles of WT and mutants.

To quantify the similarity among the functional networks, we measured the distances of the 384 functional networks from the actual *Drosophila* network (Fig. 2.5); The distances are defined by the number of different regulations (see Appendix). As a reference, we also performed the same analyses of distance measurement for all possible networks and the networks that are randomly reconnected from functional networks (see Appendix). For all possible networks, the frequency distribution of the distances shows that the network architectures are different from the actual *Drosophila* network by 7.8 ± 1.5 regulations. The reconnected networks yield similar results albeit with slightly decreased distances (7.0 ± 1.7 regulations). In contrast, the architectures of the functional networks differ by only 2.4 ± 1.1 regulations. The architectures of the functional networks resemble that of the actual *Drosophila* network. These indicate the gene networks that reproduce the known sequential expression patterns are highly constrained in their topologies.

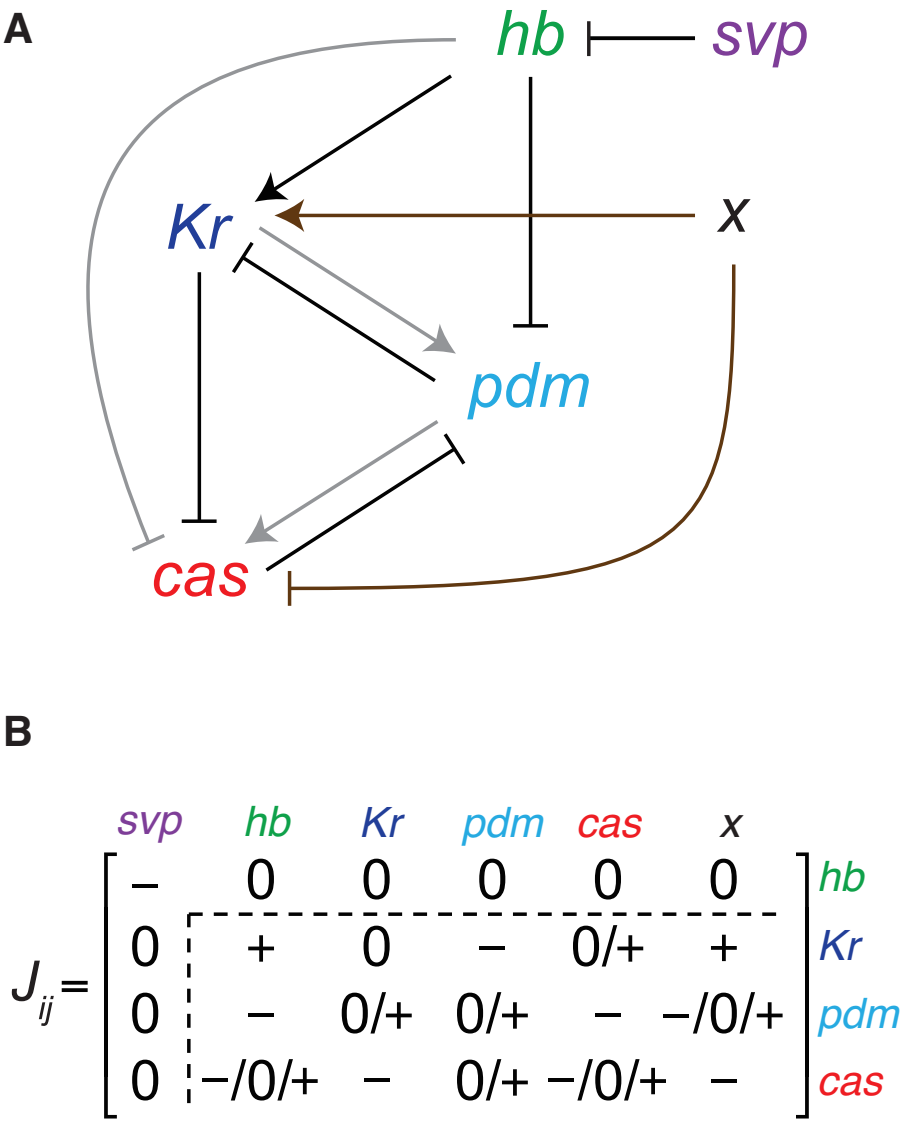

Figure 2.4: Architecture of the detected functional networks. (A) Architecture of the functional networks reproducing the gene expression sequences observed in the experiments. The black arrows are the regulations that appear in all the functional networks. The brown arrows are the regulations from the presumptive factor x that also appear in all the functional networks. The other regulations existing in the actual *Drosophila* network are shown by gray arrows. (B) Matrix representation of the functional networks. Elements of J_{ij} are shown as either $+$ for activation, $-$ for repression, or 0 for the absence of regulation.

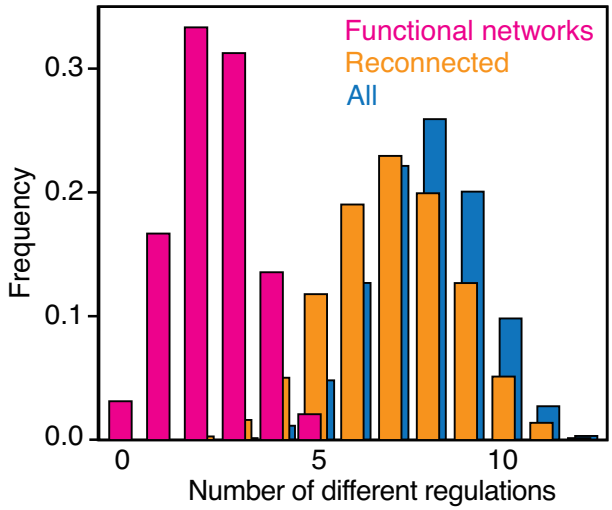

Figure 2.5: Frequency distributions of the distances of networks from the *Drosophila* network. The distributions are drawn from the functional networks ($N = 384$; magenta), all the possible networks ($N = 14,348,907$; blue), and the networks randomly reconnected from the functional ones ($N = 38,400$; yellow). From each of the functional networks, 100 reconnected networks were generated. The regulatory interactions from x and positive self-feedbacks are neglected in counting the number of different regulations.

2.3 Robustness of the temporal patterning networks

2.3.1 Robustness of the *Drosophila* network

Since there are multiple network architectures that explain the observed expression profiles as shown above, we then ask the characteristics of the actual *Drosophila* network among the functional networks. From the biological point of view, the sequential expression in NBs should proceed reliably despite developmental disturbances such as cell-to-cell variation and intracellular fluctuations. We thus evaluated the stability of sequential expression for each of the detected functional networks and compared the properties of the actual *Drosophila* network to those of the other networks. To address the problem quantitatively, we extended the previous Boolean-model into a model of ordinary differential equations with fluctuations in gene expression, where the concentrations of mRNAs $M_i(t)$ and proteins $P_i(t)$ obey the following equations [116, 170] (see Appendix for the details of the model and the following analysis):

$$\frac{dM_i(t)}{dt} = \gamma_M \left[F_i(\{P_j(t)\}) - M_j(t)\right] + \xi_i(t), \tag{2.2}$$

$$\frac{dP_i(t)}{dt} = \gamma_P \left[M_i(t) - P_i(t)\right]. \tag{2.3}$$

Here *i* refers to one of each gene: $i \in \{$*hb*, *Kr*, *pdm*, *cas*, *x*$\}$. The variables $\{M_i(t)\}$ and $\{P_i(t)\}$ take continuous values, unlike the previous Boolean description. The precise function form of promoter activities $F_i(P_j(t))$ is dependent on the regulatory interactions of the genetic networks $\{\tilde{J}_{ij}\}$ and the default promoter activities $\{S_i\}$, corresponding to the Boolean model. The time-dependent variables $\{\xi_i(t)\}$ represent the noise in promoter activities with intensity σ.

Typical dynamics of the *Drosophila* network are shown in Figure 2.6, where sequential expression of WT is reproduced. The dynamics of the model are largely dependent on the parameter values and the noise intensities, and coincide with the experimental observations only under appropriate conditions. Therefore, such sensitivity to parameter variation is important for the development to proceed under environmental and individual fluctuations.

To characterize sensitivity, we measured the fraction of successes, that is the fraction of the parameter sets that can reproduce the expression profile of WT among all the trials of random parameter assignments [109, 191]. To obtain the effect of parameter variation, we carried out the simulation without stochastic terms in Eq. 2.2 (i.e., $\sigma = 0$). In each network, we repeated the simulations with ran-

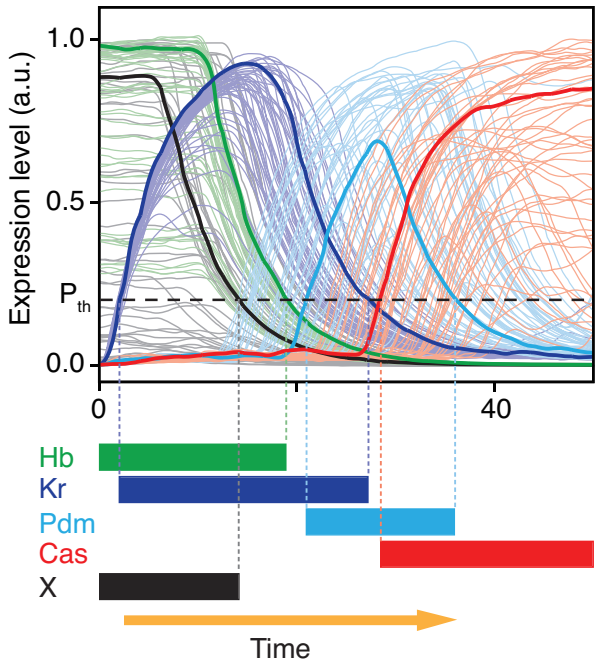

Figure 2.6: Temporal dynamics of the *Drosophila* network in the continuous model. The dynamics of expression levels of proteins $\{P_i(t)\}$ with different parameter values (upper) and discretized representation of a typical temporal dynamics (lower). In addition to the known components of the sequential expression, the presumptive factor x is also incorporated. The expression level of X changes from high level to low as in the previous model. Each gene is considered to be in the ON state when the expression level of the gene is larger than a threshold $P_{\rm th}$. The parameter values of $\{\tilde{J}_{ij}\}$ and $\{S_i\}$ are randomly selected from the following ranges: $|\tilde{J}_{ij}| \in [10^{-1}, 10^{0}]$ for $\tilde{J}_{ij} > 0$, $|\tilde{J}_{ij}| \in [10^{0}, 10^{1}]$ for $\tilde{J}_{ij} < 0$, $S_{hb},\ S_{Kr},\ S_x \in [10^{-2}, 10^{0}]$, and $S_{pdm},\ S_{cas} \in [10^{-1}, 10^{0}]$. Noise intensity is set as $\sigma = 0.05$. The other parameter values are set as shown in Table 2.4.

dom assignment of parameter values and calculated the fraction of successes (Fig. 2.7). The *Drosophila* network scored the highest fraction of successes among the functional networks, and the networks closer to the *Drosophila* network tended to have higher scores.

We also investigated the dynamical stability of the gene networks against fluctuations. In this case, we performed the stochastic simulations in Eq. 2.2 with finite σ. To evaluate stability against noise, we chose the parameter values with which the expression sequence is reproduced in the absence of noise. We then measured the relative fraction of successes under fluctuation. As is shown in Figure 2.8, the fraction of successes under expression noise increased with the similarity to the actual *Drosophila* network as the fraction of successes under parameter variations. Thus, the *Drosophila* network lies at the top level of the functional networks in terms of robustness against these perturbations.

2.3.2 Regulations that heighten functional stability

Because the *Drosophila* network has several additional regulations further to the minimum functional network (gray arrows in Fig. 2.4A), these regulations may be responsible for the robustness shown above. We compared the robustness among the networks with or without the additional regulations. The fraction of successes against parameter variations for these networks are plotted in Figure 2.9A. The minimum network reproduces the sequential expression under the appropriate parameters, but the robustness is much lower than that of the *Drosophila* network. The scores of networks that lack one of the regulations fall between the minimum and the *Drosophila* network. Stability to expression noise was also evaluated by changing noise intensity, and similar results were obtained (Fig. 2.9B). The fraction of successes decreases as the noise intensities get larger, but the effect of noise on the *Drosophila* network is less severe than that on the minimum network. Thus each of these regulations contributes to robustness of the system.

To elucidate the roles of these regulations, we tried $5,000$ random parameter assignments for each of these networks and sampled successful parameter sets that reproduce WT sequential expression profile (Fig. 2.10). In the *Drosophila* network (Fig. 2.10A), wide ranges of parameter values are allowed, indicating that this network reproduces the required profile without quantitative tuning of parameters and thus shows high robustness. For the other networks (Fig. 2.10B to E), the ranges are narrower for some parameters (as clearly seen in S_{pdm} and S_{cas}), and the numbers of successful parameter sets are less than those for the *Drosophila* network.

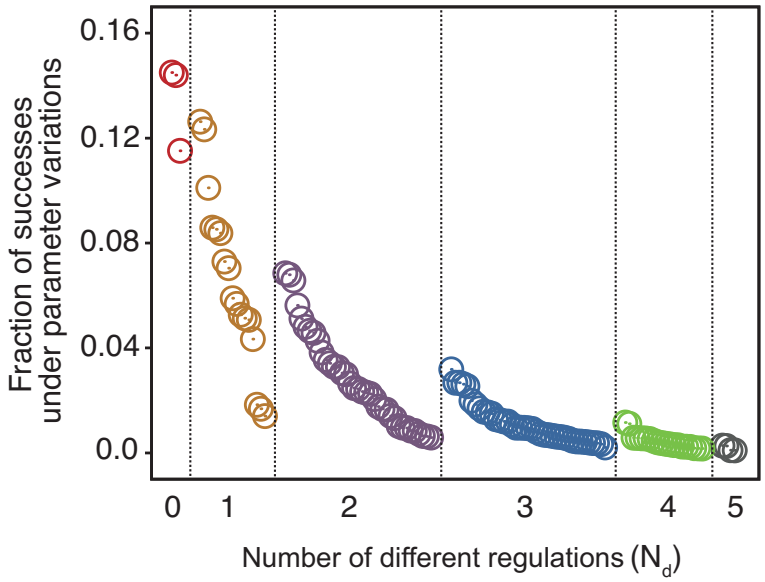

Figure 2.7: The robustness of the gene expression profiles in the functional networks. The fraction of the trials that reproduce the experimental expression profiles against random assignments of parameters. The values of the parameters $\{\tilde{J}_{ij}\}$, $\{S_i\}$, and $\tau_{x,\mathrm{off}}$ are randomly chosen within the ranges shown in Table 2.4. The other fixed parameter values are also listed in Table 2.4. Neglecting the positive self-feedback regulations in the 384 functional networks, 120 networks were chosen and investigated (Appendix). The dynamics were checked for $50,000$ trials in each network. The networks were sorted based on the distance from the *Drosophila* network. Because there are a few possible regulations from the unknown factor x, the networks with $N_d = 0$ exist more than one.

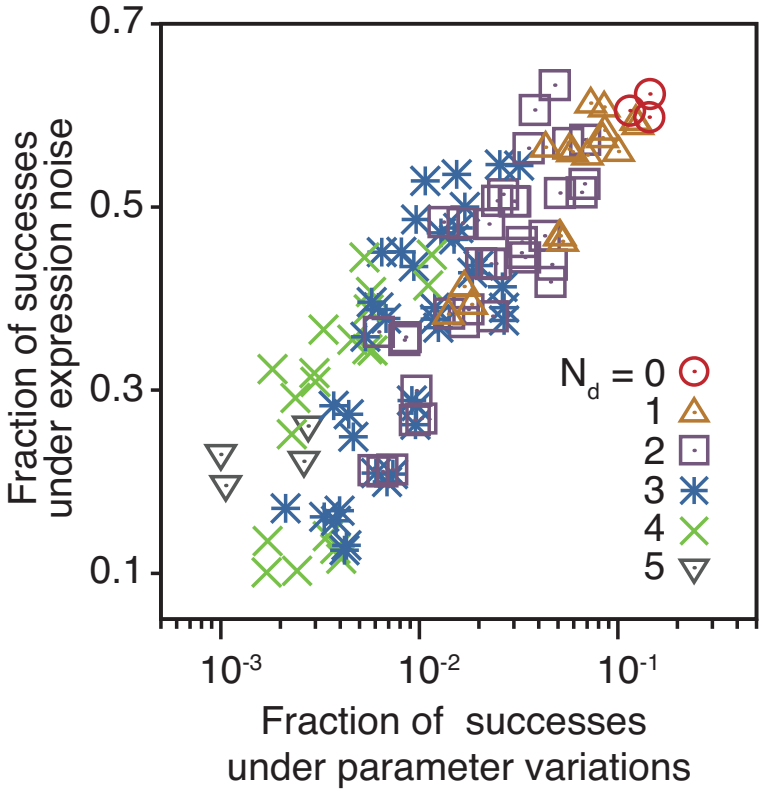

Figure 2.8: The robustness of the gene expression profiles in the functional networks. The fractions of the trials that reproduce the experimental expression sequence under expression noise (vertical axis) are plotted against the fraction of successes against the random parameter assignments. To analyze the stability against the noise in each of the 120 functional networks, we used 1000 different parameter sets with which the expression sequence is reproduced in the absence of noise. The dynamics were checked for 50 trials for each parameter set. Noise intensity is set as $\sigma = 0.05$.

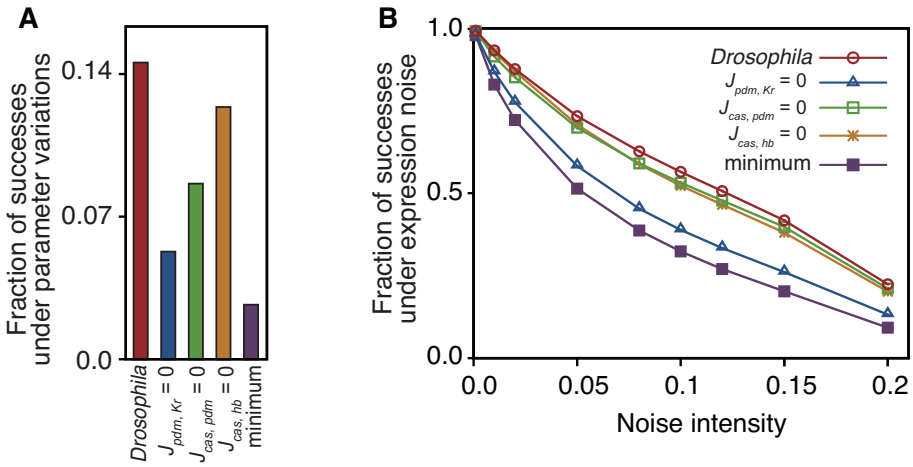

Figure 2.9: Role of the actual regulations for robustness. (A) The fraction of the trials that reproduce the experimental WT expression against parameter variations. The data of Figure 2.7 are replotted for the *Drosophila* network, the networks lacking the indicated regulation (one of the gray arrows in Fig. 2.4A), and the minimum network (black and brown arrows in Fig. 2.4A). (B) The fractions of the trials that reproduce the experimental profile under the gene expression noise with various intensities. We used $5,000$ different parameter sets with which the expression sequence is reproduced in the absence of noise. The dynamics are checked for 50 trials for each parameter set.

How is the robust nature of the *Drosophila* network implemented by these regulations? As seen above, the parameter values of S_{pdm} and S_{cas} (default promoter activities of *pdm* and *cas*) are most influenced by the loss of these regulations. Because expression of a gene is induced by either the default promoter activity or the activators (see Appendix), additional regulations in the *Drosophila* network (gray arrows in Fig. 2.4A) may compensate for the loss of default activities. To verify this possibility, we measured the dependence of the fraction of successes on the strength of regulations ($\tilde{J}_{pdm,Kr}$, $\tilde{J}_{cas,pdm}$, and $\tilde{J}_{cas,pdm}$) and of default promoter activities (S_{pdm} and S_{cas}) (Fig. 2.11).

Fig. 2.11A shows the fraction of successes for random assignments of parameter values under given strengths of $\tilde{J}_{pdm,Kr}$ and S_{pdm}. To score high reproducibility, S_{pdm} must be large for small $\tilde{J}_{pdm,Kr}$, but need not for sufficiently large $\tilde{J}_{pdm,Kr}$. This indicates that activation of *pdm* expression by *Kr* indeed compen-

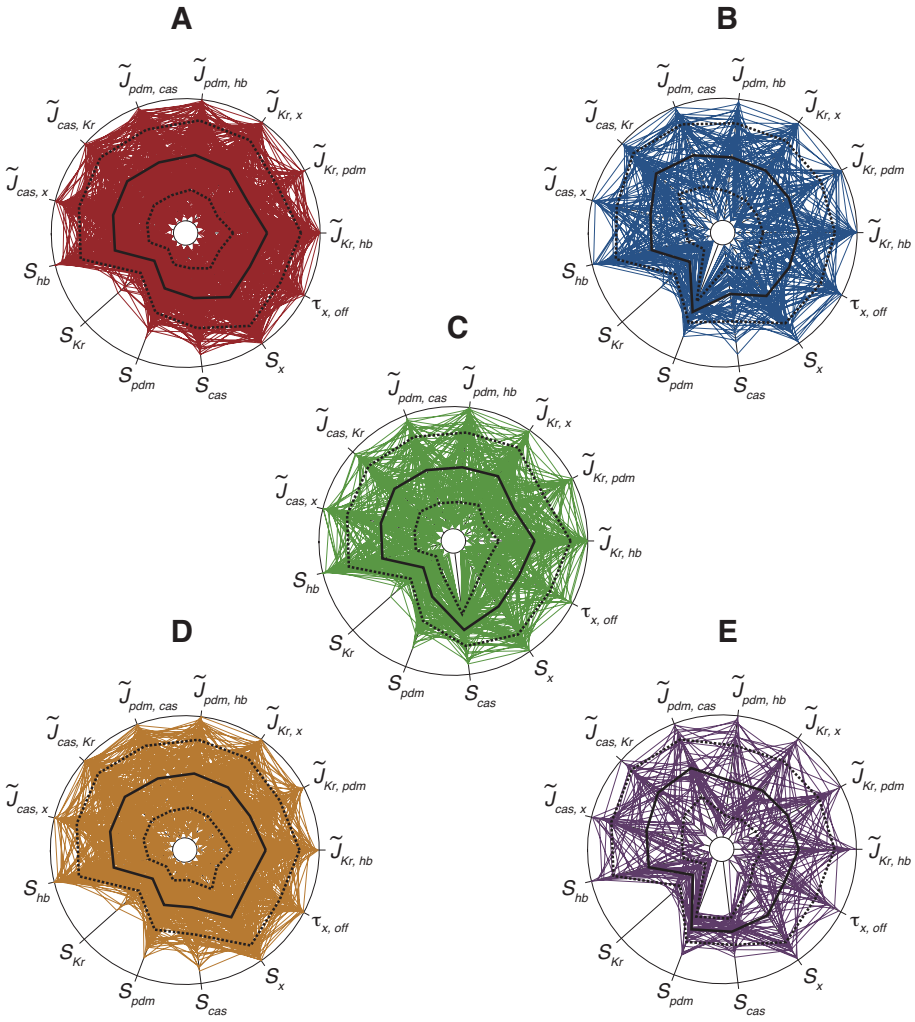

Figure 2.10: Graphical representation of parameter sets with which the WT sequential expression profile is reproduced for (A) the *Drosophila* network, the networks lacking (B) activation from *Kr* to *pdm*, (C) activation from *pdm* to *cas*, (D) repression from *hb* to *cas*, and (E) the minimum network. The parameters involved in minimum network are shown. Each spoke represents a value of indicated parameter between the range used for random parameter assignment (Table 2.4). The value of $\tau_{x,\mathrm{off}}$, is shown by normal scale and those of the other parameters are shown by log scale. Each polygon indicates one parameter set. Solid and broken lines indicate mean and s.d. of obtained parameters. The data are drawn from $5,000$ trials of the random assignment of parameter values.

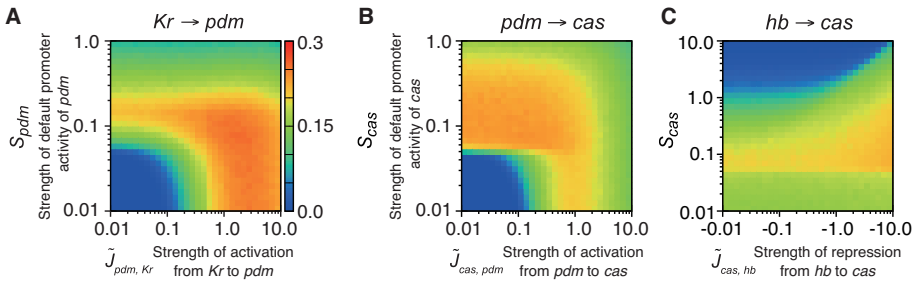

Figure 2.11: The fractions of successes for random assignment of parameter values are plotted under the different strengths of regulations ($\tilde{J}_{pdm,Kr}$, $\tilde{J}_{cas,pdm}$, and $\tilde{J}_{cas,hb}$) and default promoter activities (S_{pdm} and S_{cas}). Dependencies of robustness to (A) $\tilde{J}_{pdm,Kr}$ (strength of activation from *Kr* to *pdm*) and S_{pdm}, (B) $\tilde{J}_{cas,pdm}$ (strength of activation from *pdm* to *cas*) and S_{cas}, and (C) $\tilde{J}_{cas,hb}$ (strength of the repression from *hb* to *cas*) and S_{cas}. The other parameters are set as in Table 2.4. The temporal dynamics were checked for $50,000$ trials.

sates for the loss of default promotor activity of *pdm*. Thus, for the network lacking this regulation, the default promoter activity is necessary because inductions from other factors are absent. A similar relationship is found between $\tilde{J}_{cas,pdm}$ and S_{cas} (Fig. 2.11B).

As for repression of *cas* by *hb*, the role for robustness seems to be different from the above two. When the absolute value of $\tilde{J}_{cas,hb}$ is small, S*cas* must be small to achieve a high fraction of successes (Fig. 2.11C). As $|\tilde{J}_{cas,hb}|$ becomes larger, a higher value of S_{cas} is allowed. This is because the repression from *hb* to *cas* reduces the expression of *cas* in the early stage of sequential expression. Thus the existence of this regulation contributes to the robustness against the parameter variation of S_{cas}. Experimental observation by Grosskortenhaus *et al.* suggested the direct repression from *hb* to *cas* [57], although there is no confirmative evidence to our knowledge. If any, this regulation would contribute to the robustness of the system.

2.4 Discussion

Through the present analyses, we obtained 384 functional networks that reproduce the sequential expression of both WT and mutants. The detected functional networks exhibit high similarity in regulatory interactions among the transcrip-

tion factors (Fig. 2.4 and 2.5). This exemplifies the importance of the regulations in the minimum network for the sequential expression. In addition, the actual *Drosophila* network scores quite high on reproducibility of the WT sequential expression among all the functional networks (Fig. 2.7 and 2.8). Below, we discuss the biological implications of the temporal patterning of *Drosophila* NBs drawn from our numerical analyses.

Two regulatory interactions from a presumptive factor are necessary and sufficient to reproduce the expression patterns of WT and mutants. In this study, we introduced an additional presumptive factor x to obtain the networks that reproduce the expression sequences of both WT and mutants. As x is hypothetical, we discuss its validity here.

Since the loss-of-function mutant of any one gene has only minor effects on the expression sequence (Fig. 2.2A), several previous reports suggested the existence of either unknown regulators or an additional clock mechanism for driving the sequential expression [57, 79]. Our assumption is feasible one for explaining experimental results in that it does not need any clock mechanism or superfluous multiple regulators. It is notable that our analysis indicates that the possible regulations of the presumptive factor are highly restricted; the expression of x switches ON state to OFF (Fig. 2.6), and all the functional networks have activation of *Kr* and repression of *cas* by x (Fig. 2.4A). Thus, our assumption is testable in future experiments in vivo.

We should note that although regulator x is necessary to explain the mutant profiles, the mutual regulations of known factors are sufficient to reproduce the WT sequential expression (Fig. 2.3). Therefore, the regulations among *hb*, *Kr*, *pdm* and *cas* would play a primary role as discussed below.

2.4.1 Minimum network for the sequential expression

An effective way to capture network function is to focus on the specific substructures (network motifs or modules) [5, 46, 74, 76, 77, 109]. Comparing all the functional networks, we detected the minimum structure for the sequential expression, which contains two successive regulatory loops (Fig. 2.4A and 2.12A); one is composed of *hb*, *Kr*, and *pdm*, and the other of *Kr*, *pdm*, and *cas*. In each loop, one gene represses previous and second next factor. The repressions of the second next factors (*hb* to *pdm* and *Kr* to *cas*) define the induction timing of the regulated factors, since they are kept repressed until the regulators are switched off. The feedback repression of the previous factors (*pdm* to *Kr* and *cas* to *pdm*) ensures their downregulation, which promotes the progress of the sequential expression.

These coincide with the observation by Kambadur et al., who showed experimentally that the repressions from *hb* and *cas* define the temporal window of Pdm [83]. These repressive regulations and the activation from *hb* to *Kr* compose the minimum network for sequential expression (Fig. 2.12A). Although they are enough to reproduce the sequential expression under appropriate conditions, the expression profiles could be easily perturbed by the parameter variations or the increase of noise (Fig. 2.9 and 2.12A).

2.4.2 Mechanism generating the precise sequential expression

In the two loops of the *Drosophila* network, the activations from one gene to the next (*Kr* to *pdm* and *pdm* to *cas*) exist in addition to the repressive regulations. Other functional networks do not necessarily have these activations, but the activations can compensate for the loss of default promoter activities (Fig. 2.11A and B). These regulations achieve precise expression by enhancing the correlations among the factors and heightening the stability against fluctuations (Fig. 2.7, 2.8 and 2.9). From these results, we conclude that three different kinds of regulations (the activation of next factor, feedback repression, and repression of second next one) compose a regulatory module for precise temporal expression as summarized in Figure 2.12B. The feature of this network module embodies the robustness of the *Drosophila* network.

Do above discussions have any implications on other developmental processes? In the studies of spatial patterning in *Drosophila* segmentation, it was claimed that the frequent substructure feed forward loop (FFL) can set the positions of expression domains [76], and mutual feedback repressions between the gap genes also have a pivotal role for the formation of expression domains with steep boundaries [77, 80]. In the case of the *Drosophila* network for sequential expression, preceding genes activate the next ones, while these genes repress the preceding ones. Similar regulatory interactions are reported in the yeast cell cycle by Lau et al. [101]. Thus, such asymmetric mutual regulations would be a general mechanism that serves as precise switches in the process of temporal patterning.

2.4.3 Role of the robustness in *Drosophila* neurogenesis

We showed that the *Drosophila* network contains not only the regulations necessary for generating sequential expression, but also additional ones to achieve higher precision in the expression. In each hemisegment of *Drosophila* embryo,

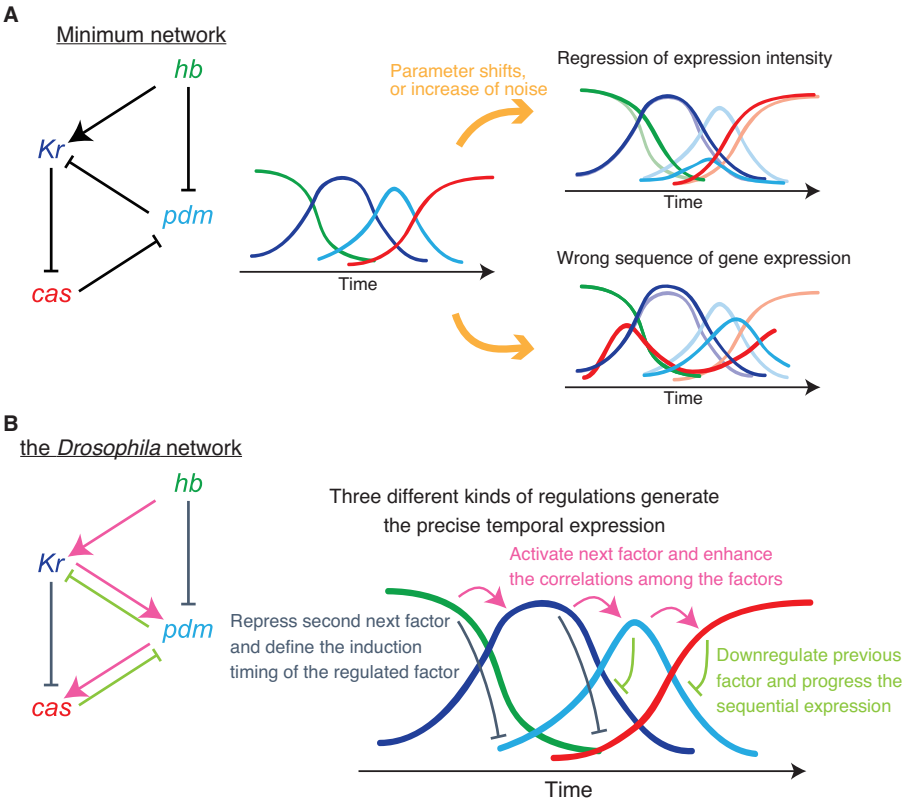

Figure 2.12: Regulatory module for the precise sequential expression. The regulatory interactions and schematic expression profiles of the networks. (A) Regulatory interactions of the minimum network for sequential expression (left). This network reproduces the sequential expression under appropriate conditions (middle). However the parameter variations from the appropriate values and the increase of noise could easily alter the expression profiles (right). (B) Regulatory interactions of the *Drosophila* network (left). Three different kinds of regulations in this network enable the temporal expression in the precise order.

30 different NBs are generated through spatial heterogeneity [181]. To guarantee *Drosophila* NBs sequentially express common temporal transcription factors despite their differences, the robustness of the system may become important.

The robust nature of the *Drosophila* network could be the consequence of evolutionary optimization in the reproducibility of the sequential expression under functional constraint. In future, we expect that experimental manipulation of corresponding enhancers will be able to clarify the relevance of each regulation to the temporal patterning and stability.

2.4.4 Biological relevance of unknown factor

We now discuss expression properties and possible roles of the unknown factor *x*. Since the regulatory interactions and expression timing of *x* are similar to those of *hb* (as we have seen in Fig. 2.4 and 2.6), the existence of *x* might provide a backup for *hb*. In addition, the downregulation of *x* may also be regulated by *svp* in the same way as the expression switch from *hb* to *Kr* regulated by *svp*.

Although the regulator x is needed to explain the mutant profiles under our modeling assumptions, the *Drosophila* temporal network without *x* reproduces the sequential expression in the case of WT. Then, what is the biological function of *x*? The existence of *x* might guarantee the use of the common temporal patterning mechanism over different NBs. Indeed, it is known that some of NBs do not express all of the temporal transcription factors. For example, NB3-3 (number means a specific NB lineage) begins the sequential expression with *Kr*, not *hb*, and thus the expression profile is same as the hb^{-} embryo in Figure 2.2A. In such case, *x* is necessary to generate the temporal expression, as for the temporal expression of mutants.

2.4.5 The architecture of temporal networks in insects

It is known that the spatio-temporal expression patterns in the neurogenesis is similar between *Drosophila* and many other insects [176]. For example, it is known that *hb* expression of NBs is highly conserved in various insects [145], such as grasshoppers *Locusta migratoria* and *Scistocerca Americana* [139], and flour beetle *Tribolium* [195]. *Kr* and *pdm* (or *nubbin*) are also expressed in the CNS of several insects [23, 104, 106]. As our results have shown that the networks reproducing the temporal expressions have many regulations in common, it is possible that *Drosophila* and other insects have similar network architecture

for the temporal gene expression. To verify this possibility, further studies on the NB temporal specification process in insects other than *Drosophila* are necessary.

2.5 Appendix: Materials and methods

2.5.1 Analysis of temporal dynamics with the Boolean model

Here we describe the details of the Boolean model (Eq. 2.1). The expressions of *svp* and *x* occur as inputs to the system. A pulse of *svp* expression always occur at $t = 1$. Expression of *x* switches either from ON to OFF state, or from OFF to ON at $t = \tau_{\mathrm{switch}}$ ($0 \leq \tau_{\mathrm{switch}} \leq \tau_{\mathrm{end}}$). Once we assigned the switching time of *x* expression (τ_{switch}), its value had been fixed through the analysis of expression patterns for all the genotypes. Because the autonomous pulsed expression of *svp* results in *hb* downregulation, we set $J_{hb,svp} = -5$, $J_{hb,j} = 0$ ($j =$ *hb*, *Kr*, *pdm*, *cas*, or *x*), and $J_{k,svp} = 0$ ($k =$ *Kr*, *pdm*, or *cas*) throughout this study. The time step at which we finish the simulation (τ_{end}) was set as $tau_{end} = 12$.

We thus investigated the behaviors of the remaining three factors (*Kr*, *pdm*, and *cas*) under the given regulatory interactions J_{ij}. The total number of combinations of the parameters is $3^M \times 2^3$ (the number of possible network architecture $\{J_{ij}\}$ multiplied by the number of default expression states 2^3), where M is the number of regulations. To simulate the dynamics for mutants, we always set the expression state of the corresponding gene to 0 (OFF) for loss-of-function or 1 (ON) for overexpression. We then examined whether the temporal dynamics of the genetic networks are coincident with the expression profiles of each mutant (Fig. 2.2A and Table 2.3).

2.5.2 Analysis of network statistics

In order to measure the similarity between the functional networks and the actual *Drosophila* network, we used two types of network ensembles as references. One is the ensemble of the possible network architectures. The other is a set of reconnected networks generated from the functional networks by iterative random reconnections of the matrix elements (1000 iterations). The numbers of positive and negative regulations are preserved in the iterations.

To count the number of different regulations between functional networks and the actual *Drosophila* network, we neglected the regulations from *x*, and positive

Genotype	**Criteria for the expression profile**
wt	$\tau_{hb,\mathrm{on(off)}} \leq \tau_{Kr,\mathrm{on(off)}} \leq \tau_{pdm,\mathrm{on(off)}} \leq \tau_{cas,\mathrm{on(off)}}$, $(\tau_{i,\mathrm{on}} \neq \tau_{j,\mathrm{on}}) \cup (\tau_{i,\mathrm{off}} \neq \tau_{j,\mathrm{off}})$
hb^{-}	$\tau_{Kr,\mathrm{on(off)}} \leq \tau_{pdm,\mathrm{on(off)}} \leq \tau_{cas,\mathrm{on(off)}}$, $(\tau_{i,\mathrm{on}} \neq \tau_{j,\mathrm{on}}) \cup (\tau_{i,\mathrm{off}} \neq \tau_{j,\mathrm{off}})$
Kr^{-}	$\tau_{hb,\mathrm{on(off)}} \leq \tau_{pdm,\mathrm{on(off)}} \leq \tau_{cas,\mathrm{on(off)}}$, $(\tau_{i,\mathrm{on}} \neq \tau_{j,\mathrm{on}}) \cup (\tau_{i,\mathrm{off}} \neq \tau_{j,\mathrm{off}})$
pdm^{-}	$\tau_{hb,\mathrm{on(off)}} \leq \tau_{Kr,\mathrm{on(off)}} \leq \tau_{cas,\mathrm{on(off)}}$, $(\tau_{i,\mathrm{on}} \neq \tau_{j,\mathrm{on}}) \cup (\tau_{i,\mathrm{off}} \neq \tau_{j,\mathrm{off}})$
cas^{-}	$\tau_{hb,\mathrm{on(off)}} \leq \tau_{Kr,\mathrm{on(off)}} \leq \tau_{pdm,\mathrm{on(off)}}$, $(\tau_{i,\mathrm{on}} \neq \tau_{j,\mathrm{on}}) \cup (\tau_{i,\mathrm{off}} \neq \tau_{j,\mathrm{off}})$
hb o.e.	$\tau_{hb,\mathrm{on(off)}} \leq \tau_{Kr,\mathrm{on(off)}}$, $(\tau_{i,\mathrm{on}} \neq \tau_{j,\mathrm{on}}) \cup (\tau_{i,\mathrm{off}} \neq \tau_{j,\mathrm{off}})$, $X^t_{pdm} = X^t_{cas} = 0$
Kr o.e.	$\tau_{hb,\mathrm{on(off)}} \leq \tau_{Kr,\mathrm{on(off)}} \leq \tau_{pdm,\mathrm{on(off)}}$, $(\tau_{i,\mathrm{on}} \neq \tau_{j,\mathrm{on}}) \cup (\tau_{i,\mathrm{off}} \neq \tau_{j,\mathrm{off}})$, $X^t_{cas} = 0$
pdm o.e.	$\tau_{hb,\mathrm{on(off)}} \leq \tau_{pdm,\mathrm{on(off)}} \leq \tau_{cas,\mathrm{on(off)}}$, $(\tau_{i,\mathrm{on}} \neq \tau_{j,\mathrm{on}}) \cup (\tau_{i,\mathrm{off}} \neq \tau_{j,\mathrm{off}})$, $X^t_{Kr} = 0$
cas o.e.	$\tau_{hb,\mathrm{on(off)}} \leq \tau_{Kr,\mathrm{on(off)}}$, $(\tau_{i,\mathrm{on}} \neq \tau_{j,\mathrm{on}}) \cup (\tau_{i,\mathrm{off}} \neq \tau_{j,\mathrm{off}})$, $X^t_{pdm} = 0$

Table 2.3: Criterion for expression profile in each genotype

self-feedbacks because the existence of those is uncertain from the experimental data.

2.5.3 Continuous model of the expression dynamics

We introduced the continuous model with stochasticity as shown in Equation 2.2. The promoter activity of gene *i* ($i =$ *hb*, *Kr*, *pdm*, *cas*, or *x*) is described as follows,

$$F_i(P_j(t)) = \frac{\left[g(S_i + \sum_j \tilde{J}_{ij} P_j)\right]^\alpha}{K_M^\alpha + \left[g(S_i + \sum_j \tilde{J}_{ij} P_j)\right]^\alpha} \tag{2.4}$$

Regulatory interactions $\{\tilde{J}_{ij}\}$ are continuous equivalents of $\{J_{ij}\}$ in the Boolean model, and $g(x)$ is a piece-wise linear function such that $g(x) = x$ for $x > 0$, and $g(x) = 0$ for $x < 0$. The parameters $\{S_i\}$ are the default activities of the promoters. Transcription of a gene is induced when the total regulatory inputs become positive ($S_i + \sum_j \tilde{J}_{ij} P_j > 0$), and is suppressed when they become negative ($S_i + \sum_j \tilde{J}_{ij} P_j < 0$). In order to consider the effect of fluctuations on the expression dynamics, we introduced additive white Gaussian noise $\{\xi_i(t)\}$: $\langle \xi_i(t)\xi_j(t')\rangle = \sigma_i^2 \delta_{ij}\delta(t-t')$ (Eq 2.2), where σ_i is the noise intensity of gene *i*.

The expressions of *hb* and *x* are induced only by the default promoter activities because all the regulations are absent for these two ($\{\tilde{J}_{hb,i}\} = \{\tilde{J}_{x,i}\} = 0$). To describe the expression change of *hb* and *x*, the promoter activities of these two are set as $S_{hb} > 0$ for $t < \tau_{hb,\mathrm{off}}$ ($S_x > 0$ for $t < \tau_{x,\mathrm{off}}$), and $S_{hb} = 0$ for $t > \tau_{hb,\mathrm{off}}$ ($S_x = 0$ for $t > \tau_{x,\mathrm{off}}$). The promoter activities of the others are always assumed to exist (S_{Kr}, S_{pdm}, and $S_{cas} > 0$). The noise intensities are also set as $\sigma_i = \sigma$ (> 0) for $t < \tau_{i,\mathrm{off}}$ and $\sigma_i = 0$ for $t > tau_{i,\mathrm{off}}$ ($i =$ *hb*, *x*). Those of the other genes are $\sigma_j = \sigma$ (> 0) ($j =$ *Kr*, *pdm*, *cas*), Here we simply assume that the noise intensities of the genes take the same value σ.

2.5.4 Analysis of the robustness of the networks

For the continuous model, we considered two different types of robustness: the reproducibility of the sequential expression against parameter variations and dynamical stability against temporal fluctuations. To analyze the former, the default promoter activities $\{S_i\}$ were assigned randomly within the defined ranges. The values of the matrix $\{\tilde{J}_{ij}\}$ were set to 0 when the corresponding regulations were absent (The corresponding element of the Boolean model takes as $J_{ij} = 0$) or

assigned randomly when they are present ($J_{ij} \neq 0$). In order to confine our attention to the properties of network architectures, the other parameters (γ_M, γ_P, K_M, and α) were fixed throughout the analysis. The ranges and the fixed values of the parameters are listed in Table 2.4. Robustness against temporal fluctuations is measured as explained in the main text.

To judge whether the dynamics coincide with the expression profile in *Drosophila* NBs, the dynamics of the protein concentrations $\{P_i\}$ were discretized to 1 (0) for $P_i > P_{\rm th}$ ($P_i < P_{\rm th}$). The threshold $P_{\rm th}$ was set as $P_{\rm th} = 0.2$. The temporal dynamics of a network were accepted when the discretized dynamics satisfied the condition for WT in Table 2.3.

In the simulations, we found that the existence of positive self-regulation enhanced the fraction of successes in many cases, but hardly affected the sequential expression. To focus on the contributions of mutual regulations of genes to robustness, we neglected the positive self-feedback regulations and confined the analysis to 120 out of 384 functional networks.

Parameter	**Biological meaning**	**Value**
γ_M	Degradation rate of mRNAs	1.0
γ_P	Degradation rate of proteins	0.2
$\tau_{hb,\text{off}}$	Time for promoter activity of *hb* switched off	10.0
$\tau_{x,\text{off}}$	Time for promoter activity of *x* switched off	$[0.5\tau_{hb,\text{off}},\ 2.0\tau_{hb,\text{off}}]$
K_M	Michaelis constant for the promoter functions	0.1
α	Hill coefficient for the promoter functions	2.0
$\tilde{J}_{ij}$	Strength of regulation from gene *j* to gene *i*	$\lvert\tilde{J}_{ij}\rvert \in [10^{-1},\ 10^{1}]$
S_i	Default promoter activity of gene *i*	$S_{i(\neq hb)} \in [10^{-3},\ 10^{1}]$ $S_{hb} \in [2 \times 10^{-1},\ 10^{1}]$

Table 2.4: Parameter values used for continuous dynamics of the genetic networks

Chapter 3

Regulative differentiation as bifurcation of interacting cell population

In developmental processes, it is often observed that initially homogeneous cells differentiate into a set of distinct types, while the population size of cells and number ratio of cells of different types are often regulated. For such behavior, intercellular interactions are, in many cases, inevitable. We propose a regulatory mechanism of such differentiation, by using a coupled cell model consisting of simple gene expression dynamics. The proposed mechanism is based on self-consistent determination of signal concentration, which works as a bifurcation parameter for differentiation. We show that this consistency between cell and population level leads to robust cell-type determination.

3.1 Introduction

Complex gene and other molecular networks are responsible for determining cellular behaviors. The function of such networks has recently been discussed in the light of specific network structures called network motifs [121, 122, 166]. Besides such motifs, several simple network modules are also considered to operate to give specific dynamical properties such as bistability, adaptation, or oscillatory behavior [39, 165, 187]. Recent experimental results also suggest that such modules provide a basis for cell differentiation, as studied in competence state in *Bacillus subtilis* [110, 177].

In multicellular organisms, several cell states coexist. Morphogenesis with differentiation into distinct cell types, however, is not an event of independent single-cellular dynamics, but occurs as a result of an ensemble of interacting cells. For determining each cell type, cell-cell interactions are often essential besides intra-cellular dynamics by functional modules at a single cell level. In fact, gene regulatory networks responsible for the early developmental process or the cell specification process of several kinds of organisms include many intercellular interactions [32, 34, 73, 107, 178]. Phenomenologically, cell-population level behaviors such as the community effect [58] and differentiation from equivalent groups of cells [55] exemplify the importance of cell-cell interactions to robust developmental processes.

When considering the development of a multi-cellular organism, not only a set of cell types, but also the number distribution of each of the cell types, has to be suitably determined and robust against perturbations during the course of development. For example, the proportion of the body plan in planarian and in the slug of *Dictyostelium discoideum* is preserved over a wide range of body sizes [136, 149]. In the *D. discoideum* slug, the number ratio of two cell types is kept almost constant. In addition, a removal of either of the cell types leads to compensatory transdifferentiation from one cell type to the other (shown in Fig. 3.1). In the hematopoietic system of mammals, approximately ten different cell

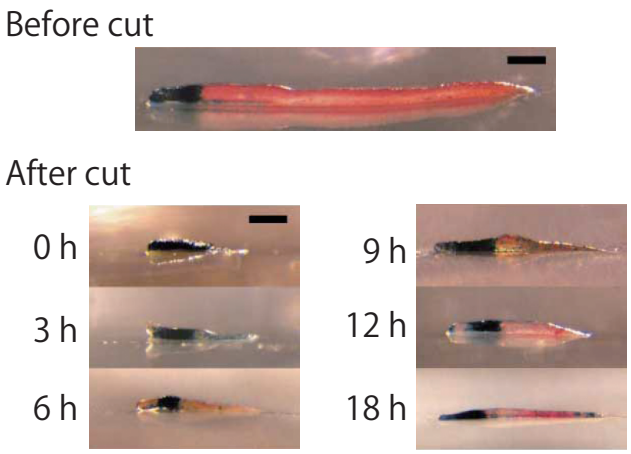

Figure 3.1: Regeneration of *Dictyostelium* slug after removal of posterior region. Anterior (left, black color): prespore cells. Posterior (right, red color): prestalk cells. Scale bar: 0.2mm. Transdifferentiation from prespore to prestalk cells are observed after the removal. Images are reproduced from [149].

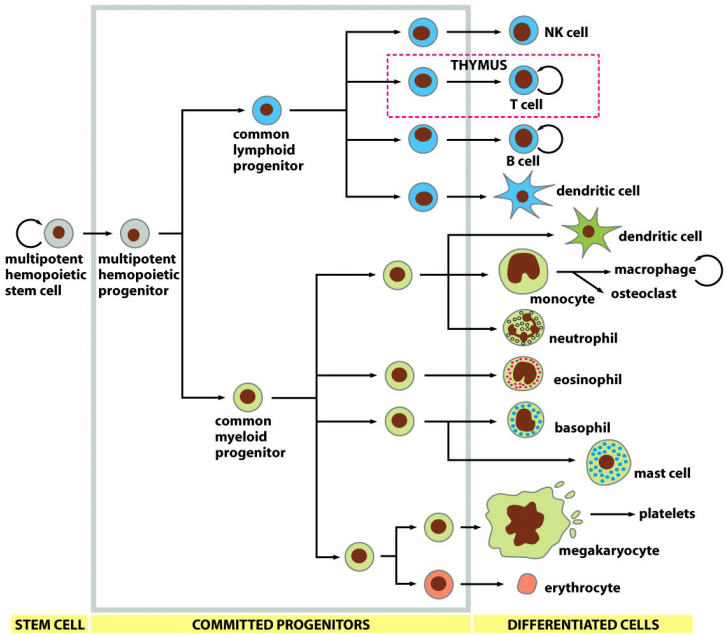

Figure 3.2: Various blood cells in the hematopoietic system. Image is reproduced from [3].

types are generated from a hematopoietic stem cell as shown in Figure 3.2. Their growth and differentiation are regulated to keep the number distribution of each cell type to achieve homeostasis of the hematopoietic system. In this case, in addition to the proportion regulation, the absolute size of stem cell population is also important because all the hematopoietic cells will ultimately die out without their existence. Indeed, regulation of the numbers of cells of each type is rather common in multicellular organisms. As the distribution of cells of each type is a property of an ensemble of cells, cell-cell interactions should be essential for such regulation.

There are several theoretical studies discussing the importance of cell-cell interactions. By considering an ensemble of cells with intra-cellular genetic (or chemical) networks and intercellular interactions, synchronization of oscillation [51, 117] or dynamical clusterings [49, 87, 88, 95, 123, 188] are observed. Cell states distinguishable from those of a single-cellular dynamics are generated, providing a basis for functional differentiation for multicellularity. The preservation of the proportion of different cell types is realized by taking advantage of Turing instability [123], while the robustness in the number distribution of different cell

types is discovered in reaction network models [49, 87, 89]. Nevertheless, regulatory mechanisms for cell type populations are not elucidated in terms of dynamical systems because of the high dimensionality of the models.

In this chapter, we propose a regulatory mechanism of cell differentiation based on dynamical systems theory by taking simple cell models with gene regulation dynamics. Specifically, we study how cell states are differentiated with the change in the total cell number following cell-cell interactions. By incorporating different interaction kinetics, we show how a simple functional module generates specific cellular behaviors such as a cell fate switching, population size regulation of a specific cell type, and preservation of the number ratio of cells of each type.

3.2 Framework of the model

Here we introduce a basic framework of our model of interacting cells with intracellular gene expression dynamics. Consider N cells interacting through a common medium (Fig. 3.3B). The internal state of i-th cell is represented by the expression pattern of m genes, as $\vec{u_i} = (u_i^1, \ldots, u_i^m)^T$. The medium under which cells are placed is represented by concentrations of n diffuse signals given by $\vec{v} = (v_1, \ldots, v_n)^T$. As the simplest case, we discard the spatial configuration of cells, thus each cell interacts with all the other cells via common signal chemicals $\vec{v}$. Gene-expression states of cells are modulated by these signal molecules, which give interactions with other cells.

For the sake of simplicity, we examine the dynamics of single gene expression, in which the state of the i-th cell is expressed by only one variable, u_i, and the intercellular interaction is mediated by only one global diffusive signal, v. As a biologically applicable system, we use a most simple network motif positive-feedback as intracellular gene network of u_i. Considering an inhibitory effect of the intercellular interaction, u_i and v obey the following equation,

$$\frac{du_i(t)}{dt} = f(u_i, v) = \frac{1}{\tau}\left(\frac{u_i^\alpha(t)}{K_u^\alpha + v^\alpha(t) + u_i^\alpha(t)} - u_i(t) + A_u\right) \tag{3.1}$$

$$\frac{dv(t)}{dt} = \mathrm{g}(\{u_i\}, v), \tag{3.2}$$

where the subscript refers to the cell index. Gene u_i activates its own expression through a feedback process, while the signal v has an inhibitory effect on the expression of the gene u_i as shown Figure 3.3A. Although we adopt competitive inhibition here, the results to be discussed are qualitatively same even if other

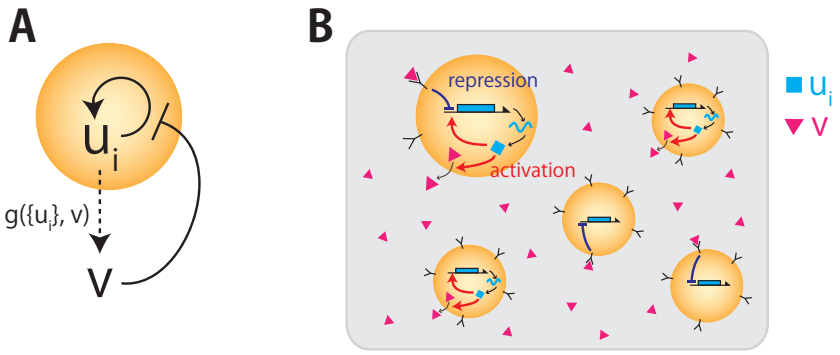

Figure 3.3: Schematic representation of the model. (A) Regulatory interactions between u_i and v. Regulation of v from u_i (broken line) depends on the details of the model. (B) Schematic image of cellular interactions.

inhibitory kinetics, such as anticompetitive or noncompetitive forms, are chosen. Generally, the signal v is released by each cell depending on its gene expression level and the signal abundances at that moment. We adopt Hill-type kinetics for self activation of the gene u_i. The parameter α denotes the Hill coefficient, i.e., the cooperativity of its kinetics, while K_u is the threshold for the activation of gene u_i in the absence of the signal v, and A_u is the activation rate of u_i by other molecules in the cell. The parameter τ is a time constant of the expression dynamics of u_i normalized by that of the signal v. Here we focus on the role of intercellular interaction on differentiation of cells in a population, so that the timescale of u_i is chosen to be much slower than that of v. This assumption on the time scale is rather natural biologically, as the gene expression occurs in a slower time scale. In the present model we study here, attractors of the system are always fixed points. Neither oscillatory nor more complex attractors exist. For numerical simulations, we use the following parameter values; $K_u = 0.1$, $A_u = 0.04$, $\alpha = 2.0$, $\tau = 10.0$. Note that the following results are qualitatively invariant as long as the Hill-coefficient α is larger than unity.

Before studying the dynamics of a population of interacting cells, we first survey the single intracellular dynamics Eq. (3.1) with v given as a constant control parameter. As is shown straightforwardly, the equation has a fixed point solution which exhibits two saddle-node bifurcations with the change in v (Fig. 3.4). We denote these bifurcation points as $v = v_1^*$ and $v = v_2^*$, and call the upper branch of the stable state as $u_{(1)}$ (or cell state 1) that is stable at $v \leq v_2^*$, and the other lower branch as $u_{(2)}$ (or cell state 2) that is stable at $v \geq v_1^*$. In the parameter region

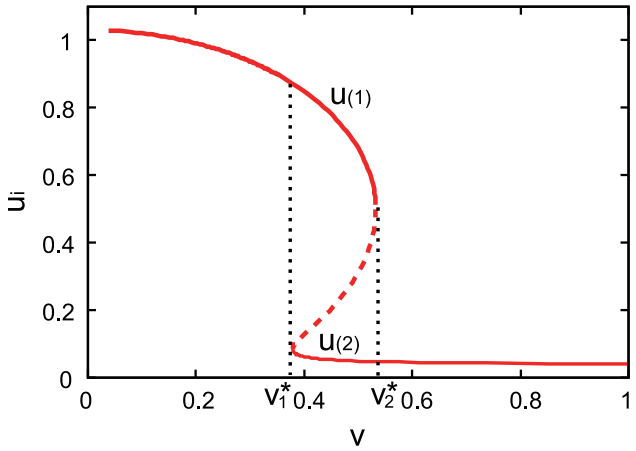

Figure 3.4: The value u of the fixed point solution as a function of the signal concentration v in our model. Solid line indicates the stable solution, while the dotted line indicates the unstable one.

$v_1^* < v < v_2^*$, the bistability of $u_{(1)}$ and $u_{(2)}$ is observed.

As shown in Fig. 3.4, the only possible stationary states of each cell are $u_i = u_{(1)}$ or $u_i = u_{(2)}$. Depending on the value of v and also on the initial condition of u_i, each of the two solutions are selected. The question we address is as follows: how is one of these bistable states selected what determines a possible range in the number distribution of the two states when intercellular interactions through v are taken into account. In the followings, we analyze three models with different types of the function $g(u_1, \ldots, u_N, v)$ to study how the differences in the kinetics of v lead to different types of regulation in the number distribution of cell types.

3.3 Model I: Cell fate determination by total cell number

As a first example of interacting cells, we adopt a model in which each cell simply emits the signal v with the same rate. The kinetics of v obeys the following equation (also see Fig. 3.5),

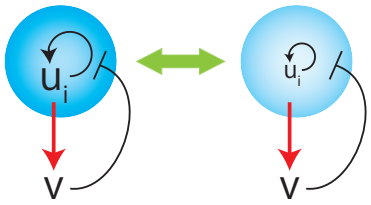

Figure 3.5: Dependence of v regulation on the expression state of u_i in model I. High u_i expression state (left), low u_i expression state (right). Signal v is constitutively generated by each cell (independent of the expression level of u_i).

model I

$$\frac{dv(t)}{dt} = \mathrm{g}_1(\{u_i\}, v) = \sum_{i=1}^{N} c_i - v(t) = c_1 N - v(t), \tag{3.3}$$

while the kinetics of $\{u_i\}$ obey Eq. (3.1). We are interested in the behavior of the stationary state as a function of the total cell number N. The stationary state solution of an ensemble of cells is generally obtained by the following procedure. First, we regard the signal v as a fixed parameter, not a variable, and obtain the solution u_i as a function of v, as already described. Next, we write down v as a function of N and $\{u_i\}$ so that the self-consistent solution of the coupled equation is obtained, from which we analyze the dependence of the solution on the total cell number.

The stationary state is simply obtained by $du_i/dt = 0$ and $dv/dt = 0$. In the present case, the solution v is independent of $\{u_i\}$, and depends only on N, which leads to

$$f(u_i, v) = 0, \quad v = c_1 N. \tag{3.4}$$

The solution curve $f(u_i, v(N)) = 0$ is shown in Fig. 3.6, and the numerical result of the ratio of the number of each cell type to the total cell number is shown in Fig. 3.7. Here we define a single-cluster of an ensemble of cells as a state in which all the cells take the same stationary states, i.e.,

$$u_i = u_{(k)} \ \ (k = 1, \text{ or } 2), \tag{3.5}$$

and a two-cluster state as that in which two cell types with $u = u_{(1)}$ and $u = u_{(2)}$

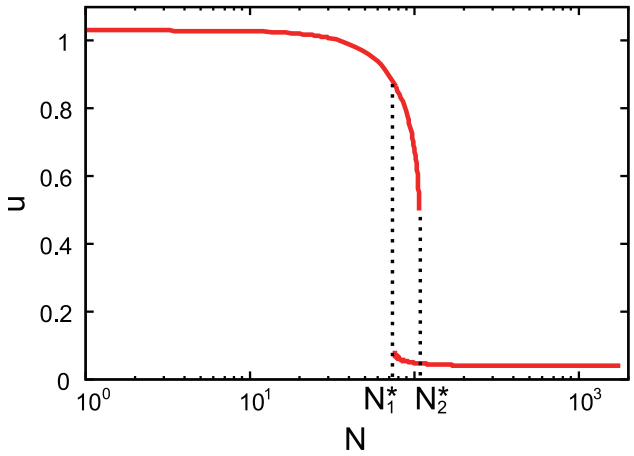

Figure 3.6: The stationary states of u_i in model I are plotted against the total cell number N. At the interval $N_1^* \leq N \leq N_2^*$, two different cell states coexist. The parameter value c_1 is set at 0.005.

coexist, so that

$$u_i = \begin{cases} u_{(1)} & \text{for } i = 1, \ldots, N_{(1)}, \\ u_{(2)} & \text{for } i = (N_{(1)} + 1), \ldots, (N_{(1)} + N_{(2)}), \end{cases} \tag{3.6}$$

where $N_{(1)}+N_{(2)} = N$. $N_{(1)}$ and $N_{(2)}$ denote the number of the cells with $u = u_{(1)}$ and $u = u_{(2)}$, respectively.

When the cell number N is lower than a threshold N_1^* $(= v_1^*/c_1)$, the single-cluster state of $u_{(1)}$ is realized, while for N larger than a threshold N_2^* $(= v_2^*/c_1)$, the single-cluster state of $u_{(2)}$ is realized, irrespectively of the initial cell state. Only within the range of $N_1^* \leq N \leq N_2^*$ are two-cluster states of $u_{(1)}$ and $u_{(2)}$ possible, where any population ratio of the cell types with $u_{(1)}$ to $u_{(2)}$ can be realized depending on the initial condition. Cell types switch between $u_{(1)}$ and $u_{(2)}$ simply by the total cell number, and the signal v works as a population size detector.

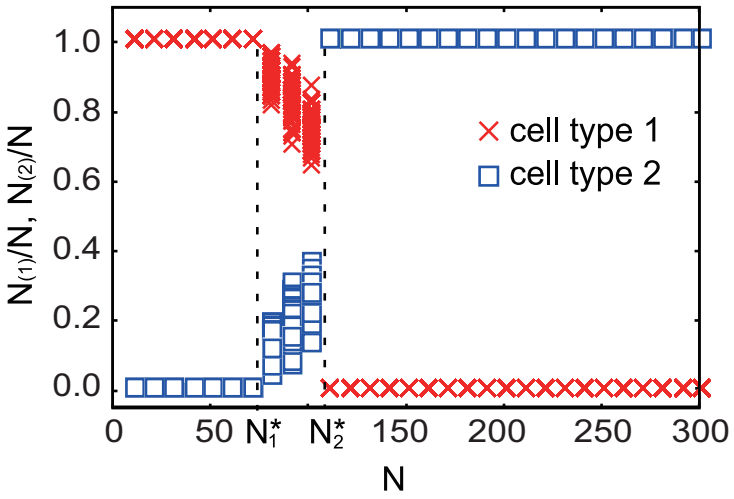

Figure 3.7: The ratio of the number of each cell type ($\times$ for $N_{(1)}$ and $\square$ for $N_{(2)}$) plotted against the total cell number N, for model I. The initial values of u_i are chosen randomly from the interval of $u_i \in [0, 1]$. The parameter value is $c_1 = 0.005$.

3.4 Model II: Diversification from single state, and population size regulation of specific cell type

Next, we consider the case in which the signal induction depends on the expression level of u_i. We will show that the cells are differentiated into two types over a wide range of the total cell number N, and that the number of type 1 cells remains at a same level herein.

The kinetics of the signal v in model II is represented as follows (also see Fig. 3.8),

model II

$$\frac{dv(t)}{dt} = g_2(\{u_i\}, v) = c_2 \sum_{i=1}^{N} \frac{u_i^\beta(t)}{K_v^\beta + u_i^\beta(t)} - v(t). \tag{3.7}$$

We here adopt Hill-type kinetics for the induction of the signal v by u_i, where β is the Hill coefficient, representing the cooperativity in the induction, and K_v

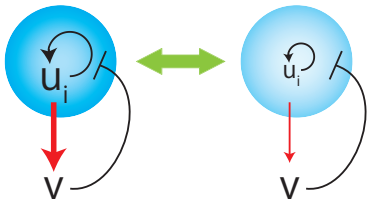

Figure 3.8: Dependence of v regulation on the expression state of u_i in model II. High u_i expression state (left), low u_i expression state (right). Signal v is mainly generated by u_i high-expression cells.

denotes the threshold value for the signal induction. The parameter c_2 gives the maximum release rate of v from each cell.

Dependence of the stationary states on the total cell number is shown in Fig. 3.9. For a small N, all the cells always fall on a single-cluster state of $u_{(1)}$. As N

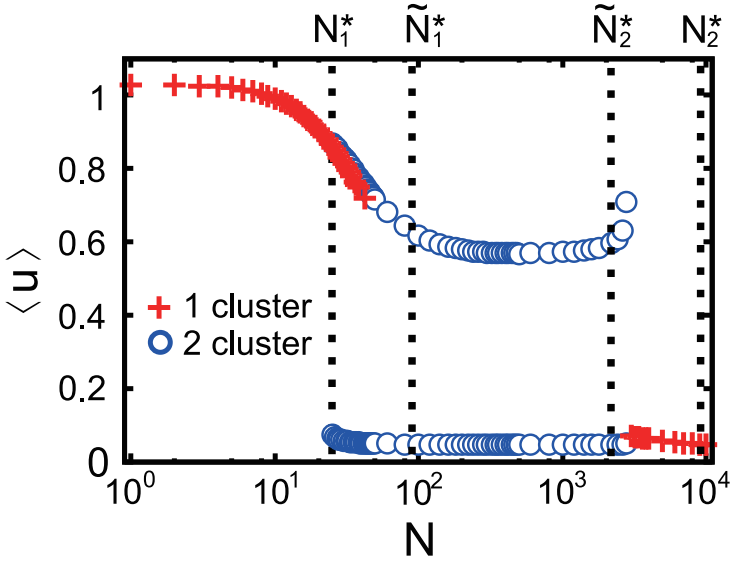

Figure 3.9: The fixed point values of u_i in model II are plotted against the total cell number N. At each N, 100 initial conditions are chosen. The expression levels of u_i for a single cluster ($+$) and two-cluster solutions ($\circ$) are plotted as a function of N. The value for two-cluster solutions is the average over initial conditions. The parameter values are set at $K_v = 2.0$, $\beta = 2.0$, $c_2 = 0.1$.

gets larger, the bifurcation to a two-cluster state occurs, where the cells take either $u_{(1)}$ or $u_{(2)}$. Here, the single-cluster state of $u_{(1)}$ ($u_{(2)}$) is realized only at a small (large) number of cells, respectively, so that there is a gap in the total number of cells between the two single-cluster states. The two-cluster state exists within this gap.

To understand the observed dependence of the clustering behavior on the cell number, we first consider the stability of a single-cluster state. From $du_i/dt = 0$, $dv/dt = 0$, and $u_i = u_{(k)}$ ($k = 1,$ or 2) for $i = 1, \ldots, N$, we get

$$f(u_{(k)}, v) = 0, \qquad v = c_2 N \frac{u_{(k)}^{\beta}}{K_v^{\beta} + u_{(k)}^{\beta}}. \tag{3.8}$$

By solving the above equations self-consistently, the solution curve of u is obtained as a function of the total cell number N (Fig. 3.10). For $N < \tilde{N}_1^*$, a single-cluster state of $u_{(1)}$ is always stable. When the cell number increases beyond $\tilde{N}_1^*$, this single-cluster state becomes unstable, while for much larger N such that $N > \tilde{N}_2^*$, the single-cluster state becomes stable again, where the cell state is $u_{(2)}$ (Fig. 3.10) . The threshold $\tilde{N}_1^*$ and $\tilde{N}_2^*$ are given by $\tilde{N}_1^* = v_2^*(K_v^{\beta} +$

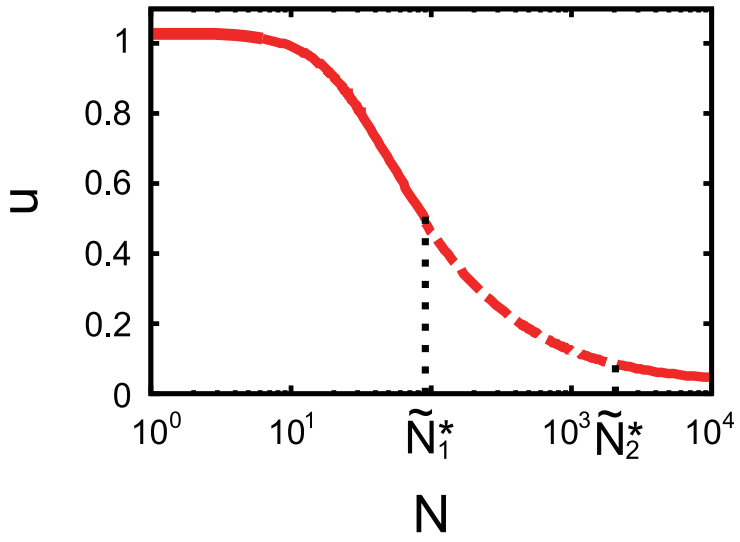

Figure 3.10: The stationary state of a single-cluster solution for model Ⅱ. Solid line indicates u_i of the stable fixed solution, while the broken line denotes that of the unstable one. The parameters are $K_v = 2.0$, $\beta = 2.0$, $c_2 = 0.1$.

$u^{\beta}_{(1)}(v^*_2))/(c_2u^{\beta}_{(1)}(v^*_2)) \simeq 92$ and $\tilde{N}^*_2 = v^*_1(K^{\beta}_v + u^{\beta}_{(2)}(v^*_1))/(c_2u^{\beta}_{(2)}(v^*_1)) \simeq 2200$, respectively.

Next, consider the condition for the existence of a two-cluster state. Because the stability of a cell state is determined by the amount of v, the condition for the existence of a two-cluster state is given by $v^*_1 < v < v^*_2$. Accordingly, considering v as a function of $N_{(1)}$ and N, a two-cluster state is possible if $N_{(1)}$ satisfies $v^*_1 < v(N_{(1)}, N) < v^*_2$. Note that v satisfies $\partial v(N_{(1)}, N)/\partial N_{(1)} > 0$. Thus, the range of the cell number N in which a two-cluster state exists is given by $N^*_1 < N < N^*_2$, where $N^*_1 = v^*_1(K^{\beta}_v + u^{\beta}_{(1)}(v^*_1))/(c_2u^{\beta}_{(1)}(v^*_1)) \simeq 24$ and $N^*_2 = v^*_2(K^{\beta}_v + u^{\beta}_{(2)}(v^*_2))/(c_2u^{\beta}_{(2)}(v^*_2)) \simeq 9400$, respectively. These threshold sizes satisfy $N^*_1 < \tilde{N}^*_1$ and $\tilde{N}^*_2 < N^*_2$, so that only two-cluster states are stable for N satisfying $\tilde{N}^*_1 < N < \tilde{N}^*_2$. In the region satisfying $N^*_1 < N < \tilde{N}^*_1$ and $\tilde{N}^*_2 < N < N^*_2$, single-cluster and two-cluster states coexist, which is demonstrated in Fig. 3.9. In this case, either a single-cluster or two-cluster state is realized depending on the initial condition.

Because the number of each cell type in these two-cluster states has to satisfy the above condition, the range of possible numbers of two cell types is limited, depending on the total number of cells. The number of cell type 1 ($N_{(1)}$) from a variety of initial conditions is plotted as a function of N in Fig. 3.11. As N is increased beyond N^*_1, $N_{(1)}$ decreases linearly with N, with a rather small slope, over a wide range of N, up to N^*_2. Within this range the value of N_1 does not change so much.

To understand this behavior we obtain the dependency of $N_{(1)}$ on v and N. In a two-cluster state $(N_{(1)}, N_{(2)}(= N - N_{(1)}))$, v is expressed by the contribution from the cell types 1 ($u_{(1)}(v)$) and types 2 ($u_{(2)}(v)$). By setting $du_i/dt = 0$, $dv/dt = 0$, and solving Eq. (3.7) for $N_{(1)}$, the number of type 1 cells $N_{(1)}$ is written as a function of N, given by

$$N_{(1)}(N, v) = -A(v)N + B(v), \tag{3.9}$$

with

$$A(v) = \frac{u^{\beta}_{(2)}(v)/(K^{\beta}_v + u^{\beta}_{(2)}(v))}{u^{\beta}_{(1)}(v)/(K^{\beta}_v + u^{\beta}_{(1)}(v)) - u^{\beta}_{(2)}(v)/(K^{\beta}_v + u^{\beta}_{(2)}(v))}, \tag{3.10}$$

$$B(v) = \frac{v}{c_2\{u^{\beta}_{(1)}(v)/(K^{\beta}_v + u^{\beta}_{(1)}(v)) - u^{\beta}_{(2)}(v)/(K^{\beta}_v + u^{\beta}_{(2)}(v))\}}. \tag{3.11}$$

Here, we note that $u_{(1)}$ and $u_{(2)}$ are determined self-consistently as functions of v, and that $A(v) > 0$ and $B(v) > 0$. For the existence of a two-cluster state, v has

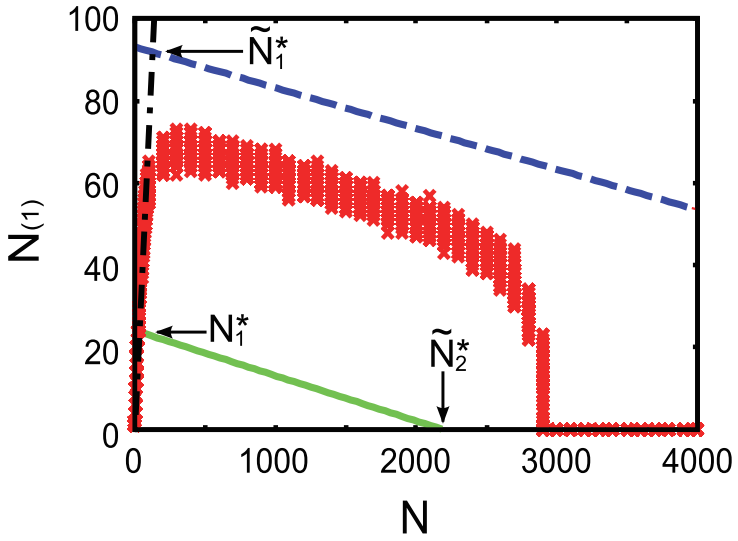

Figure 3.11: The number of cell type 1 ($\times$) is plotted against the total cell number in model Ⅱ. The initial condition of u_i is chosen randomly from the interval $u_i \in [0, 1]$. Solid and broken lines indicate $N_{(1)}(N, v_1^*) = -A(v_1^*)N + B(v_1^*)$ and $N_{(1)}(N, v_2^*) = -A(v_2^*)N + B(v_2^*)$, respectively, where $A(v_1^*) = 0.011$, $B(v_1^*) = 24$, $A(v_2^*) = 0.0099$, and $B(v_2^*) = 93$. The threshold values N_1^*, $\tilde{N}_1^*$, $\tilde{N}_2^*$ are indicated (N_2^* is out of the range of this figure). The parameters are $K_v = 2.0$, $\beta = 2.0$, $c_2 = 0.1$.

to satisfy $v_1^* < v < v_2^*$, that is, $N_{(1)}(N, v_1^*) < N_{(1)}(N, v) < N_{(1)}(N, v_2^*)$ for each N. By inserting Eq. (3.9) into this expression, it is shown that $N_{(1)}(N, v_1^*)$ and $N_{(1)}(N, v_2^*)$, i.e., the lower and upper bounds of $N_{(1)}$, decay linearly with N, with the slope of $A(v_1^*)$ and $A(v_2^*)$. In fact, a linear decrease in $N_{(1)}$ with the increase in N is clearly discernible in Fig. 3.11.

Next, we evaluate the value of the slope $A(v)$. Eq. (3.9) is written as $A(v) = \{(u_{(2)}/K_v)^\beta + (u_{(2)}/u_{(1)})^\beta\}/\{1-(u_{(2)}/u_{(1)})^\beta\}$. If $u_{(2)} \ll u_{(1)}$ and $u_{(2)} \ll K_v$ are satisfied, that is the case for the parameters used in Fig. 3.11, $A(v)$ is much smaller than unity. As a result, the decrease in $N_{(1)}$ with N is slow, and $N_{(1)}$ is sustained at a same level over a wide range of N, satisfying $N_{(1)}(v_1^*) < N_{(1)}(v) < N_{(1)}(v_2^*)$ (Fig. 3.11).

By increasing the Hill-coefficient β, $A(v)$ becomes much smaller than unity which asymptotically go to zero, even if the value of $u_{(2)}$ is the same level as $u_{(1)}$ or K_v as is shown in Fig. 3.12. Note that the conditions $u_{(2)} < u_{(1)}$ and

$u_{(2)} < K_v$ have to be satisfied. The value of the slope $A(v)$ shows an exponential decrease with β. $A(v)^{-1}$ gives a measure for the range in which two-cluster states exist. Hence, $N_{(1)}$ is sustained at an almost constant level and the population size regulation of cell type 1 is realized with a sufficiently large β.

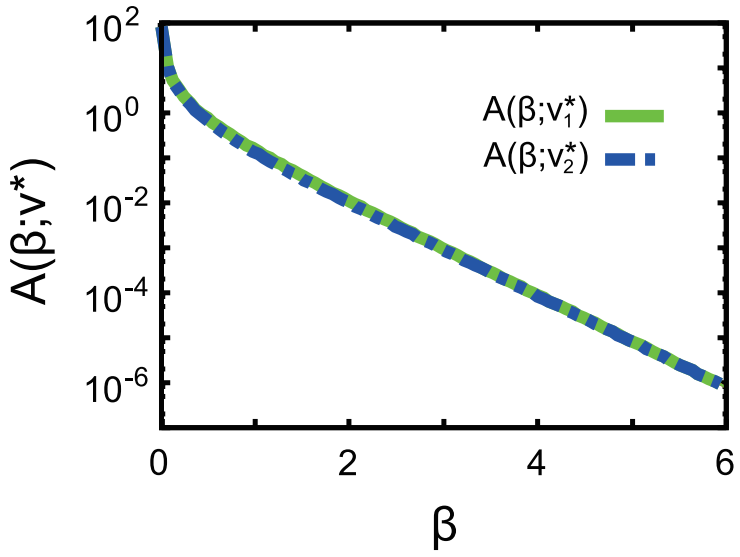

Figure 3.12: The slope $A(\beta; v)$ is plotted as a function of β. Here, $A(\beta; v)$ for two different values of v, i.e., v_1^* and v_2^* are plotted, which agree within the resolution of the plot in the figure. The parameter values are $K_v = 2.0$, $c_2 = 0.1$.

3.5 Model Ⅲ: Proportion preservation of two cell types

For precise body plan or for tissue homeostasis, proportion regulation of the number of each cell type is required. The fraction of each cell type has to be sustained at a certain range, against the change in the total number of cells. Here we modify the kinetics of v in the previous model Ⅱ to seek for the possibility of the proportion regulation. With this modification, we will show that the population fraction of the two types of cells is kept at a certain level against the change of N.

Here, the kinetics of v is modified as follows,

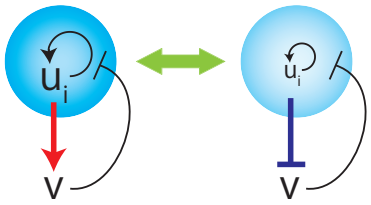

Figure 3.13: Dependence of v regulation on the expression state of u_i in model Ⅲ. High u_i expression state (left), low u_i expression state (right). Signal v is generated by u_i high-expression cells, and degraded by u_i low-expression cells.

model Ⅲ

$$\begin{aligned}\frac{dv(t)}{dt} &= \mathrm{g}_3(\{u_i\}, v) \\ &= c_{v1}\sum_{i=1}^{N}\frac{u_i^\beta(t)}{\tilde{K}_v^\beta + u_i^\beta(t)} - c_{v2}v(t)\sum_{i'=1}^{N}\frac{\tilde{K}_v^\beta}{\tilde{K}_v^\beta + u_{i'}^\beta(t)} - v(t)\end{aligned} \tag{3.12}$$

The modification to model Ⅱ is just an addition of the second term in Eq. (3.12). In other words, each cell in this model also contributes to the degradation of the signal v (Fig. 3.13).

As in the previous model, the cellular states fall on stationary states, and the bifurcation of the stationary state from a single-cluster to two-cluster states are observed with the increase in N (Fig. 3.14). Here, we first note that the two-cluster state remains stable over a wide range of N. Indeed, non-zero $N_{(1)}$ exists so that $v_1^* < v(N_{(1)}, N) < v_2^*$ is satisfied even for sufficiently large N.

Next, we study the population distribution of two cell types. As shown in Fig. 3.15, the ratio $N_{(1)}/N$ stays at a constant level against the change of N. In the same way as in the previous section, the dependency of $N_{(1)}$ on v and N for a two-cluster state is written as,

$$\frac{N_{(1)}(N,v)}{N} = \tilde{A}(v) + \frac{\tilde{B}(v)}{N}, \tag{3.13}$$

$$\tilde{A}(v) = \left[1+\left(\frac{c_{v1}u_{(1)}^\beta(v) - c_{v2}\tilde{K}_v^\beta v}{c_{v2}\tilde{K}_v^\beta v - c_{v1}u_{(2)}^\beta(v)}\right)\left(\frac{\tilde{K}_v^\beta + u_{(2)}^\beta(v)}{\tilde{K}_v^\beta + u_{(1)}^\beta(v)}\right)\right]^{-1}, \tag{3.14}$$

$$\tilde{B}(v) = v\left[c_{v1}\left\{\frac{u_{(1)}^\beta(v)}{\tilde{K}_v^\beta + u_{(1)}^\beta(v)} - \frac{u_{(2)}^\beta(v)}{\tilde{K}_v^\beta + u_{(2)}^\beta(v)}\right\} + c_{v2}\tilde{K}_v^\beta v\left\{\frac{1}{\tilde{K}_v^\beta + u_{(2)}^\beta(v)} - \frac{1}{\tilde{K}_v^\beta + u_{(1)}^\beta(v)}\right\}\right]^{-1}. \tag{3.15}$$

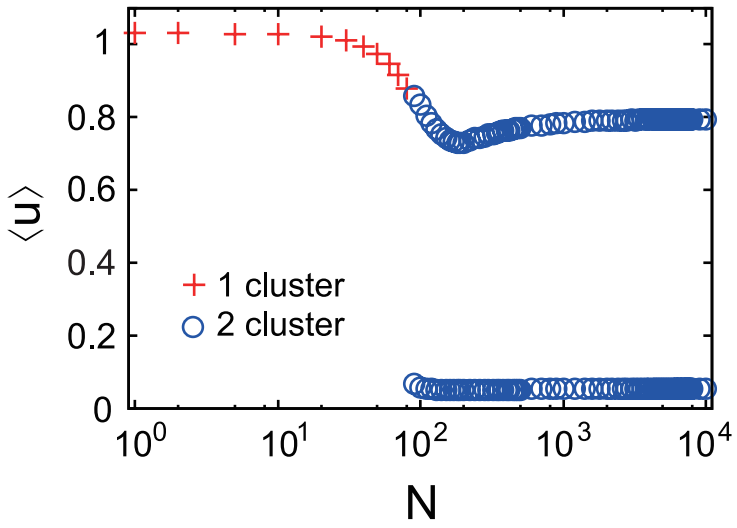

Figure 3.14: The fixed point solutions of model Ⅲ plotted against the total cell number N. At each N, 100 initial conditions are chosen. The expression levels of u_i for a single cluster (+) and two-cluster solutions (∘) are plotted as a function of N. The value for two-cluster solutions is the average over initial conditions. The parameter values are $\tilde{K}_v = 0.2$, $\beta = 2.0$, $c_{v1} = c_{v2} = 0.005$.

Here, $\tilde{B}(v) > 0$ is always satisfied. Because v satisfies $v_1^* < v < v_2^*$ for the existence of a two-cluster state, $N_{(1)}/N$ is within the range $\left(\tilde{A}(v_1^*)+\tilde{B}(v_1^*)/N\right) < \frac{N_{(1)}(N,v)}{N} < \left(\tilde{A}(v_2^*)+\tilde{B}(v_2^*)/N\right)$ for each N. As a result, when N is sufficiently large, the possible range of $N_{(1)}/N$ is given by

$$\tilde{A}(v_1^*) < \frac{N_{(1)}}{N} < \tilde{A}(v_2^*). \tag{3.16}$$

From the above expression of $\tilde{A}(v)$, if the condition $(v_2^*/u_{(1)}^{\beta}(v_2^*)) < c_{v1}/(c_{v2}K_v^{\beta}) < (v_1^*/u_{(2)}^{\beta}(v_1^*))$ is satisfied, $\tilde{A}(v)$ is within $0 < \tilde{A}(v) < 1$. This is the case for the parameter values in Fig. 3.15. Thus, the cell type ratio of a two-cluster state has to be within the range given by Eq. (3.16), so that its ratio is insensitive to the change of the total number of cells. In addition, by increasing the Hill-coefficient β, the range given by Eq. (3.16) gets narrower. Thus, the ratio $N_{(1)}/N$ is more accurately regulated. As β goes to infinity the range approaches its minimum, where the boundary is given by $\tilde{A}_{\infty}(v) = v/(c_{v1}/c_{v2} + v)$.

Note that $\tilde{A}(v)$ here is positive and is not necessarily small, in contrast to $A(v)$

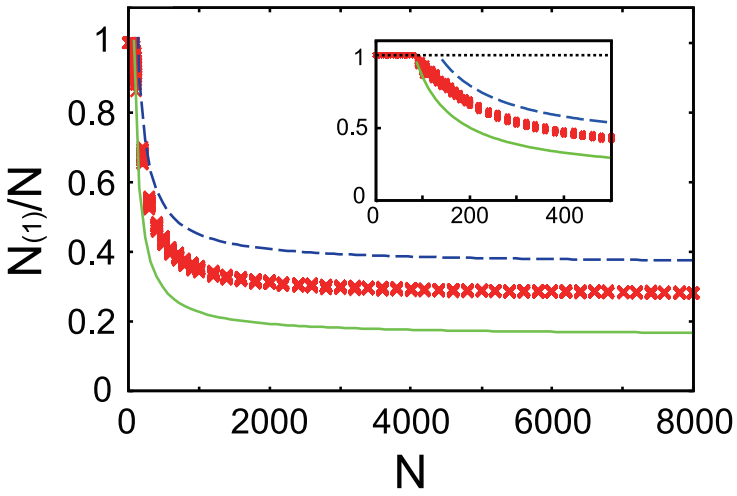

Figure 3.15: The ratio of the number cell type 1 $N_{(1)}$ to the total cell number N is plotted against N for model Ⅲ. The initial condition of u_i is chosen randomly from the interval of $u_i \in [0, 1]$. Solid and broken lines indicate $N_{(1)}(N, v_1^*)/N = \tilde{A}(v_1^*) + \tilde{B}(v_1^*)/N$ and $N_{(1)}(N, v_2^*)/N = \tilde{A}(v_2^*) + \tilde{B}(v_2^*)/N$, respectively, where $\tilde{A}(v_1^*) = 0.16$, $\tilde{B}(v_1^*) = 69$, $\tilde{A}(v_2^*) = 0.36$, and $\tilde{B}(v_2^*) = 86$. The parameter values are $\tilde{K}_v = 0.2$, $\beta = 2.0$, $c_{v1} = c_{v2} = 0.005$.

in Eq. (3.9) for the model Ⅱ. Inclusion of the second term in Eq. (3.12) allows for this behavior, and the proportion regulation of cell types is achieved over a wide range of cells.

3.6 Discussion

Through the analysis of several models, we see, i) a switch of cell types via an increase of the total cell number, and ii) diversification to two cell types. In addition, when the cells differentiate to two types, population size preservation of a specific cell type or proportion preservation of two cell types appears, depending on the interaction form with other cells. These behaviors are explained as a bifurcation of cell states via the intercellular interactions. First, possible cell types $u_{(1)}$ and $u_{(2)}$ are generated by a single positive feedback loop, which works as a module for bistability. Secondly, intercellular signal v works as a bifurcation parameter, whose abundances determine the actual cell types. This bifurcation

parameter is a function of the number of each cell type, depending on the intercellular interactions. Then, the resulting bifurcation parameter has to be determined self-consistently. This constraint restricts the number distribution of the cell types, which gives a mechanism of the regulation of the cell differentiation.

In model I, because the total cell number simply corresponds to the bifurcation parameter of cell states, the switch of the cell types by the total cell number is straightforward. In model Ⅱ and Ⅲ, since intercellular couplings change the bifurcation parameter, the transition from the single-cluster state of $u_{(1)}$ to a two-cluster state occurs by the increase in the total cell number. In model Ⅱ, the cell-type 2 contributes only weakly to the increase of v, compared with the cell-type 1. Thus, the amount of v mainly depends on the number of the cell-type 1. In contrast, in model Ⅲ, the cell-type 2 degrades v. As a result, the amount of v depends on the number ratio of two cell-types.

If a gene expression network shows bistability with a bifurcation structure as in Fig. 3.4, cell differentiation is a general consequence when cell-cell couplings are introduced. An important point here is that the same intracellular module can be used in several different biological contexts by modifying only the intercellular interaction. This is quite useful in an evolutionary perspective because new biological functions can be added by incorporating new interactions while preserving the intracellular core module.

Although we confine our analysis to a system with only fixed point solutions, oscillatory and other dynamical behaviors are often observed in biological systems. The analysis we introduced here is also applicable to such cases, as long as there are bifurcations of attractors with the change in relevant chemical concentrations that are influenced by cell-cell interactions. On the other hand, oscillatory behaviors may bring about richer bifurcations, as well as clustering of cells with regards to the oscillation phase or amplitude, as has been discussed in models with intra-cellular oscillatory dynamics and cell-cell interactions [87, 88, 95, 188]. The study of possible forms on differentiations and regulations in such dynamical systems will be important in future. In multicellular systems, cells behave in coordination by taking advantage of communication with other cells. Such collective behavior is a result of interacting systems with intra-cellular gene expression dynamics. The present self-consistent determination of bifurcation parameters through cell-cell interactions will be essential to understand organization in multicellularity.

Possible biological counterparts of the studied models

Here, we discuss several phenomena in development that may be described by our models.

model I

- **Community effect**
  The community effect was discovered in muscle formation in reaggregated cells of the *Xenopus* embryo [58]. Only when the number of cells is sufficiently large (i.e., more than one hundred), the cells differentiate to muscle. Cell-cell interaction, thus, is important for the differentiation, which is mediated by the diffusive factor eFGF, generated by each muscle progenitor cell [40, 171]. The amount of eFGF increases with the total cell number, just like the signal v in the model I. The precursor cells differentiate to non-muscle cells (correspond to cell-type 1) if they are surrounded only by a small number of cells, while they differentiate to muscle cells (correspond to cell-type 2) if they are surrounded by a large number of cells. The possible targets of the inhibition activity of eFGF are the transcription factors GATA-1 and GATA-2, the regulators of the erythropoiesis [75, 198]. In addition, eFGF can induce a transcription factor MyoD, the master regulator of myogenesis [40, 171]. Thus, the differentiation decision between erythropoiesis and myogenesis by eFGF is dependent on the cell number, as in our model I.

- **Mid-blastula transtion**
  Another example of the model I may be given by mid-blastula transition. In the cell cycle machinery in *Xenopus*, the phosphorylation states of the cyclin dependent kinase Cdc2 have a fundamental role in the entry into mitosis [60, 131]. Cdc2 positively regulates its own active state via an activation of the phosphatase Cdc25 and via an inhibition of the kinase Wee1. As opposed to the positive feedback of Cdc2, the kinase Chk1 inhibits Cdc25 and activates Wee1, and thus inactivates Cdc2. Hence it is possible that the amount of active Cdc2 shows bistability depending on the amount of active Chk1 [132]. Here, DNA accelerates the phosphorylation of Chk1 and activates Chk1. Thus, the increase in DNA amount via cleavage in the early embryo can induce a transition from the active to inactive state of Cdc2. This transition is considered to trigger the mid-blastula transition in *Xenopus* [132, 141, 167]. This induced change can fit well with the transition observed in model I, in the sense that the system parameter (the concentra-

tion of the signal v in our model or the amount of active Chk1 in the mid-blastula transition) changes as a function of the cell number, which induces a transition of the cell state. To be precise, the bifurcation parameter in the mid-blastura transition refers to the DNA content instead of the cell number. Also, we should mention that mid-blastula transition involves many other factors such as the change in cell motility and the initiation of zygotic gene transcriptions [200], which are not included in the present study. Still, the core part of the transition could be described by our mechanism.

It is known that mid-blastula transition occurs when the ratio of DNA to cytoplasm in each individual cell is increased beyond a threshold [129, 130]. In our model I, the transition threshold is v_2^*, which is equal to cN_2^*. The parameter c corresponds to the inverse of the amount of a cytoplasmic factor which has an inhibitory effect to Chk1 or has a competitive effect on DNA. Then, addition (depletion) of cytosol to an egg in the experiment corresponds to decrease (increase) in the parameter value of c in the model. Thus, also in the model I, the threshold for the transition is determined by the ratio of the DNA amount N to a cytoplasmic factor c^{-1}. T he total amount of cytoplasm is almost constant during the initial stage of embryogenesis. Thus, the DNA amount works as the bifurcation parameter for the mid-blastula transition.

model II

- **Hematopoietic stem cell**
  As for model II, consider the maintenance of the hematopoietic stem cells in mammals. Here the transcription factor GATA-2 is known to play an essential role for the maintenance of hematopoietic stem cell and hematopoietic progenitors [21, 178]. GATA-2 expression is active in hematopoietic stem cell, while during erythropoiesis, it is switched off, and is replaced by the active expression of the transcription factor GATA-1. GATA-2 activates itself and maintains its expression once activated, while GATA-1 suppresses GATA-2 transcription with FOG-1.

  Generally, an environment called stem cell niche is needed for the maintenance of the stem cell population. In a hematopoietic system, osteoblasts are known to work as such stem cell niche [20]. The stem cells compete for some chemical factors derived from this niche, and the cells which cannot take the factors differentiate to specific hematopoietic lineages. Indeed, the

competition for these factors has been discussed to be essential to the regulation of the stem cell population size, while competence for these factors decrease through the differentiation process [148]. In fact, several factors such as Angiopoietin-1, Wnt, Notch-ligand Jagged1 are identified as mediators for this niche-stem interaction [1, 8, 151]. For example, Notch signals inhibit the erythroid differentiation by suppressing GATA-1 activity through Hes1 [78, 98]. Hence, it is possible that GATA-2/GATA-1 transition is regulated by the degree of the GATA-1 mediated repression of GATA-2 which is modulated by Notch [178]. Once several cells of the stem cell population differentiate, the differentiated cells cannot respond to Jagged1 because of the decrease in the expression of Notch [148]. The competition for the niche is then relaxed, so that a certain fraction of undifferentiated cells remained as stem cells stably.

To sum up, the strength of GATA-2 repression increases with the increase of the number of hematopoietic stem cells. Through this change, the erythroid differentiation is induced and the number of stem cells is maintained at a certain level. Following this discussion, we propose that this process is described by assigning GATA-2 and Notch-ligand Jagged1 as the chemical u_i and v in our model II respectively. If this assignment is correct, GATA-2 expression is expected to show bistability for a certain range of Jagged1 stimulation. By examining this theoretical prediction experimentally, it will be possible to confirm the validity of the application of our model to the hematopoietic stem cell system. Here we should mention that, the above example for Notch often assumes the spatial heterogeneity implicitly. Even though the spatial heterogeneity was not included in our model here, extension to include it is rather straightforward, which does not alter the conclusion here. Recently, it is shown that Wnt uses the same signaling pathway as Notch for the maintenance of hematopoietic stem cells and that Wnt signal upregulates Hes1 [35, 36]. Hence it is possible that GATA-2/GATA-1 transition is also regulated via Wnt signal.

model III

- ***Dictyostelium* slug**
  Thirdly, our model III may be applied to the proportion regulation of prestalk-cell types and prespore-cell types in the *Dictyostelium* slug. Differentiation to prespore cells is induced by cAMP, and the cell state is maintained by a positive-feedback loop of prespore cell specific adenylyl cyclase G activity

[6, 70, 194]. On the other hand, differentiation-inducing factor-1 (DIF-1) is necessary for the differentiation from a prespore-cell to a prestalk-cell (at least for the differentiation to pstO, which is a subtype of the prestalk-cell) [90, 194]. As an intercellular interaction, this DIF-1 is produced by prespore-cells, and is degraded by prestalk-cells. This cell-type specific induction/destruction of DIF-1 is responsible for the proportion preservation as studied in model Ⅲ.

Evolution of differentiation mechanism

Of course, the present multicellular organisms also adopt other mechanisms of differentiation such as morphogen gradient [45, 180], besides the intra-inter-cellular dynamical mechanism discussed here. How the both mechanisms are used cooperatively will be important for understanding the development of present multicellular organisms. On the other hand, since the mechanism discussed here requires neither external morphogen gradient nor detailed gene expression network with finely tuned parameters, it is natural to expect that it worked at an evolutionarily ancient stage in multicellular development, whereas sophisticated mechanisms as in the present organisms are evolved later [42]. The intra-inter-cellular dynamical mechanism here requires just a few chemicals, and is easily accessible. More sophisticated mechanisms of differentiation, using prepattern of morphogen gradient and/or using well designed genetic network, could be evolved later to achieve more complex architecture of body plan with robust and fast developmental process.

Based on our model, we can consider a possible scenario for evolution of cell differentiation in multicellular organisms. Since bistability can provide a memory in a cell system, it would also be beneficial to unicellular organisms as a phenotypic switch to respond environmental stimulus. Hence, unicellular systems might attain bistability before evolution to multicellularity. When these cells emit some chemical factors to which they respond and communicate, interacting cells begin to show some kind of differentiation as shown in this chapter. Indeed bacteria in a biofilm take different cell states from a free living cell, which may represent ancient type of cell differentiation [33]. It is interesting to seek the origin of multicellularity along this line [50] both theoretically and experimentally.

Chapter 4

Relaxation kinetics of cell sorting

In the previous chapter, we showed that intercellular interactions give rise to regulative behaviors of cell population. We further investigate the importance of intercellular interactions in development, especially in relation to tissue morphogenesis.

One of the most important cellular machineries for morphogenesis is cell-cell adhesion. Cellular adhesion not only makes a number of cells functional tissue, but also makes possible to sort out of different type of cells; This is called cell sorting in which the intermixed cells of different types sort out to domains of homogeneous cells. Sorting out of cells via differential adhesive property is utilized for morphogenetic processes such as formation of a tissue boundary.

For the developmental processes to proceed successfully, not only the precise stationary pattern, but also the time schedule of the developmental events is important. In this chapter, we investigate the kinetics of cell sorting, that is the growth of the size of cellular domains. Although the cellular aggregates sometimes show similar properties as fluid, the behavior of a well-accepted theoretical model of cell sorting, Cellular Potts Model (CPM), is quite different from fluid. In fact, the behavior of CPM reported so far does not agree with the experimental observations of cell sorting process. Through numerical analysis of the original and extended CPM, we propose importance of the collective motion of cells for the cell sorting process.

4.1 Introduction

4.1.1 Differential adhesion and cell sorting

Different types of animals cells, when dissociated from the tissues and intermixed, sort out to domains of homogeneous cells [67, 186]. This phenomenon is called cell sorting. The sorting behavior of cells is involved in multiple morphogenetic events [172], such as in the regeneration of hydra from the aggregates of dissociated cells [182], the formation of germ layers in the early zebrafish embryo [97, 163], and tissue boundary formation in various organisms [99, 128]. The typical sorting experiment is shown in Figure 4.1. At first intermixed cells are dispersed in the culture medium (left in Fig. 4.1B). The cells begin to form aggregates via adhesion among cells (middle). Several hours later, intermixed cells eventually sort out to the domains of homogeneous cells in an aggregate (right).

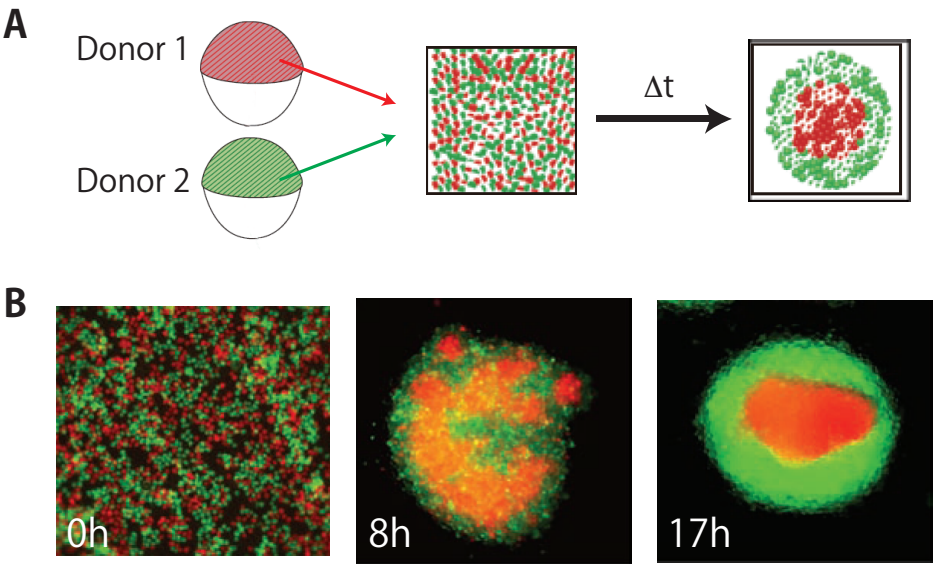

Figure 4.1: Sorting process of zebrafish early embryonic cells. (A) experimental procedure, (B) time coarse of the cell soritng process. Red: ectodermal cells; Green: mesodermal cells. Figures are partially modified from [97].

Differential adhesion hypothesis

Since the spatial configuration of different cell types in sorting aggregates mimics that of tissues and early embryos, this sorting behavior has been assumed as one mechanism driving tissue organization. In order to explain the cell sorting, Steinberg proposed the Differential Adhesion Hypothesis (DAH) [173–175]. Similar to the phase separation process, the DAH postulates that the surface tension of tissues arise from adhesion among cells and that the sorting is driven by the minimization of surface energy. Thus the engulfing configuration such as in Figure 4.1 is assumed to arise as a result of differences in their surface tensions.

The propositions of the DAH has been verified by various experiments. The cells with higher surface tension enveloped by the ones with lower surface tension in the sorting experiments of chick [43, 44] and zebrafish [163], as expected from the DAH. The endodermal cells are enveloped by the ectodermal cells in the sorting experiments of hydra, and the estimated adhesive forces between the endodermal cells were larger than that of ectodermal cells [160]. An example of such experiments is shown in Figure 4.2. The estimated surface tension and the cellular geometries in aggregates are in good agreement with that expected from the DAH.

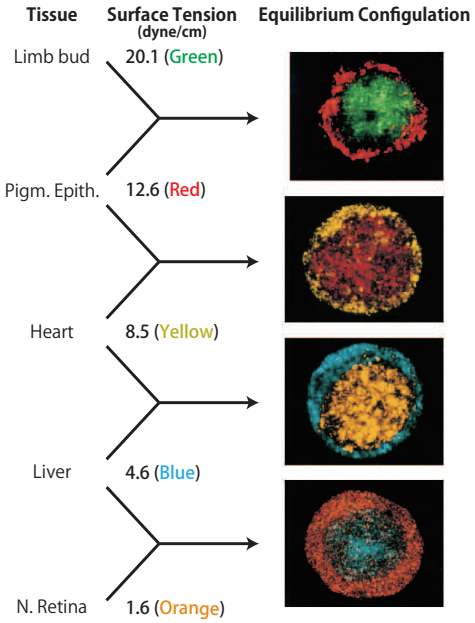

Figure 4.2: Images are reproduced from [44]

4.1.2 The Cellular Potts Model

Basic formalism of the Cellular Potts Model

Based on the DAH, several theoretical models have been proposed and have succeeded in reproducing the eventual configurations of cells in sorting experiments [9, 54, 111, 114, 124, 137]. Among these, the Cellular Potts Model (CPM), also called as Glazier-Graner-Hogeweg (GGH) model, is one of the most accepted models and has been utilized for the analyses of various morphogenetic processes [64, 82, 115, 118, 161, 201].

The CPM is a kind of Potts model with modification to account for biophysical properties of cells such as the volume and deformation of cells. In the model, each cell is represented as a set of sites on a lattice, and each site is labeled by the index of the occupying cell. The dynamics of the CPM is based on the minimization process of the effective energy of the model. The effective energy is written as follows [53, 54, 114],

$$\begin{aligned} \mathcal{H}_{\mathrm{CPM}} &= \sum_{\langle ii' \rangle} J_{\tau\tau'}(1-\delta_{\sigma\sigma'}) + \lambda_V \sum_{\sigma} (V_\sigma - V_0)^2 \\ &\quad + \lambda_L \sum_{\sigma} (L_\sigma - L_0)^2. \end{aligned} \tag{4.1}$$

Cells are indexed by Potts spin σ, and the cell type of σ-th cell is denoted as τ. V_σ and L_σ is the volume and the surface area (peripheral length in two-dimensions) of the σ-th cell, respectively. In the first term, $(1-\delta_{\sigma\sigma'})$ assures that the neighboring sites belonging to the same cell do not contribute to the energy of the system, and the interaction energies act only between neighboring cells. Thus the first term can be assumed as adhesive interactions between neighboring cells. The second term of Equation 4.1 represents the energy cost for a cell to deviate from

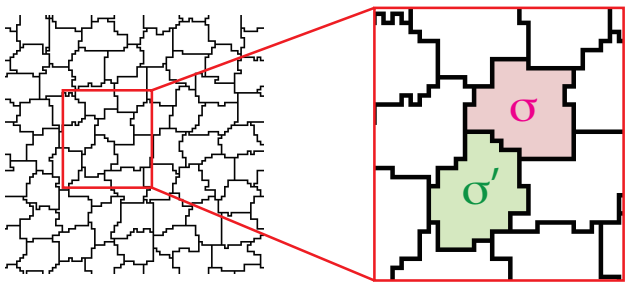

Figure 4.3: Cellular configurations in the two-dimensional Cellular Potts Model.

the preferred volume V_0, and the third term represents the cost to deviate from the preferred length L_0. Thus the relative intensity of these terms gives the degree of cell deformability. We have shown cell configurations of two-dimensional CPM on a square lattice in Figure 4.3. Each polygon corresponds to a cell in the system, and the sites of surrounded regions (belonging to the same cell) have the same index.

The time evolution of the model is obtained by the Monte Carlo simulation with Metropolis algorithm: First as a trial, the state of one of the neighboring sites is copied to a randomly chosen site. The energy difference of before and after the trial, $\Delta\mathcal{H} \equiv \mathcal{H}_{\text{after}} - \mathcal{H}_{\text{before}}$, is compared, and then the new configuration is accepted with a probability which is given as,

$$P_{\sigma\to\sigma'} = \begin{cases} 1 & \text{if} \quad \Delta\mathcal{H} < 0, \\ \exp(-\beta\Delta\mathcal{H}) & \text{if} \quad \Delta\mathcal{H} > 0. \end{cases} \tag{4.2}$$

Here, β is the inverse of the effective temperature of the system. In the CPM, the temperature ($=\beta^{-1}$) are related to the activity of the random ruffling of cell membranes. High (low) temperature corresponds to the active (less active) cell motion.

Cell sorting of the CPM

Now we discuss the sorting condition of the CPM. Here we focus on the sorting of two cell types, where two types are denoted as τ and τ'. In the above formalism of the CPM, the DAH is implemented by assigning different interaction strengths of J, depending the interacting pair. The possible interactions between cells are $J_{\tau\tau}$, $J_{\tau'\tau'}$, and $J_{\tau\tau'}$. In addition we also consider a medium surrounding the cell aggregates, thus the interactions between the cells and medium also exist. These are denoted as $J_{\tau m}$ and $J_{\tau' m}$. Surface tensions are defined as [53],

$$\begin{aligned} \gamma_{\tau\tau'} &= J_{\tau\tau'} - \frac{J_{\tau\tau} + J_{\tau'\tau'}}{2}, \\ \gamma_{\tau m} &= J_{\tau m} - \frac{J_{\tau\tau}}{2}, \\ \gamma_{\tau' m} &= J_{\tau' m} - \frac{J_{\tau'\tau'}}{2}, \end{aligned} \tag{4.3}$$

where the subscripts indicate the corresponding interfaces. To obtain the stable assembly of cells, the surface tensions should be,

$$\gamma_{\tau\tau'},\ \gamma_{\tau m},\ \gamma_{\tau' m} > 0. \tag{4.4}$$

In the typical sorting experiment, cells of one type are surrounded or engulfed by those of the other (see Fig. 4.1). For such a configuration of cells, the surface tensions should also satisfy the following inequality,

$$\gamma_{\tau m} > \gamma_{\tau\tau'} + \gamma_{\tau' m}, \tag{4.5}$$

where we assume τ as internal cells and τ' as external ones. Under the conditions of (4.4) and (4.5), the energy-minimum state corresponds to the cellular configuration in which cells of type τ is surrounded by cells of type τ'. Figure 4.4 is an example of sorting of the CPM. It is shown that the initially intermixed cells have segregated to homogeneous cell domains after sufficient time steps. For the parameters used, the surface tensions satisfy the relation, $\gamma_{rm} > \gamma_{rg} + \gamma_{gm}$ (for the notations of cell types, see the figure caption). As we see, the final configuration of cells obeys this sorting condition.

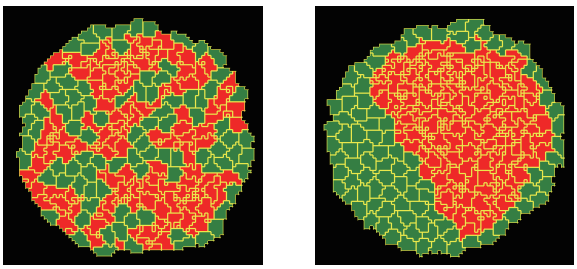

Figure 4.4: Cell sorting of the two-dimensional CPM. Left: initial configuration. Right: stationary configuration. The parameters are set as $\gamma_{rg} = 2$, $\gamma_{rm} = 15$, and $\gamma_{gm} = 8$, where cell types are denoted as r for internal (red) cells and g for external (green) ones.

Relaionship between the CPM and biophysical properties of cells

The Hamiltonians of other multicellular models such as the Vertex model, which is another well-utilized model, have basically the same structures to Equation (4.1) [37, 68, 69, 99]: interfacial interactions between neighboring cells, constraints of cell volume and surface area. The Hamiltonian of the CPM in the original papers has only the former two terms of Equation (4.1) [53, 54], and the third term is added in the later works to describe that cells take a given magnitude of surface area [82, 135]. Only with the former two terms, the parameter values of $J_{\tau\tau'}$ is necessary to be positive to keep the integrity of cells. Otherwise, each cell is

disintegrated into small pieces. Such situations are biologically implausible. In contrast, by incorporating the third term, the value of $J_{\tau\tau'}$ can be either positive or negative, depending on the biological situations of interest. In addition, this modification permits to change the tensile force of cellular surface, independently of the adhesive interactions. Thus the formalism of the Hamiltonian (4.1) could be regarded as incorporating the minimal requirements of cellular properties.

Two cellular machineries contribute to physical properties of cells and tissues. One of them is the cell-cell adhesion, where cadherins, one of the major classes of cell adhesion molecules, play a major role. The other is an actomyosin network in the subcortical region of a cell, which gives rise to the cell-cortical tension. Figure 4.5 shows the localizations of these molecules in an epithelial tissue. Both cadherin and actin are seen to be localized at the cell-cell interfaces.

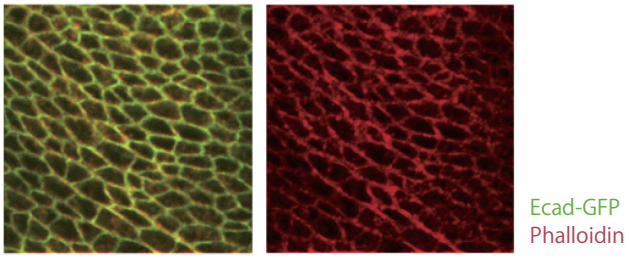

Figure 4.5: Epithelial tissue of *Drosophila melanogaster*. Adhesion and contractility at the cell-cell interface. Left: E-cadherin. Right: cortical actin. Images are reproduced from [37].

The strength of interfacial tension at the contact region of neighboring cells is modulated by the localization level of these molecules. This is illustrated in Figure 4.6. As in Figure 4.6A, cadherins and actins are localized at cell-cell interfaces. If the localization of cadherins increases, or that of actomyosins decreases, at the interface of neighboring cells, these work to expand the adhesion area as in Figure 4.6B. This corresponds to the decrease of the interfacial tension. On the other hand, if the localization of cadherins decreases, or that of actomyosins increases, the adhesion area shrinks. In this case, the corresponding interfacial tension increases.

These biophysical properties of cells can be connected to the Hamiltonian (4.1). The first term of (4.1) is interfacial interactions of neighboring cells, to which interface dependent localization of both cadherins and actomyosin networks should contribute. The third term, quadratic function of L, is related to the cellular cortical elasticity, which is determined by cortical actin network. To

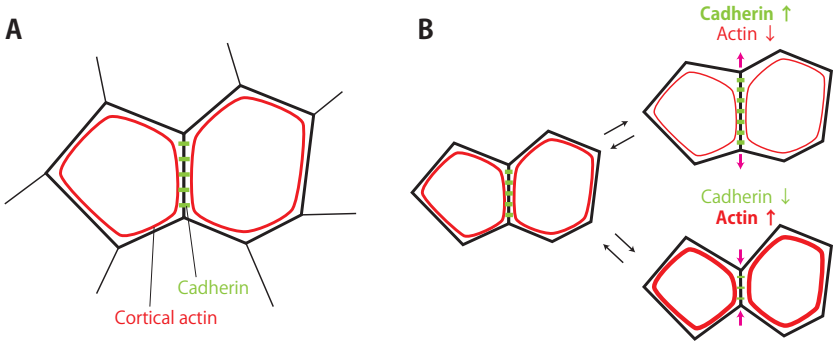

Figure 4.6: Contribution of cellular machineries to interfacial tension. (A) Localization of cadherin and cortical actin. (B) Relationship between the interfacial tension and the localization level of these molecules.

see these relationships, we define the interfacial tension of neighboring cells [97], $\Gamma_{\sigma\sigma'}$, as follows,

$$\begin{aligned} \Gamma_{\sigma\sigma'} &\equiv \frac{\delta \mathcal{H}_{\mathrm{CPM}}}{\delta L_{\sigma\sigma'}}, \\ &= J_{\tau\tau'} + 2\lambda_L(L_\sigma - L_0) + 2\lambda_L(L_{\sigma'} - L_0), \end{aligned} \tag{4.6}$$

where $L_{\sigma\sigma'}$ is the length (area in the three-dimensions) of the interface between the cell σ and σ'. Note that the defined interfacial tension, Γ, is different from the tissue surface tension, γ, defined by Equation (4.3). Considering the contributions of cadherin and actin to the interfacial interaction, $J_{\sigma\sigma'}$ could be resolved to two terms as, $J_{\sigma\sigma'} = J^{\mathrm{cad}}_{\sigma\sigma'} + J^{\mathrm{act}}_{\sigma\sigma'}$. $J^{\mathrm{cad}}_{\sigma\sigma'}$ is related to the contribution of cadherin and $J^{\mathrm{act}}_{\sigma\sigma'}$ to actin at the interface. From the previous discussion (Fig. 4.6), it is usually assumed that $J^{\mathrm{cad}}_{\sigma\sigma'}$ and $J^{\mathrm{act}}_{\sigma\sigma'}$ take negative and positive values, respectively. Using these notations, we can decompose the contributions of the two molecules to the interfacial tension as,

$$\Gamma_{\sigma\sigma'} = \Gamma^{\mathrm{cad}}_{\sigma\sigma'} + \Gamma^{\mathrm{act}}_{\sigma\sigma'}, \tag{4.7}$$

where $\Gamma^{\mathrm{cad}}_{\sigma\sigma'} = J^{\mathrm{cad}}_{\sigma\sigma'}$ and $\Gamma^{\mathrm{act}}_{\sigma\sigma'} = J^{\mathrm{act}}_{\sigma\sigma'} + 2\lambda_L(L_\sigma - L_0) + 2\lambda_L(L_{\sigma'} - L_0)$. $\Gamma^{\mathrm{cad}}_{\sigma\sigma'}$ and $\Gamma^{\mathrm{act}}_{\sigma\sigma'}$ is a contribution of cadherin and actin, respectively. Thus, the localization of cadherin and actin contributes to the strength of interfacial tension. The former decreases $\Gamma^{\mathrm{cad}}_{\sigma\sigma'}$, and the latter increases $\Gamma^{\mathrm{act}}_{\sigma\sigma'}$, respectively.

Relative contributions to the interfacial tension could be deduced by measuring the mechanical properties of cells: cell-cell adhesion and cell-cortical tension. The former is related to the first term of Equation (4.7), and the latter to the second term of (4.7). Various assays have been developed to measure these cellular

properties [138]. Two techniques to measure cell-cell adhesion and cell-cortical tension are shown in Figure 4.7. One is the micropipette aspiration [28, 65] (Fig. 4.7A), and the other is atomic force microscope [13, 63] (Fig. 4.7B). To detect the cell-cell adhesion force by micropipette (the upper of Fig. 4.7A), two cells trapped by micropipettes are attached together. The pipettes are then pulled apart until the cells are separated. The adhesion force is measured by the pressure in the micropipettes. In the case of atomic force microscope (the bottom of Fig. 4.7A), one cell is attached to the cantilever while the other is attached to the substrate. The force is deduced by measuring the bending deflection of the cantilever when two adhering cells are separated. To estimate the cell-cortical tension by micropipette aspiration technique (the upper of Fig. 4.7B), the tension is calculated from the deformation of cell surface to the aspiration. In the case of the atomic force microscope (the bottom of Fig. 4.7B), the tension is estimated from the deformation of a cell against the indentation by a bead attached in the cantilever.

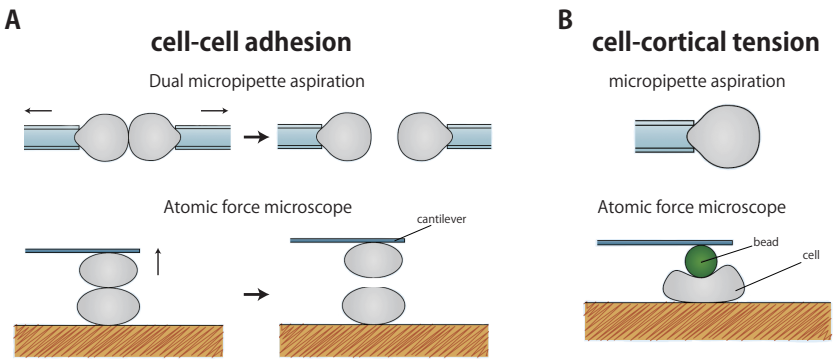

Figure 4.7: Methods for measuring the mechanical properties of single cells. Images are from [28]

Recently, Krieg and coworkers studied relative contribution of cell-cell adhesion and cell-cortical tension to the cell sorting behavior of zebrafish embryonic cells [97]. They calculated the adhesion force and the cell-cortical tension of different pairs of cell types by the atomic force microscope technique. Comparing the adhesion force and cell-cortical tension to the sorting configurations, they concluded that the cell-cortical tension mainly contributes to the interfacial tension and determines the sorting configurations in zebrafish embryonic cells. There are several other studies to estimate relative intensities of the parameters of the CPM and Vertex models from experimental observations in various situations such as cell patterning in the *Drosophila* retina [82], epithelial packing

geometries of *Drosophila* cells [37], and the tissue elongation in the *Drosophila* embryo [152]. To understand developmental processes, it is necessary to connect the molecular-level observations, such as expression-level and localization of proteins, with morphogenetic events, such as cell configuration and tissue deformation. In this sense, these attempts are important to link different hierarchical levels and obtain further understanding of developmental processes.

4.1.3 Importance of the study of biological dynamics

Until now, most studies of the CPM have argued only on the stationary patterns of interest. In contrast, the kinetics of the model have not been discussed so much. Although several works have treated dynamical properties of the model [114, 126, 135], understanding of the model kinetics remains rather poor.

Dynamics in cells and tissues can be observed in many different situations such as transport of molecules, cellular movement, and blood flow. Not only observing stationary states and patterns, but also the time-dependent dynamics give us meaningful information of the system properties. One of such examples is seen in transport of a molecule within a neuron (Fig. 4.8). Neurons typically show polarized morphology with a long axon. For cellular functions, it is necessary for neurons to transport various molecules from cell body toward axon terminals or synapses. If the transport of a molecule is conducted thoroughly by diffusive process, the molecule shows random displacements as shown Figure 4.8A. For such a diffusive molecule, the typical time it takes to diffuse a distance L is given by $t \sim L^2/D$, where D is the diffusion constant of the molecule. This indicates that the time scale grows quadratically with distance. On the other hand, if the molecule is actively transported in a directed fashion by molecular motors, the molecule moves with constant velocity V. In this case the time to travel a distance L grows linearly with length, $t \sim L/V$. We plot the time of transport as a function of the distance for these two cases in Figure 4.8B. The graph has a different slope (quadratic or linear), depending on the transport mechanism. If we assume the axon length of a neuron as $L = 10$ cm and the diffusion constant of a molecule as $D = 100$ μm^2/s, diffusive transport takes the time of 10^8 s, amounting to the order of several years. This is too long for usual cellular functions. In the case of active transport, if we assume the velocity as $V = 1$ μm/s, it takes only about 10^5 s. This corresponds to the scale of a day, which is an acceptable time scale compared to the diffusive transport.

The above example highlights that different underlying mechanisms leads to a huge difference in the kinetics, which could be a crucial for the functionality of

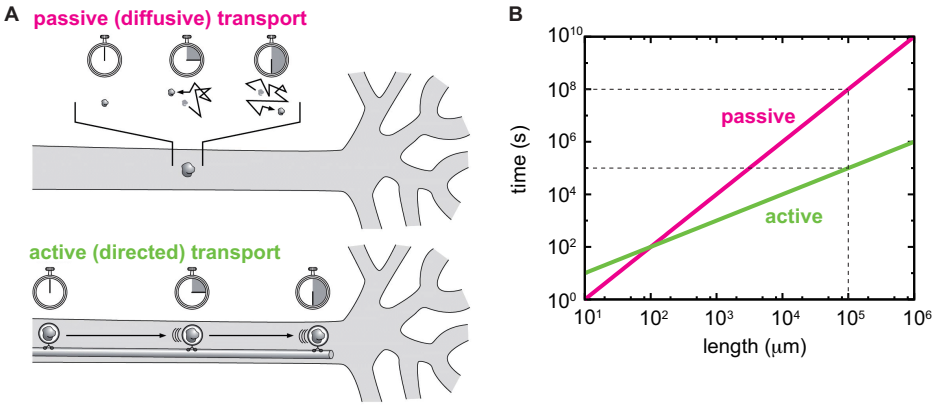

Figure 4.8: Transport of a molecule within a neuron. (A) Illustration of passive and active transport. Image is reproduced from [144]. (B) Time of transport as a function of length for two transport mechanisms. The diffusion constant is set as $D = 100\ \mu\text{m}^2/\text{s}$, which is a characteristic diffusion coefficient for a globular protein in water at room temperature. The velocity of molecular motors is set as $V = 1\ \mu\text{m/s}$ as an approximate speed of a kinesin moving on a microtubule. We have used the approximated values of D and V listed in [144].

cells and tissues. Similarly, to ask the kinetics of cell sorting is important since the time scale of this process should have a large impact on the time schedule of developmental processes. In this chapter, we deal with this question via investigating the sorting kinetics of the CPM and comparing the results with experimental observations. As a preparation for the study, we review the theory of the phase separation kinetics in the following section. Also in the case of phase separation, it will be shown that several underlying processes leads to clearly different behaviors in the kinetics.

4.2 Review of phase separation kinetics

As we have seen, the stationary configuration of cell sorting is well understood as a minimization of the surface energy which arises from the difference of the surface tension between the cell types. This is similar to the phase separation process. Typically, the phase separation of a system is induced by rapid temperature quench (cooling of the system) over the critical temperature. After temperature quench, the homogeneous phase of the system, such as binary alloys and poly-

mer blends, begins to separate into two different phases. We show an example of phase ordering process in Figure 4.9. The phase ordering usually begins with the formation of small domains, and then the length scale of the phase ordering grows with time. In the past decades, the phase separation kinetics has received much attentions, and its understanding has been developed through theoretical, numerical and experimental investigations [16, 18, 47, 66]. Here we give a brief review of the theory for the phase-ordering kinetics. For more complete description of the theory, see the above references.

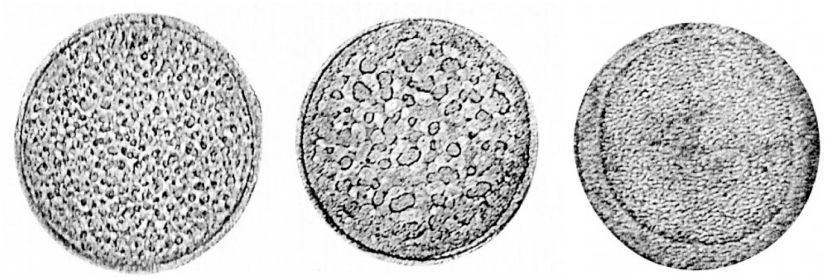

Figure 4.9: Phase separation process of sulfur hexafluoride (SF_6). It separates into gas and liquid phases after temperature quench. Images are reproduced from [14]. The phase ordering proceeds from left to right.

4.2.1 Dynamical scaling hypothesis

An important theoretical prediction in the growth process of phase ordering is that the domain growth process obeys the dynamical scaling, that is, the growth is determined only by a single length scale of the system, $L(t)$. One commonly used measure of the domain structure is the spatial correlation function of the field ϕ,

$$C(\mathbf{r}, t) = \langle \phi(\mathbf{r}_0 + \mathbf{r})\phi(\mathbf{r}_0) \rangle, \tag{4.8}$$

where ϕ is a physical quantity characterizing the two phases (such as a local magnetization, or relative density of some materials). On the basis of the standard dynamical scaling, the correlation function is expected to be scaled as,

$$C(r, t) \approx F(r/L(t)), \tag{4.9}$$

for large $L(t)$, where $F(x)$ is a unique scaling function. The dynamical scaling has been proven in some simple models [17, 31]. Although the scaling has not

System	Order parameter	Hydrodynamics	Growth exponent ($L(t) \sim t^n$)	
model A	not conserved	non	$\frac{1}{2}$	
model B	conserved	non	$\frac{1}{3}$	
model H	conserved	exist	$\frac{1}{3}^a$ $(d=3)$	$\frac{1}{2}^a$ $(d=2)$
			1^b	—
			$\frac{2}{3}^c$	$\frac{2}{3}^c$

(a) diffusive, (b) viscous hydrodynamic, (c) inertial hydrodynamic regime

Table 4.1: Domain growth laws of phase separation process

been confirmed for many cases, the evidence has been accumulated from numerical simulations [4,26,71,100] and experiments [61,62,96]. This scaling indicates that the domain structure of the system is characterized only by the single characteristic length $L(t)$, and statistical property of the system is independent of time, just by the rescaling of the length by $L(t)$.

An important consequence of the scaling is that the growth law of phase ordering obeys an algebraic growth law,

$$L(t) \propto t^n, \tag{4.10}$$

where n is the growth exponent, which value depends on several characteristics of the system such as the conservation laws and hydrodynamic effects. Before giving the explanations for each system, we summarize the growth laws of model A, model B, and model H (according to the classification of Hohenberg and Halperin [66]) in Table 4.1.

4.2.2 Non-conserved fields

We use a continuous description of an order-parameter field $\phi(\mathbf{r}, t)$. Landau free-energy functional to describe the ordered phase is given as,

$$F[\phi] = \int d\mathbf{r} \left[\frac{1}{2} |\nabla \phi|^2 + V(\phi) \right], \tag{4.11}$$

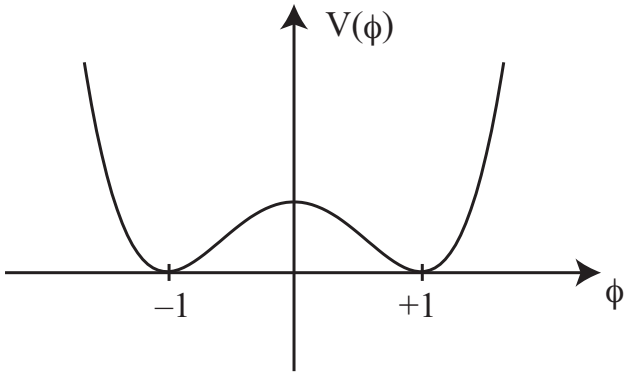

Figure 4.10: Ginzburg-Landau potential $V(\phi)$.

where the potential $V(\phi)$ has a double-well structure. For simplicity, we adopt a symmetric function $V(\phi) = (1-\phi^2)^2$, where the energy minimum of the potential is taken at $\phi \pm 1$ ($V(\pm 1) = 0$) (Fig. 4.10).

When the order parameter is not conserved ($\frac{d}{dt}\int d\mathbf{r}\phi \neq 0$), the time evolution of ϕ obeys model-A dynamics (in the classification of Hohenberg and Halperin [66]),

$$\begin{aligned} \frac{\partial \phi}{\partial t} &= -\frac{\partial F}{\partial \phi}, \\ &= \nabla^2 \phi - V'(\phi), \end{aligned} \tag{4.12}$$

where $V(\phi)' \equiv dV/d\phi$. This equation is called the time-dependent Ginzburg-Landau (TDGL) equation, or the Allen-Cahn equation. This equation corresponds to a coarse-grained description of the Ising model.

We begin with the introduction of the idea of surface tension. If the system is in a stationary state with a flat domain wall, equation (4.12) is written as,

$$\frac{d^2\phi}{dz^2} = V'(\phi) \tag{4.13}$$

with $\phi(\pm\infty) = \pm 1$ (see Fig. 4.11). Here the coordinate z is taken normal to the wall and the position of the wall (defined by $\phi = 0$) is set to be at $z = 0$. By integrating the equation once and imposing the boundary conditions, the equation gives rise to $(d\phi/dz)^2 = 2V(\phi)$. This result can be used in equation 4.11 to give the energy per unit area of the wall, that is the surface tension, as

$$\sigma = \int_{-\infty}^{\infty} dz \left(\frac{d\phi}{dz}\right)^2 = \int_{-1}^{1} d\phi \left[2V(\phi)\right]^{1/2}. \tag{4.14}$$

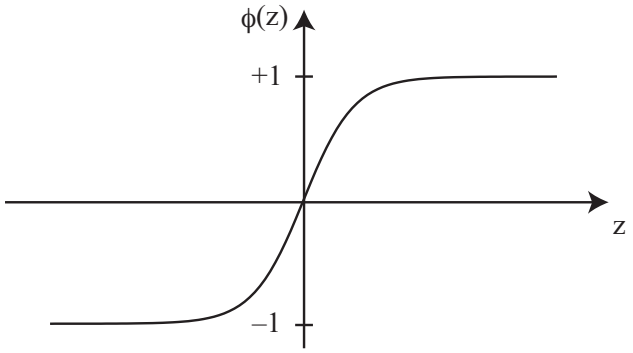

Figure 4.11: Spatial profile of the order parameter with a domain wall in one dimension.

This shows that the excess energy is localized in the domain walls. In the phase separation process, the driving force for the domain growth is the wall curvature since the energy of the system can only decrease through a reduction in the total wall area after the development of the domain walls.

The existence of surface tension implies that a force proportional to mean curvature acts at each point on the wall. Consider a spherical domain of radius R in three dimensions. The work done by the force f in decreasing the radius is $4\pi R^2 f dR$. This balances the decrease in surface energy $8\pi\sigma R dR$, which gives $f = 2\sigma/R$. Then the velocity of domain movement is given by

$$\eta \frac{dR}{dt} = -\frac{2\sigma}{R}, \tag{4.15}$$

where η is the friction constant. This indicates that the characteristic domain size of the system $L(t)$ grows with $L(t) \propto t^{1/2}$ in the case of model A dynamics.

Dimensional analysis for growth law

We can derive the growth law with exponent $1/2$ through dimensional argument of the Allen-Cahn equation (4.12). By paying our attention to the movement of domain walls, the equation is transformed to,

$$-v\frac{\partial \phi}{\partial n} = (\nabla \cdot \mathbf{n})\frac{\partial \phi}{\partial n} + \frac{\partial^2 \phi}{\partial n^2} - V', \tag{4.16}$$

where a new coordinate n is taken normal to the wall, $\mathbf{n}$ is a unit vector along this direction and v is the velocity of the domain wall. If the the domain boundary is

sufficiently sharp compared to the local curvature of the wall, the last two terms are approximately cancelled out by equation 4.13. Then we get,

$$v + \nabla \cdot \mathbf{n} = 0. \tag{4.17}$$

If there is a single characteristic scale L, then the wall velocity is estimated as $v \sim L/t$. The second term $\nabla \cdot \mathbf{n}$ corresponds to the wall curvature κ, that is approximated as $\kappa \sim 1/L$. Balancing these two terms, the growth law $L(t) \sim t^{1/2}$ is obtained.

4.2.3 Conserved fields

Next we introduce the case of conserved order parameter ($\frac{d}{dt}\int d\mathbf{r}\phi = 0$). The conservation law means that materials or chemicals of the fields is neither generated nor degraded along all the time. The conservation of the order parameter leads to a different dynamical equation of the field $\phi(\mathbf{r}, t)$,

$$\frac{\partial \phi}{\partial t} = \nabla^2 \mu, \tag{4.18}$$

where μ ($\mu \equiv \delta F/\delta\phi$) is the chemical potential and F is the free-energy functional which is the same as defined in the previous section. This is called model-B according to [66], or Cahn-Hilliard equation. This equation is a model of binary alloys and microscopically corresponds to Kawasaki-exchange dynamics of ising spins.

The domain growth mechanism is different from the non-conserved case, since the field cannot move independently. The dominant mechanism is evaporation-concentration process, that is the transport of the order parameter from domains with high curvature to those with low curvature (Fig. 4.12).

The chemical potential μ is written as $\mu = -\nabla^2\phi + V'(\phi)$. As in the calculation of the Allen-Cahn equation, we consider the movement of domain walls. The equation is transformed to,

$$\mu = -\kappa\frac{\partial \phi}{\partial n} - \frac{\partial^2 \phi}{\partial n^2} + V'. \tag{4.19}$$

A new coordinate n is taken normal to the wall. $\kappa = \nabla \cdot \mathbf{n}$ is the curvature of the wall. By multiplying both sides of the equation by $(\partial\phi/\partial n)$ and integrating over n through the wall, we get,

$$2\mu + \sigma\kappa = \int \frac{\partial}{\partial n}\left[-\left(\frac{\partial \phi}{\partial n}\right)^2 + V\right] dn. \tag{4.20}$$

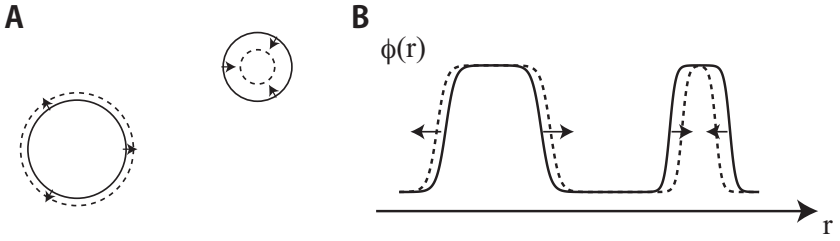

Figure 4.12: Evaporation-condensation process. (A) Schematic representation of temporal change of domains. (B) Profile of the order parameter.

By assuming that the the domain boundary is sufficiently sharp, the equation is reduced to,

$$\mu = -\frac{\sigma\kappa}{2}. \tag{4.21}$$

This gives the chemical potential near the domain wall with curvature κ.

Then the growth law can be intuitively derived as the non-conserved case. If we assume that there is only one length scale $L(t)$ in the system, both the average distance between domain walls and the curvature of the walls are determined by this scale. From (4.21), the chemical potential is $\mu \sim \sigma/L$. Thus the right-hand of (4.18) is $\nabla^2\mu \sim \sigma/L^3$, while the left-hand side is $\partial\phi/\partial t = -v\partial\phi/\partial n \sim \dot{L}/L$. This gives $L/t \sim \sigma/L^2$, and then we obtain the growth law of model B as follows,

$$L(t) \sim (\sigma t)^{1/3}. \tag{4.22}$$

The growth law of $1/3$ is considered to be true independently of the ratios of two phases ($\int d\mathbf{r}\phi/\int d\mathbf{r}$) and spatial dimensions, with the exception of the logarithmic corrections for the two-dimensional case [25, 72, 158].

In the limit that the one phase occupies a infinitesimal volume fraction c, $t^{1/3}$ growth can be demonstrated more convincingly by the Lifshitz-Slyozov theory [105] for the dimensions $d > 2$, while it is also extended for the two-dimensional case [157, 199].

4.2.4 Binary liquids

For the phase separation of binary liquids, we should take account of hydrodynamic effects. The principal new ingredient is the advection of the order parameter by the fluid. The incorporation of advection terms into equation (4.18) leads

to

$$\frac{\partial \phi}{\partial t} + \mathbf{v} \cdot \nabla \phi = \lambda \nabla^2 \mu, \tag{4.23}$$

where $\mathbf{v}$ is the local fluid velocity, μ is the chemical potential and λ is a kinetic coefficient. The velocity $\mathbf{v}$ obeys the Navier-Stokes equation of incompressible fluid as follows,

$$\rho \left(\frac{\partial \mathbf{v}}{\partial t} + (\mathbf{v} \cdot \nabla)\mathbf{v} \right) = \eta \nabla^2 \mathbf{v} - \nabla p - \phi \nabla \mu, \tag{4.24}$$

where p is the pressure and η is the viscosity of the fluid. The density ρ is constant because of incompressibility. The final term in equation (4.24) arises from the free-energy change per unit volume that accompanies the transport of the fluid. The gradients of chemical potential $\nabla \mu$ act as a driving force on the fluid. The temporal evolution of the conserved order parameter coupled with hydrodynamic effect (4.23), (4.24) is called model-H dynamics [66].

Our aim is to obtain the growth law of this system. To do this, we assume the left-hand side of equation (4.24) to be zero using the Stokes-approximation, which is the over-damped limit of the system. The resulting linear equation for $\mathbf{v}$ is written in Fourier space as follows,

$$\hat{\mathbf{v}}(\mathbf{k}) = \frac{1}{\eta k^2}[-i\mathbf{k}\hat{p}(\mathbf{k}) + \hat{\mathbf{F}}(\mathbf{k})], \tag{4.25}$$

where $\mathbf{F}(\mathbf{r}) = -\phi \nabla \mu$, and $\hat{f}$ means the Fourier transformation of f. The pressure $\hat{p}(\mathbf{k})$ is determined by the incompressibility condition $\mathbf{k} \cdot \hat{\mathbf{v}}(\mathbf{k}) = 0$. Substituting the obtained expression of $\hat{p}(\mathbf{k})$ into equation (4.25), we obtain,

$$\hat{v}_\alpha(\mathbf{k}) = \frac{1}{\eta k^2} \left(\delta_{\alpha\beta} - \frac{k_\alpha k_\beta}{k^2} \right) \hat{F}_\beta(\mathbf{k}). \tag{4.26}$$

The repeated indices mean summation from 1 to d (d is the spatial dimensions). Then in the real space (for $d = 3$), the fluid velocity is expressed as,

$$v_\alpha(\mathbf{r}) = \int d\mathbf{r}' [T_{\alpha\beta}(\mathbf{r} - \mathbf{r}') \partial_\beta \phi(\mathbf{r}')] \mu(\mathbf{r}'), \tag{4.27}$$

$$T_{\alpha\beta}(\mathbf{r}) = \frac{1}{8\pi\eta r} \left(\delta_{\alpha\beta} + \frac{r_\alpha r_\beta}{r^2} \right), \tag{4.28}$$

where $T(\mathbf{r})$ is the Oseen tensor. Substituting this result into equation (4.23), the time evolution of order parameter is given by,

$$\frac{\partial \phi}{\partial t} = \lambda \nabla^2 \mu - \int d\mathbf{r}' [\nabla \phi(\mathbf{r}) \cdot T(\mathbf{r} - \mathbf{r}') \cdot \nabla' \phi(\mathbf{r}')] \mu(\mathbf{r}'). \tag{4.29}$$

In order to estimate the sizes of the two terms on the right-hand side of the equation, we use dimensional arguments as before. Using $\mu \sim \sigma/L$, the first diffusive term is assumed as $\lambda\nabla^2\mu \sim \lambda\sigma/L^3$. From $T(\mathbf{r}) \sim 1/\eta L$, $\nabla\phi \sim 1/L$ and $\mu \sim \sigma/L$ over the integral interval $\int d^3\mathbf{r} \sim L^3$, the second advective term has the dimensions of $\sigma/\eta L$. The advective transport of the order parameter therefore dominates over diffusion under the condition $\sigma/\eta L \gg \lambda\sigma/L^3$, that is, if the characteristic length scale satisfies $L \gg (\lambda\eta)^{1/2}$. Using $v \sim L/t$ and the same dimensional argument to the expression of the velocity (4.27), the growth law of the characteristic domain size in this regime is given as,

$$L(t) \sim \frac{\sigma t}{\eta}. \tag{4.30}$$

In contrast, when $L \ll (\lambda\eta)^{1/2}$, the diffusive effect dominates the advective transport. In this case, by equating the first term of the right-hand side of equation (4.29) with the left-hand side of the equation, we obtain,

$$L(t) \sim (\lambda\sigma t)^{\frac{1}{3}}. \tag{4.31}$$

Thus far, we have ignored the inertial terms on the left-hand side of equation (4.24). Under what conditions is it justified to ignore these terms? Using the dimensional argument again, we see that in the stage $L \gg (\lambda\eta)^{1/2}$, the inertial term has the dimensions of $\rho L/t^2 \sim \rho\sigma^2/\eta^2 L$ from equation (4.30), while the terms of the right-hand side give the dimensions of σ/L^2. Comparing these terms, we can conclude that the inertial terms are negligible when $\sigma/L^2 \gg \rho\sigma^2/\eta^2 L$, that is $L \ll \eta^2/\rho\sigma$. At sufficiently late time, when this inequality is violated, the inertial terms will therefore be important.

In the case that the inertial effect is dominant over the viscous effect, the inertial terms and the driving terms of equation (4.24) should balance; the former scales as $\rho(\mathbf{v}\cdot\nabla)\mathbf{v} \sim \rho L/t^2$ and the latter as $\phi\nabla\mu \sim \sigma/L^2$. The growth law $L(t)$ is therefore obtained as

$$L(t) \sim \left(\frac{\sigma t^2}{\rho}\right)^{\frac{1}{3}}. \tag{4.32}$$

To summarize, there are in principle three growth regimes for phase separation of binary liquids in three dimensions, with the growth laws,

$$L(t) \sim t^n \tag{4.33}$$

$$n = \begin{cases} \frac{1}{3}, & L \ll (\lambda\eta)^{\frac{1}{2}}, \quad \text{(diffusive)}, \\ 1 & (\lambda\eta)^{\frac{1}{2}} \ll L \ll \frac{\eta^2}{\rho\sigma}, \quad \text{(viscous hydrodynamic)}, \\ \frac{2}{3}, & L \gg \frac{\eta^2}{\rho\sigma}, \quad \text{(inertial hydrodynamic)}. \end{cases} \tag{4.34}$$

These growth laws have been observed by numerical simulations [4, 91, 92, 147, 168, 189]. The former two regimes have been also confirmed by experiments of binary liquids [27, 196].

The above discussions apply for three-dimensions. In the case of two-dimensions, the exponents are given by,

$$n = \begin{cases} \frac{1}{2} & L \ll \frac{\eta^2}{\rho\sigma}, \quad \text{(diffusive)}, \\ \frac{2}{3} & L \gg \frac{\eta^2}{\rho\sigma}, \quad \text{(inertial hydrodynamic)}. \end{cases} \tag{4.35}$$

The diffusive regime has the exponent of $1/2$, and it is connected to the inertial regime of $2/3$ skipping the viscous regime [11, 47, 48, 120] (the reason of the absence is explained later). Both the growth laws have been observed by numerical simulations [4, 38].

We have derived the growth laws of binary liquids via dimensional analysis of model-H dynamics. In the above derivation, the physical situations of the system are rather unclear since we only considered the relative contributions of several terms of (4.23) and (4.24) for the domain growth. We rederive the exponents of diffusive and viscous hydrodynamic regime more intuitively, and comment on the case where the fractions of two fluids is not equal.

Phenomenological argument for the diffusive regime

In the diffusive regime, where viscous or inertial hydrodynamic effects have only minor effects, the growth law of the domain size is $1/3$ in three dimensions and $1/2$ in two dimensions. Although the exponent in three dimensions is same as that of model-B dynamics, the dominant mechanism in the diffusive regime is different. It is diffusion and coalescence of domains rather than the continuous transport (evaporation-condensation) of the order parameter (see Fig. 4.13, and also Fig. 4.12) [143, 169, 197]. To derive these exponents, we follow a similar argument as in [169].

We deal with a system of two immiscible fluids, where domains of one material float randomly in the other. The density of domains of radius a per unit volume is denoted as $n(r; a)$. Consider a domain of radius a_1 coalesces with domains of radius a_2. The coordinate origin is fixed at the center of the domain. The number of the collisions per unit time, $I(a_1, a_2)$, follows from an integral of

domain flux over the surface at $r = a_1 + a_2$,

$$I(a_1, a_2) = 4\pi(a_1 + a_2)^2 \left(D(a_1) + D(a_2)\right) \left.\frac{dn(r; a_2)}{dr}\right|_{r=a_1+a_2}, \tag{4.36}$$

where $D(a)$ is a diffusion coefficient of the domain of radius a. We assume that domains that just touch merge quickly, much faster than diffusion.

If the scaling hypothesis is valid, the time dependence of average density of characteristic radius size a follows,

$$\frac{dn}{dt} = -I(a, a)n = -32\pi a^2 D \frac{dn}{dr} n. \tag{4.37}$$

This indicates for the dimensions of d,

$$\frac{dn}{dt} \propto -a^{d-1} D \frac{dn}{dr} n. \tag{4.38}$$

By assuming dn/dr as $dn/dr \sim n/a$ and the diffusion constant D as $D \propto a^{-\gamma}$, the time dependence of the number density becomes,

$$\frac{d}{dt}\left(\frac{1}{n}\right) \propto a^{d-\gamma-2}. \tag{4.39}$$

The fraction of the minority phase c is written as $c = n v_d a^d$ $(0 < c < 0.5)$, where v_d denotes the sphere volume of unit radius for dimensions d. Using this relation, we obtain the growth law as follows,

$$a(t) \sim t^{\frac{1}{\gamma+2}}. \tag{4.40}$$

In the case of the spherical drop of a fluid in three dimensions, the diffusion coefficient is $D(a) \sim 1/\eta a$ from the Einstein-Stokes relation, which leads to the growth exponent of $1/3$. In two dimensions, the diffusion coefficient is $D(a) \sim 1/\eta$ [15, 93], which gives the growth exponent of $1/2$.

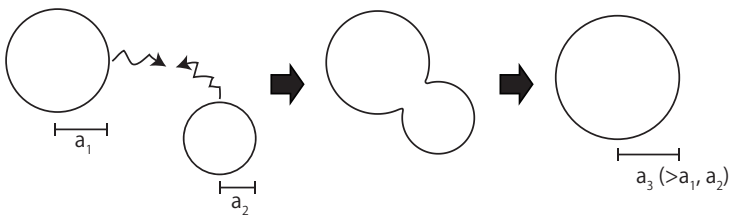

Figure 4.13: Domain-coalescence process.

Phenomenological argument for the viscous hydrodynamic regime

The linear growth law (4.30) was first derived by Siggia [169]. In the case the mixing ratio of two fluids are around 0.5, the successive coalescence of domains leads to percolating or continuous domains. For the ease of discussion, we assume continuous domains as a long tube of fluid of radius a in a medium of uniform pressure. If the long tube is under radial fluctuations with wave length l (Fig. 4.14), The difference of local curvature leads to a pressure difference along the tube. The pressure difference is roughly σ/R from the Young-Laplace relation, which leads to the pressure gradient per unit length as $\nabla p \sim \sigma/al$. This pressure gradient along the tube axis induces the flow. If the produced fluid flow follows the equation of Hagen-Poiseuille flow, the average velocity of the fluid obeys $v \sim a^2 \nabla p/\eta \sim \sigma a/\eta l$. This leads to $L(t) \sim \sigma t/\eta$ via the dimensional argument.

In this argument, the point is that the tube breaks into small domains since the tube structure of fluids in three dimensions is unstable to long-wavelength fluctuations for the wave length larger than $2\pi a$ [153, 154, 184]. In the case of two dimensions, the long tube structure corresponding to stripe-like pattern is linearly stable against infinitesimal perturbation [120]. Because of this stability, the hydrodynamic flow is not induced. Thus, there is no viscous hydrodynamic regime [11].

Growth law for the mixtures of unequal fractions

The viscous and inertial hydrodynamic regime is considered to be dominant when the mixing ratios of two fluids are almost same and percolating clusters exist. For two immiscible fluids with fractions far from equal, such hydrodynamic effect also appears at the intermediate time scale. However, at sufficiently late stage, the evapolation-condensation mechanism (Fig. 4.12) is believed to be dominant. Thus the growth law of the late stage is $t^{1/3}$ for the unequal mixtures. This has

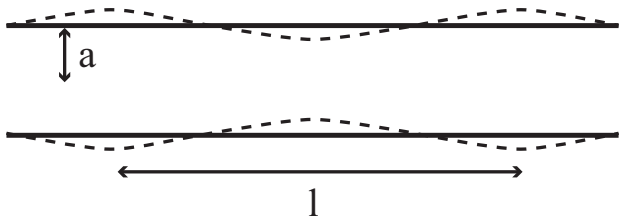

Figure 4.14: Schematic representation of deformation of a tube.

been observed in numerical simulations [26,108,133] and in experiments of binary liquids [143, 197].

4.3 Segregation kinetics of cell sorting

We have seen that the time dependence of the characteristic domain size obeys a power-law growth (Eq. 4.10), and that the transport mechanisms of the order parameter lead to a clear difference in the macroscopic behavior of the system, the growth exponent of the power law. While the diffusive transport results in the exponent $n = 1/3$ (model B), the hydrodynamic flow leads to $n = 1$ in three dimensions (model H). Thus the hydrodynamics contribute to much faster growth of domains.

To understand the morphogenetic event, connections between tissue and molecular/cellular level are important. The segregation kinetics of cell sorting is an example bridging these scales. Similarly to the phase separation process, the study of sorting kinetics will provide understanding of underlying cellular behaviors.

Experimental observations

How does the kinetics of cell sorting process behave? Beysens et al. examined the temporal behavior of the sorting of chick epithelial and retinal cells and its domain-growth kinetics [14]. The result is shown in Figure 4.15. As shown in Figure 4.15A, the sorting process shows temporal patterns similar to the phase separation kinetics (Fig. 4.9), where initially small cellular domains are formed and the size of domains grow with time. It was reported that the characteristic domain size grows linearly with time as shown Figure 4.15B [14]. Beysens and coworkers argued that the cellular aggregates behave like immiscible fluids, implying the flow-like movements of cells.

A similar argument comes from the observations of cellular aggregates of hydra [155, 156]. Rieu and Sawada studied the relaxation of elongated aggregates in a two dimensional geometry, toward a circular shape [156]. They found that the relaxation time is proportional to the radius of the aggregate, which is expected from hydrodynamic laws [112]. They also studied the profiles of cellular motions in aggregates, where correlated motions of neighboring cells are observed along with the shape relaxation of aggregates (shown in Fig.4.16). They also studied cellular motions in aggregates during cell sorting [155]. The trajectories of cell motions exhibited correlated flow of neighboring cells of the same type.

These results indicate that cellular aggregates behave like fluid, and hydrodynamic effects come from the correlated motions of neighboring cells.

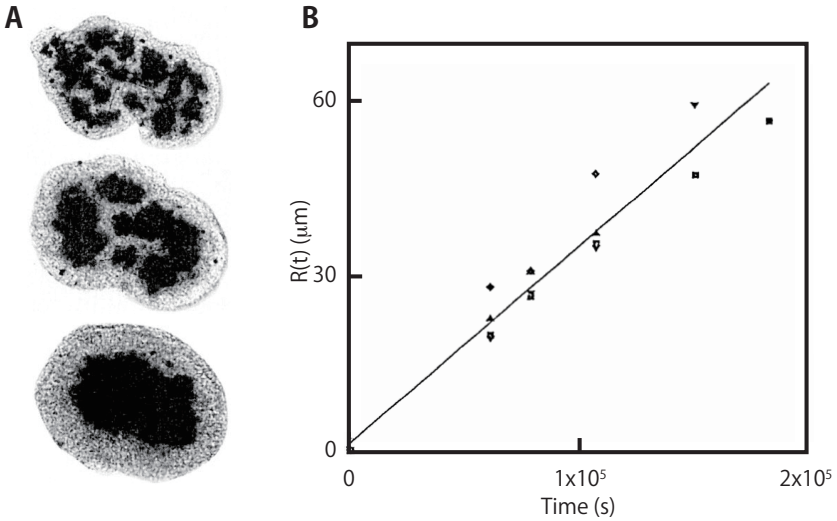

Figure 4.15: Sorting process of chick embryonic cells in three dimensions [14]. (A) Snapshot of sorting process, (B) Growth kinetics.

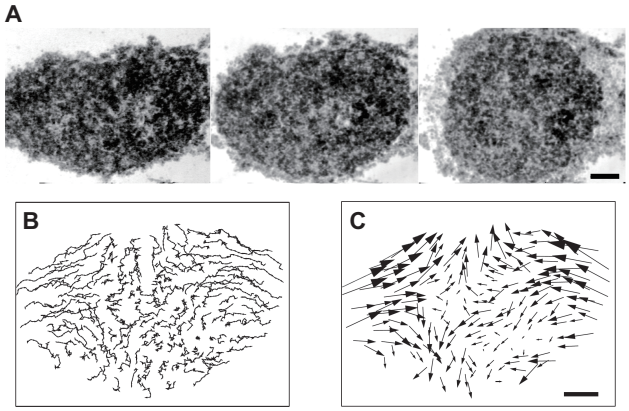

Figure 4.16: Shape relaxation of hydra endodermal aggregates. (A) Snapshots of shape relaxation. (B) Cell trajectories (from 0 to 6h) and (C) displacements (from 0 to 3h) in aggregate during the relaxation. Scale bar: $100\mu m$. The images are reproduced from [156].

Numerical simulations

While most studies of the CPM are concerned primarily with the stationary cellular geometries and patterns, several studies reported the kinetics of cell sorting

process of the CPM [53, 54, 125]. The simulation result of the two-dimensional CPM carried out in [54] is shown in Figure 4.17. Figure 4.17A shows snapshots of cellular geometries. The size of cellular domains in the sorting process of the CPM grows with time similarly to that in the sorting experiment (Fig. 4.15) and phase separation kinetics of fluid (Fig. 4.9). However, in contrast to the experiments, the kinetics of the CPM indicated the logarithmic time dependence as shown Figure 4.17B, which is much slower than the observation. Note that the decrease in the domain length in Figure 4.17B indicates the logarithmic growth of domain size since the relative density of domain boundary length has a dimension of R^{-1}.

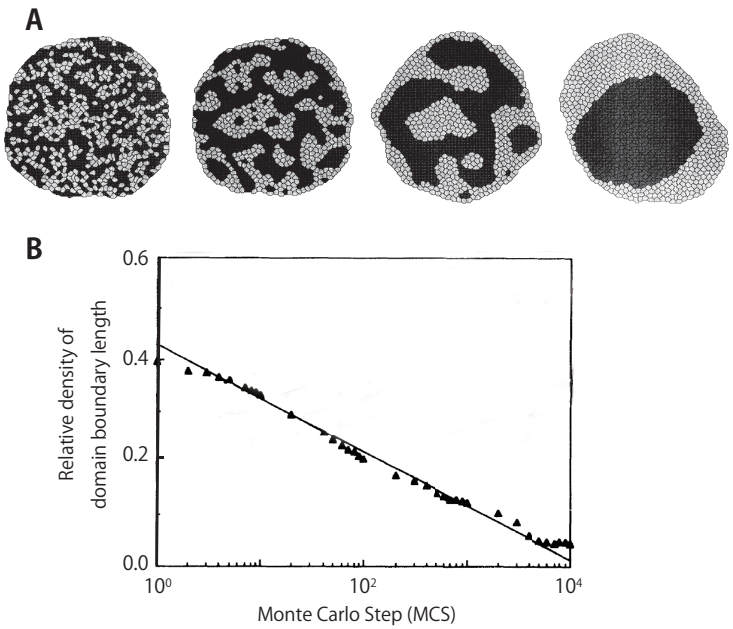

Figure 4.17: Cell sorting behavior in the CPM. (A) Snapshot, and (B) growth kinetics of sorting process. (A) and (B) is reproduced from [53] and [54] respectively.

The numerical result of the CPM means that the sorting process of cellular aggregates takes much longer time to obtain the final stationary configuration of cells. The experimental results do not show such a slow kinetics. Indeed the sorting proceeds with much reasonable time-scale. This implicates that other mechanisms lacking in the CPM are necessary to speed up the sorting process.

As such a mechanism hastening the sorting as seen the experiments, recently,

Belmonte *et al.* performed a particle based simulation of cell sorting [12]. In the model, each cell is represented by a particle, and particles within the interaction radius interact each other. Such models are sometimes called as self-propelled particle system. While cells in the CPM move randomly, particles in this model have a polarity and move with a constant velocity if there is neither other particle nor fluctuation. With this model, they studied the relaxation process of the cell sorting. They showed that the growth law of domain size is not logarithmic but algebraic (power-law) with the exponent $n \simeq 0.18$. The authors argued that the difference in the growth laws between the CPM (logarithmic) and their particle-based model (algebraic) is a result of the active cellular movement they introduced in the model. However, the obtained exponent is still much slower than the experimental result, and even slower than the phase separation of the model B, where dynamics is driven only by diffusion.

4.4 Re-investigation of the kinetics of the Cellular Potts Model

4.4.1 Sorting of two cell types with the mixture ratio $50:50$

To resolve the discrepancy between the experiments and numerical results, we first re-analyzed the CPM. In the previous studies, the numerical calculations of the CPM were performed with about 1000 cells [54, 125]. This system size for the simulation might have been very small to determine the growth law precisely. To clarify this possibility, we first re-analyzed the kinetics of CPM by using a sufficiently large system size. We investigated the sorting of two cell types with the Hamiltonian, which is given by (4.1; here, we denote the type of σ-th cell as τ_σ with $\tau_\sigma = +1$ or -1. We used a square lattice in two dimensions for the numerical simulation with a periodic boundary condition. In our simulation, all sites of the lattice were filled by cells; thus, the number of sites N is set as $N = MV_0$, in which M represents the number of cells. For ease of calculations, the adhesive strength of homotypic cells was assumed to be the same for both types, that is, $J_{++} = J_{--}$. The adhesive strength of heterotypic cells was assumed to be symmetric, that is, $J_{+-} = J_{-+}$, which is normally true. For ease of comparing the results of the different parameter values, we defined the rescaled parameters; $\tilde{J}_{\tau\tau'} = J_{\tau\tau'}L_0$, $\tilde{\lambda}_V = \lambda_V V_0^2$, and $\tilde{\lambda}_L = \lambda_L L_0^2$. The rescaled parameters were set as $\tilde{\lambda}_V = 1250$, $\tilde{\lambda}_L = 600$. The adhesive interactions were set as $\tilde{J}_{++} = \tilde{J}_{--} = -300$ and $\tilde{J}_{+-} = \tilde{J}_{-+} = -100$, where the interactions satisfy the relation,

$(2\tilde{J}_{+-} - \tilde{J}_{++} - \tilde{J}_{--}) > 0$, to favor cell sorting. The effective temperature of the system was set as $\beta = 0.1$. We denoted the degree of the mixture ratios as ψ_0, where

$$\psi_0 = \frac{M_+ - M_-}{M}. \tag{4.41}$$

M_+ and M_- are the number of type $+1$ and -1 cells, respectively. First, we investigated the case of $\psi_0 = 0$, that is, the fraction of the two cell types was set at $50 : 50$. Figure 4.18 shows the typical evolution of the sorting process. Initially, two types of cells are distributed randomly (Fig. 4.18 A). Then the aggregates of each type begin to form (Fig. 4.18 B), and its domain size (width) increase with time (Fig. 4.18 C, D). Finally, the cells are completely segregated to layers of homogeneous cells (Fig. 4.18 E).

Domain growth of the CPM obeys the algebraic growth law

The domain size of each cell type continues to increase until the domain grows up to a size comparable to the system size. We quantified the kinetics of this domain growth process in a large system size. Here, the optimal volume and peripheral length of cells were set at $V_0 = 9$ and $L_0 = 12$. To characterize the domain size, one typical length scale is the perimeter density of domains, γ, which is defined as,

$$\gamma \equiv (1 - \psi_0)^{-1/2} \frac{A}{N}, \quad A = \sum_{\langle ii' \rangle} (1 - \delta_{\tau\tau'}). \tag{4.42}$$

A refers to the number of heterogeneous interactions, and N is the number of sites in the system. The prefactor is added for normalization. The summation is over the neighboring square lattice sites. Figure 4.19 shows the time dependence of γ from random initial conditions. At the early stage (MCS $< 10^4$), $\gamma(t)$ seems to decrease logarithmically with time (Fig. 4.19A). Such behavior of the peripheral length is consistent with the previously reported results (Fig. 4.17) [54, 125]. However, when we observed the dynamics in a long time scale, the temporal behavior did not obey the logarithmic decay. Instead, γ exhibited an algebraic (power-law) as, $\gamma(t) \sim t^{-n}$ with $n = 0.31 \pm 0.01$ (Fig. 4.19B). The growth exponent of γ is obtained from the least-square fit to the data within the time interval $1 \times 10^5 <$ MCS $< 2 \times 10^6$.

Another indicator of the domain growth is the spatial correlation function of cell types, $C(r, t)$. The correlation function is defined as,

$$C(\mathbf{r}, t) = C(x, y, t) = \langle \tau(\mathbf{r}_0, t)\tau(\mathbf{r}_0 + \mathbf{r}, t) \rangle_{\mathbf{r}_0} - \langle \tau(\mathbf{r}_0, t) \rangle^2_{\mathbf{r}_0}. \tag{4.43}$$

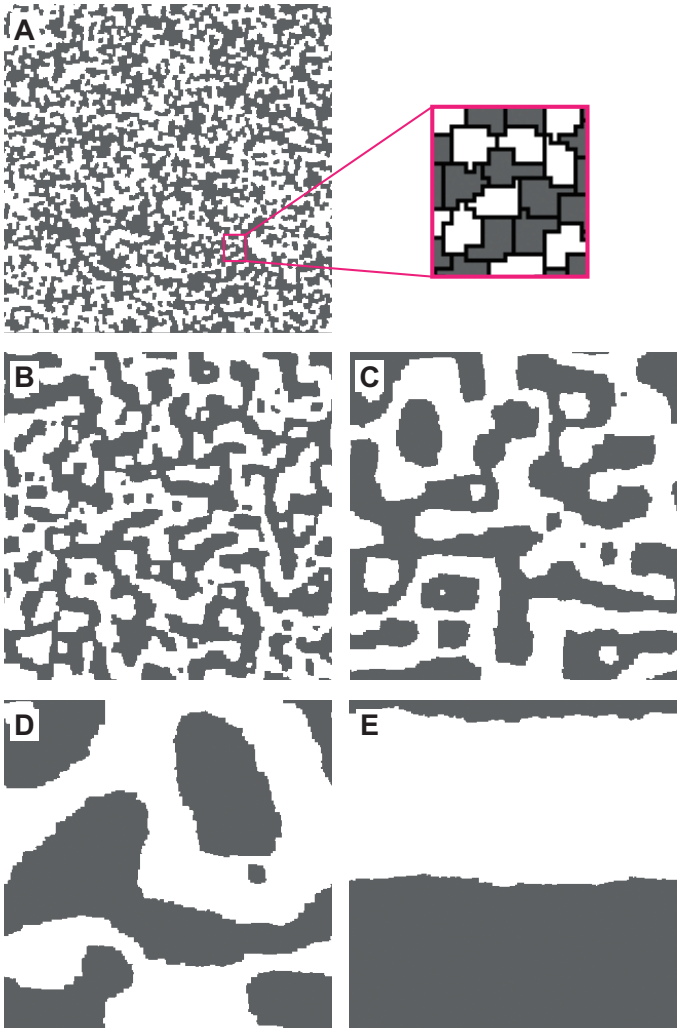

Figure 4.18: Cell sorting process in the CPM. Gray and while cells represent the cell types of $\tau = +1$ and -1. The number of cells M was set at $M = 32^2$. The optimal volume and peripheral length of cells were set as $V_0 = 25$ and $L_0 = 20$, respectively. Configurations were shown on several occasions (the number of Monte Carlo Steps; MCS) (A) MCS $= 0$, (B) MCS $= 5 \times 10^3$, (C) MCS $= 5 \times 10^4$, (D) MCS $= 4 \times 10^5$, and (E) MCS $= 4 \times 10^7$. The simulations were performed under periodic boundary conditions.

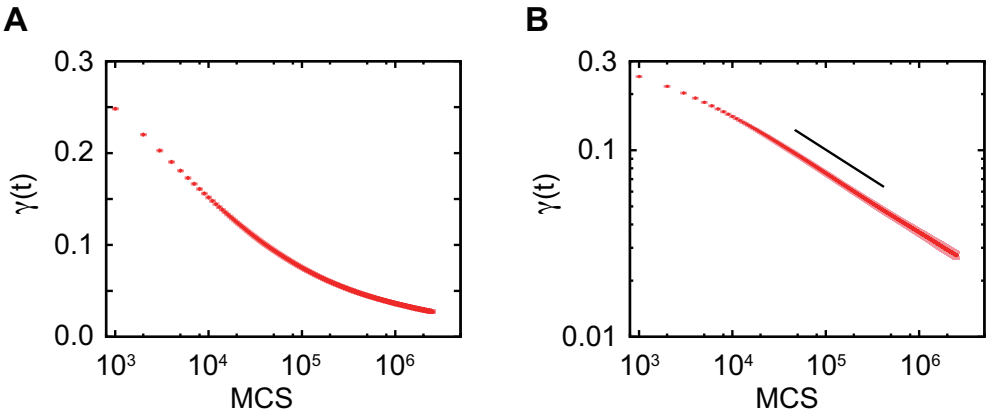

Figure 4.19: Time dependence of perimeter density of domains, $\gamma(t)$. The data are shown on (A) semi-log and (B) log-log coordinates. The number of cells is $M = 288^2$. The data were averaged over 24 independent runs. Error bars represent the SD of the trials. In the normal scale of γ, the error bars are smaller than the symbol size. The solid lines with the slope $n = -0.32$ are for visual aid.

The brackets denote an average of all sites. For numerical calculations, we approximated $C(r,t)$ as $C(\sqrt{2}r,t) \simeq \{C(r,r,t)+C(r,-r,t)\}/2$ for ease of calculation. Figure 4.20 shows the $C(r,t)$ of the simulation at several time points. The correlation function exhibits oscillation at about zero, reflecting alternating domain layers (Fig. 4.18). Corresponding to the domain growth with time, the correlation length or the wave length of the oscillation" increases. We defined the characteristic domain size of the system, $R(t)$, by the first point where $C(r,t)$ crossed the zero line (see Fig. 4.20), as is commonly adopted in the analysis of phase separation kinetics [7, 72, 159]. The time dependence of $R(t)$ is shown in Figure 4.21. Although we could not discriminate whether $R(t)$ obeys the logarithmic or algebraic growth at the early stage (MCS $< 10^4$), we did observe a linear relation between $\ln R(t)$ and $\ln t$ at late stage (MCS $> 4 \times 10^4$), implying the algebraic growth of $R(t)$ with $n = 0.33 \pm 0.02$. The exponent was obtained from the fitting within the time interval $1 \times 10^5 <$ MCS $< 2 \times 10^6$.

Both indicators of domain size, $R(t)$ and $\gamma(t)$ (γ^{-1} to be exact), exhibited algebraic growth except in the early stage (MCS $\lesssim 10^4$). This suggests that the kinetics of the domain growth in the CPM follow not the logarithmic but an algebraic growth law for a sufficiently large system size.

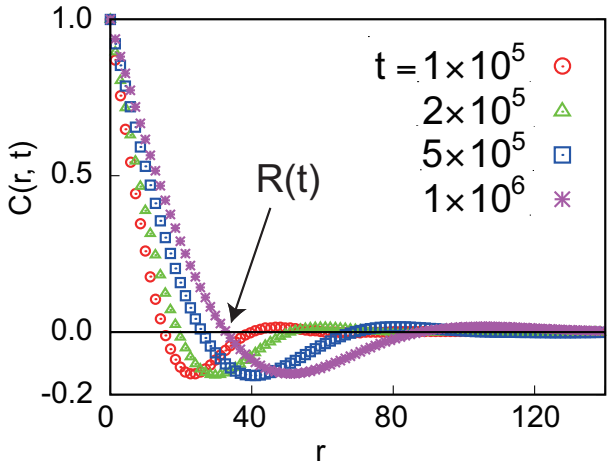

Figure 4.20: Spatial correlation of cell types, $C(r,t)$; $C(r,t) = \langle C(\mathbf{r},t)\rangle_\theta$. $C(r,t)$ was shown at several time points; MCS $= 1\times10^5$, 2×10^5, 5×10^5, and 1×10^6.

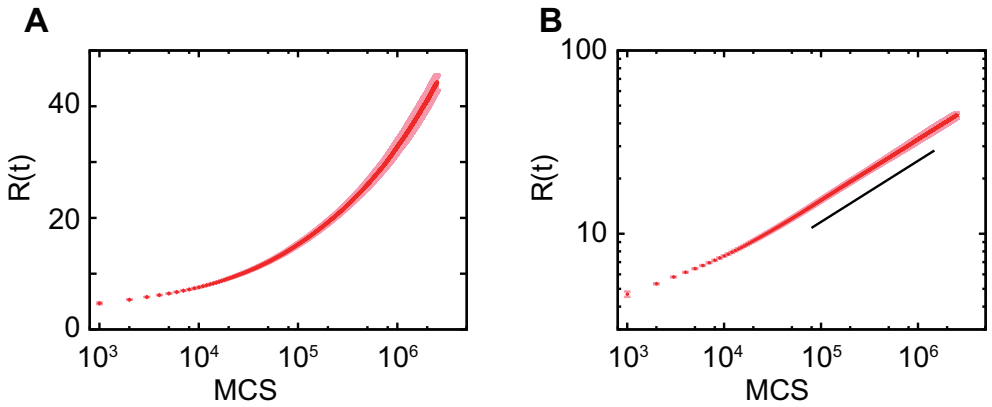

Figure 4.21: Time dependence of the characteristic domain length, $R(t)$. The data are shown on (A) semi-log and (B) log-log coordinates. The number of cells and trials are the same as that shown in the figure 4.19. Error bars represent the SD of the trials. The slope of the solid line is $n = 1/3$.

Growth exponent is compatible with the model-B dynamics

The time dependence of domain size exhibited the power law behavior with the exponent $n \sim 0.31$ for $\gamma(t)$ and $n \sim 0.33$ for $R(t)$. These are close to the exponent of model B, $n = 1/3$. To confirm the exponent of the CPM, we considered the asymptotic behavior of domain growth. The slope of the log-log plot of $R(t)$ or $\gamma(t)$ is interpreted as an effective exponent $n_{\text{eff}}(t)$ at time t [24, 72, 189]. n_{eff} is written as,

$$n_{\text{eff}}(t) \equiv \frac{d[\ln R(t)]}{d[\ln t]}. \tag{4.44}$$

For numerical simulation, we calculated the effective exponent using the approximation $n_{\text{eff}}(t) \simeq \frac{\ln(R(ct)/R(t))}{\ln(c)}$. c is set at $c = 5$. Figure 4.22 shows $n_{\text{eff}}(t)$ as a function of $1/R(t)$ for $M = 128^2$, 216^2, and 288^2. For each system size, $n_{\text{eff}}(t)$ increases monotonically as $R(t)$ increases at early stage, and after that, stays around $1/3$ as $1/R(t)$ approaches 0. For the behavior of $n_{\text{eff}}(t)$ at late stage, the coincidence of $n_{\text{eff}}(t)$ to $1/3$ is improved as the system size is increased. This result is consistent with the expectation of $n = 1/3$.

Correlation function of cell types exhibits the dynamical scaling behavior

As described in the previous section, an important theoretical prediction in the phase separation kinetics is that the domain growth process obeys the dynamical scaling. From the scaling hypothesis, the correlation function is expected to be scaled as the equation (4.9). To check if the scaling is also valid for the CPM, the $C(r, t)$ of Figure 4.20 is re-plotted, here as a function of $r/R(t)$ (shown in Figure 4.23). The data for different time points lie on the same curve. This shows that the system rescaled by the length $R(t)$ exhibits the same statistical property for the spatial correlation of cell types. Thus, the scaling holds for the sorting process of the CPM as well.

Taken together, we conclude that the kinetics of the domain growth in the CPM follows the algebraic growth law with $n \sim 1/3$ in the case of $\psi_0 = 0$. This exponent is consistent with the model-B dynamics. In addition, our results indicate a faster relaxation than the results of previous works on the CPM [54, 125].

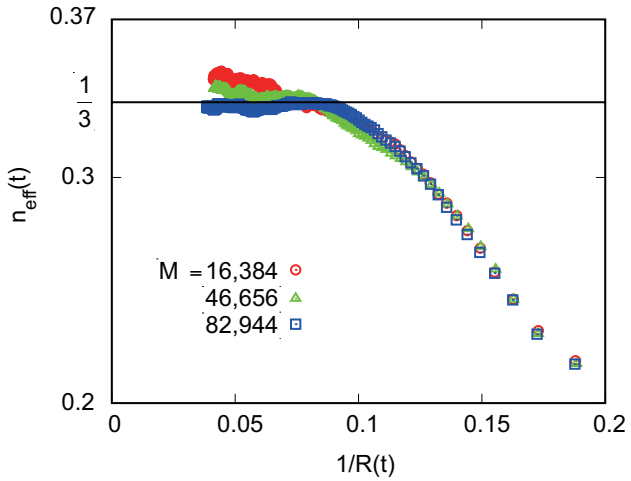

Figure 4.22: Asymptotic behavior of the effective exponent n_{eff} derived from $R(t)$. $M = 128^2$(red circle), 216^2 (green triangle), and 288^2 (blue square).

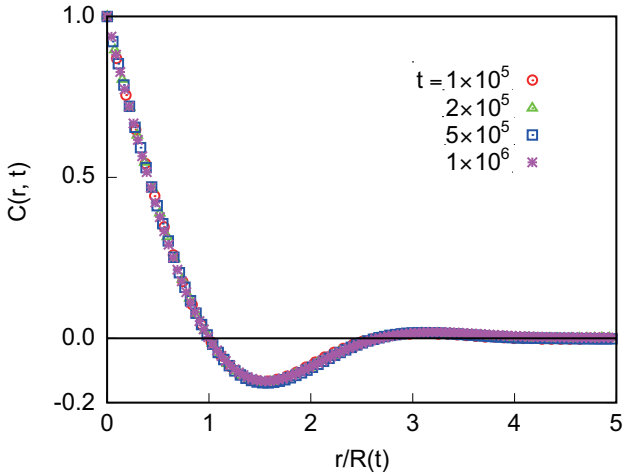

Figure 4.23: Correlation function $C(r,t)$ as a function of the rescaled length $r/R(t)$. The data are shown at MCS $= 1.0 \times 10^5$, 2.0×10^5, 5.0×10^5, 1.0×10^6. The naive correlation function is shown in Figure 4.20.

4.4.2 Sorting of two cell types with uneven ratios

Uneven mixtures show different growth kinetics

We next investigate the sorting process in a case where the mixture ratio of two cell types is not $50 : 50$, that is $\psi_0 \neq 0$. Since $\{J_{ij}\}$ is symmetric, we only consider the case $\psi_0 \geq 0$; the cell of $\tau = +1$ is in the majority of the system. Similarly with the even mixtures, we calculated $\gamma(t)$ and $R(t)$. Figure 4.24 shows the kinetics of $\gamma(t)$ for several different ratios. $\gamma(t)$ does not show logarithmic time dependence (in Figure 4.24A). Instead, as shown in Figure 4.24B, $\gamma(t)$ seems to exhibit power-law decrease at the late stage for the mixtures $\psi_0 \geq 0.4$. For the mixtures $\psi_0 = 0.06$ and 0.1, which are close to $\psi_0 = 0.0$, $\gamma(t)$ shows a power-law with an exponent close to that of $\psi_0 = 0$ at the intermediate stage (10^4 MCS $< 10^5$). At the late stage, $\gamma(t)$ shows a different time dependence from that of $\psi_0 = 0$, with a slower slope.

The results of $R(t)$ for uneven mixtures are shown in Figure 4.25. The time dependence of $R(t)$ also seems different from the logarithmic growth for $\psi_0 \geq 0.4$ (4.25A). For $\psi_0 = 0.1$ and 0.2, although $R(t)$ seems to exhibit logarithmic growth in the late stage, this is probably a transient behavior associated with a crossover between different growth mechanisms as is shown later. The power-law behavior of $R(t)$ is similar to that of $\gamma(t)$ as shown in Figure 4.25B; for $\psi_0 \geq 0.4$, $R(t)$

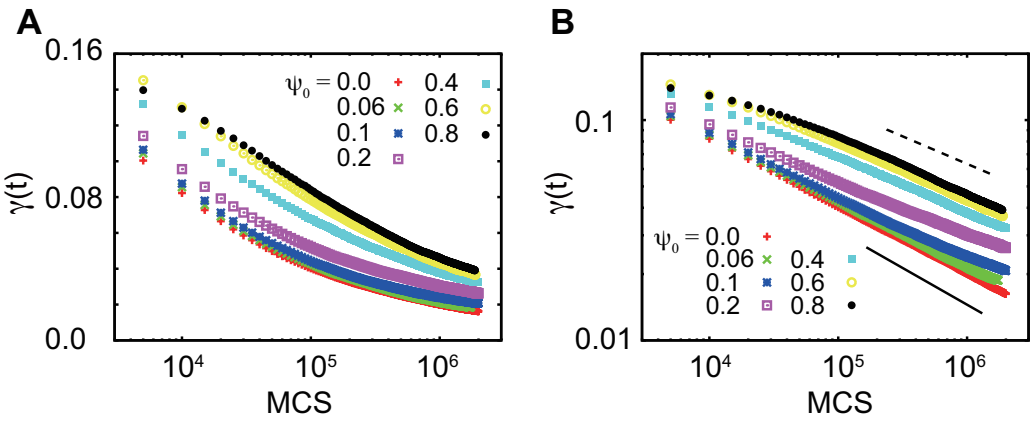

Figure 4.24: Time dependence of $\gamma(t)$ for uneven ratios. The data are shown on the (A) semi-log and (B) log-log coordinates. The number of cells is set as $M = 512^2$. The optimal volume and peripheral length are set as $V_0 = 25$ and $L_0 = 20$. The slopes of the solid and broken lines are $1/3$ and $1/4$, respectively.

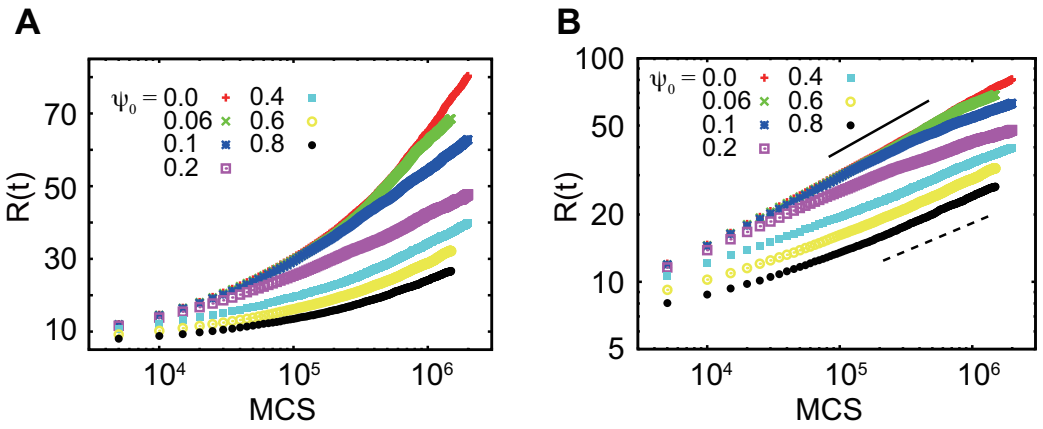

Figure 4.25: Time dependence of $R(t)$ for uneven ratios. The parameters are set as in Figure 4.24. The data are shown on the (A) semi-log and (B) log-log coordinates. The slopes of the solid and broken lines are $1/3$ and $1/4$, respectively.

shows a power-law growth at the late stage, and for $\psi_0 \sim 0.0$, $R(t)$ shows a power-law similar to that of $\psi_0 = 0$ at the intermediate stage. For $\psi_0 = 0.2$, the slope of the growth kinetics in the log-log plot seems to still change within our simulation time scale.

Although both $R(t)$ and $\gamma(t)$ seem to follow a power-law in t for $\psi_0 \geq 0.4$, their growth exponent seems different from those for $\psi_0 = 0$. We sum up the estimated values of growth exponent in Table 4.2. The data are fitted among the time interval $5 \times 10^5 <$ MCS $< 1.5 \times 10^6$. We show the results for $\psi_0 = 0$ and $\psi_0 \geq 0.4$. For $\psi_0 = 0$, the results obtained in the previous section are also shown. The exponents of $\psi_0 = 0$ are around 0.33, while those of $\psi_0 \geq 0.4$ are within the range $0.24 < n_{\rm eff} < 0.28$.

Measure	$\psi_0 = 0$	$\psi_0 = 0.4$	$\psi_0 = 0.6$	$\psi_0 = 0.8$
$\gamma(t)$	0.311 ± 0.001 $(0.31 \pm 0.01)^a$	0.255 ± 0.007	0.264 ± 0.004	0.269 ± 0.007 $(0.2733 \pm 0.0003)^b$
R	0.333 ± 0.002 $(0.33 \pm 0.02)^a$	0.242 ± 0.004	0.269 ± 0.008	0.264 ± 0.004 $(0.272 \pm 0.003)^b$

a. results of the previous section, b. $M = 768^2$.

Table 4.2: Effective growth exponents for two different measures of domain size

Domain morphology of clusters

To see the origin of the different kinetics, we have shown snapshots of the sorting process for the mixture ratios $\psi_0 = 0$, 0.2, and 0.6 in Figure 4.26. For $\psi_0 = 0$, the domains of each cell type show interconnected structures, while for $\psi_0 = 0.2$ and 0.6, the domains of minority cells (shown in gray in Fig. 4.26) have different morphologies. For $\psi_0 = 0.6$, the domains of minority cell types assume a spherical shape after the initial domain formation with nearby cells. For $\psi_0 = 0.2$, the domain morphologies are intermediate between the two cases. The domains with a small size have a spherical shape, while those with a large size have a deformed and elongated shape within the shown time scale. The difference in the domain structure between interconnected and spherical one seems to lead to the different kinetics.

To verify our hypothesis, we characterized the domain morphologies. To that end, we defined a shape factor [157] as,

$$s_i = \frac{64}{\pi}\frac{A_i}{l_i^2}, \tag{4.45}$$

where A_i and l_i are the area and perimeter length of i-th cluster, respectively. The prefactor $64/\pi$ normalizes the shape factor so that s_i satisfies $s_i = 1$ for circular domains on the square lattice. In contrast, convoluted clusters are characterized by $s_i << 1$. We also used an averaged shape factor of the system, which is defined as,

$$S = \frac{\sum_i A_i s_i}{\sum_i A_i}, \tag{4.46}$$

where the summation is taken over all domains of minority cells in the system. Figure 4.27 shows the s_i of all the clusters against A_i/A_{tot} for $\psi_0 = 0$, 0.1, and 0.8 at several time points. A_{tot} refers to the total area occupied by cells of the minority type. For $\psi_0 = 0$, while clusters are distributed over a wide range of A_i and s_i, the largest cluster is characterized by $A_i/A_{\text{tot}} \sim 1$ and $s_i \sim 0$ at all the shown time points. This corresponds to the percolated cluster with highly convoluted morphology as shown Fig. 4.26. For $\psi_0 = 0.8$, there is no cluster with $A_i/A_{\text{tot}} \sim 1$ or $s_i \sim 0$. At the late stage (MCS $= 1.5 \times 10^6$), s_i becomes $s_i \sim 1$ for all the clusters, which indicates that a large majority of domains assumes a circular morphology. For $\psi_0 = 0.1$, the situations are more subtle. Although there are many clusters with $s_i \sim 0$ at the early stage (MCS = 5×10^3), a majority of clusters assume $s_i > 0.5$ at the late stage (MCS = 1.5×10^6). The largest cluster also shows an increase in s_i at this stage.

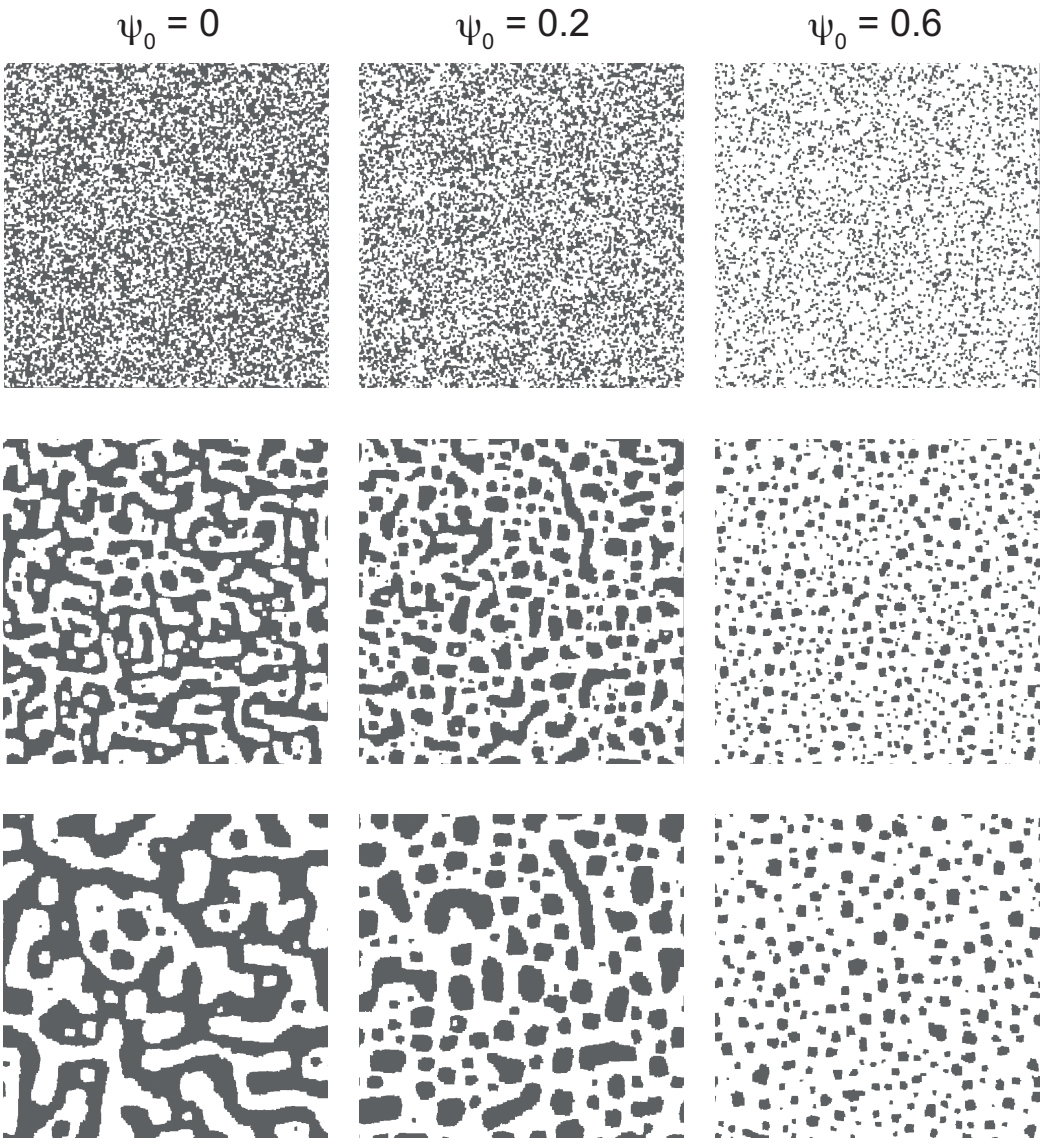

Figure 4.26: Different domain morphologies in the sorting process. Snapshots are shown for the mixture ratios $\psi_0 = 0$, 0.2 and 0.6. White: cells of $\tau = +1$, gray: cells of $\tau = -1$. The data are shown at the times MCS $= 0$ (top), 2×10^4 (center), and 1×10^5 (bottom). The number of cells is $N = 128^2$. $V_0 = 25$ and $L_0 = 20$.

We also showed the time dependence of S and s_i of the largest cluster (referred to as $s_{\rm lc}$) for $\psi_0 = 0$, 0.1, and 0.8 (Fig. 4.28). Reflecting the distribution of domain morphologies, S assumes stationary values for $\psi_0 = 0.0$ and 0.8, $S \sim 0.1$ for $\psi_0 = 0$ and $S \sim 1$ for $\psi_0 = 0.8$. In contrast, the S for $\psi_0 = 0.1$ does not assume a constant value, but continues to increase over the simulation time steps. This shows that the domains of the system are a mixture of convoluted and circular domains, and the proportion of circular domains grows with time. As seen in Figure 4.28, $s_{\rm lc}$ shows similar behaviors to S for $\psi_0 = 0$ and 0.8. For $\psi_0 = 0.1$, the $s_{\rm lc}$ stays $s_{\rm lc} \sim 0$ for MCS $\lesssim 10^5$, while $s_{\rm lc}$ shows a systematic increase for MCS $\gtrsim 10^5$. Around this time point, $R(t)$ of $\psi_0 = 0.1$ takes a clearly different value from that of $\psi_0 = 0$ (Fig. 4.25). This suggests that the domain morphology of the largest cluster is a good indicator for the sorting kinetics; the system with $s_{\rm lc} \sim 0$ shows the power-law domain growth with a growth exponent $n \sim 1/3$, and the system with $s_{\rm lc} \sim 1$ also shows the power-law domain growth with a growth exponent $n \sim 0.26$.

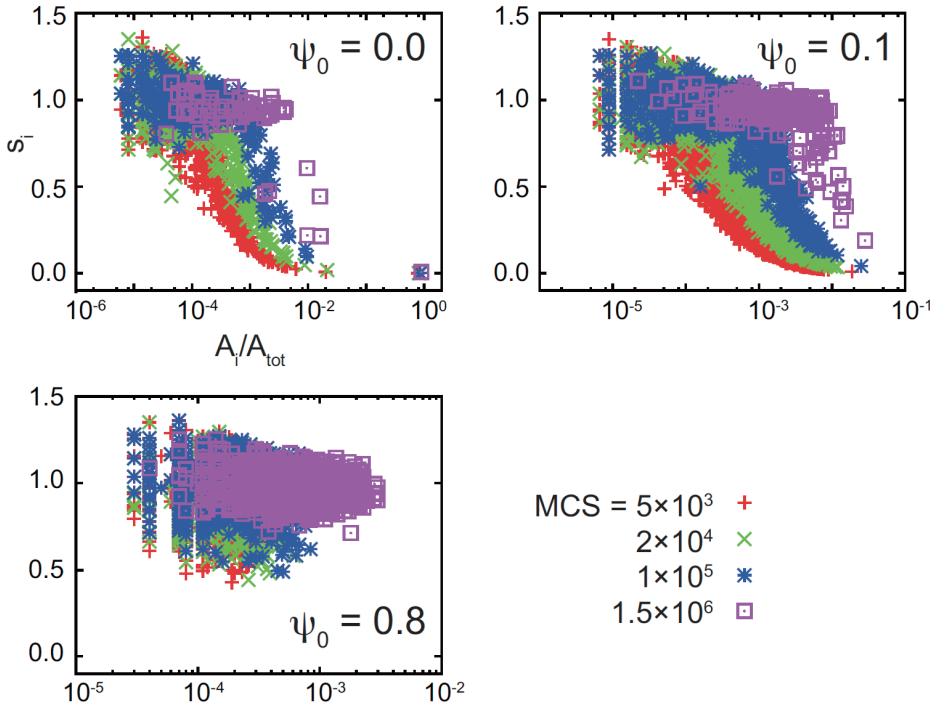

Figure 4.27: Distribution of shape factor s_i against $A_i/A_{\rm tot}$, where $A_{\rm tot} = (1 - \psi_0)N/2$.

To verify the power-law growth of unequal mixtures, the size distribution of clusters is investigated. From the dynamical scaling, the distribution is expected to obey,

$$P(A) = P_0(A/A_0), \tag{4.47}$$

where P_0 is a unique scaling function, A is the domain size, and A_0 is the average domain size. Figure 4.29A shows cumulative distribution of domain size for $\psi_0 = 0.8$. As representing the domain-growth, the distributions shift toward the larger domain size with time. Figure 4.29B shows the distribution as a function of rescaled domain size. The rescaled distributions lie on a unique scaling function at small domain size. At large domain sizes, although the rescaled distributions show a slight shift among the timescale $1 \times 10^5 <$ MCS $< 5 \times 10^5$, the distributions seems to lie on a single curve at a late stage, MCS $> 5 \times 10^5$. This scaling behavior supports the idea that the domain growth at $\psi_0 = 0.8$ shows the power-law behavior.

To summarize, the above results indicate that there exist two kinetics of domain growth for cell sorting in the CPM; both are power-law growth, one with the exponent $n \sim 1/3$ as seen in the even mixture ratio, and the other with the exponent $0.24 < n < 0.28$ in uneven mixtures. In the case of the even mixture, the domain-growth proceeds by smoothing the interface of the interconnected domains, driven by the surface tension. In the uneven case, the growth proceeds via the increase in the average size of circular domains. In addition, we should note that the behaviors of $R(t)$ for $\psi_0 = 0.1$ and 0.2 (shown in Fig. 4.25) are probably transient, and

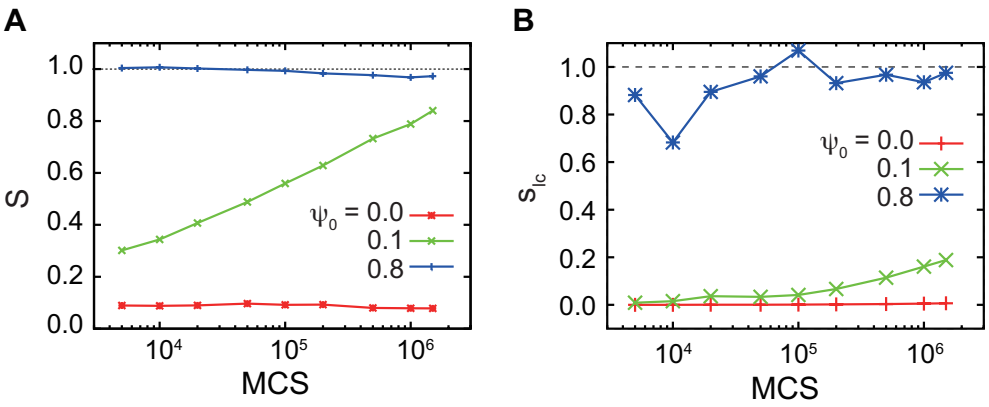

Figure 4.28: Time evolution of S and $s_{\rm lc}$.

at the later stage, it will asymptotically follow the power-law growth of circular domains.

Growth law for uneven mixtures

We now consider the reason why the exponent becomes smaller than $1/3$ in the domain growth of uneven mixtures. Two mechanisms have been proposed for the growth of circular domains in phase separation kinetics: the evaporation-condensation process (Fig. 4.12) and the direct coalescence of domains (Fig. 4.13). For model-B dynamics of unequal mixtures, the dominant mechanism is the evaporation-condensation process [157]. In the present case, it seems that this mechanism does not work since the cells are barely separated from a domain to which they originally belong. Instead, domain coarsening proceeds via diffusion and coalescence of cell domains. This is understood from a simple argument as follows. Consider a situation in which two neighboring cells of the same type are surrounded by cells of another type. To separate the neighboring cells, it is necessary to overcome an energy barrier posed by the replacement of homogeneous adhesions to heterogeneous ones. The probability that the replacement of just one homogeneous adhesion (not cell) occurs is given by

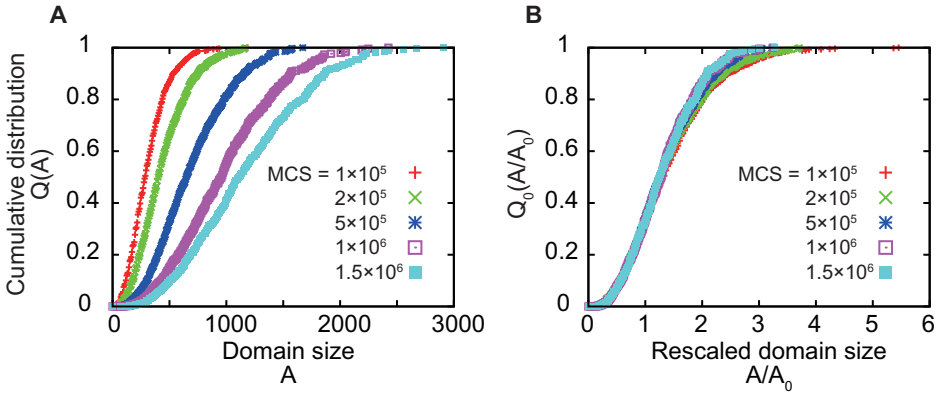

Figure 4.29: Cumulative distribution function of cluster size for $\psi_0 = 0.8$ at the shown time steps. Cumulative distribution function, $Q(A)$, is written as $Q(A) = \int_0^A P(A)dA$. $Q(A)$ is also expected to obey $Q(A) = Q_0(A/A_0)$ from the scaling of $P(A)$; Q_0 is a scaling function. (A) Naive cumulative distribution, (B) cumulative distribution as a function of A/A_0. A is the domain size (number of sites included in the domain), and A_0 is the average domain size.

$p_{site} = \exp(-\beta\Delta H_{\text{site}})$, where $\Delta H_{\text{site}} \sim (2J_{+-} - J_{++} - J_{--})$, while the probability that the replacement of all the adhesions occurs is $p_{cell} = \exp(-\beta\Delta H_{\text{cell}})$, where $\Delta H_{\text{cell}} \sim \sqrt{V_0}\Delta H_{\text{site}}$ (V_0 is the optimal cell area). The barrier accompanied by the separation of two cells is higher by a factor of $\sqrt{V_0}$ than that accompanied by the separation of a homogeneous bond. Because we have used the parameters $L_0 = 4\sqrt{V_0}$, $\tilde{J}_{++} = \tilde{J}_{--} = -300$ and $\tilde{J}_{+-} = -100$ (where $\tilde{J}_{\tau\tau'} = J_{\tau\tau'}L_0$), ΔH_{cell} is estimated as $\Delta H_{\text{cell}} \sim 100$. From this value and $\beta = 0.1$, the probability of separating the two homogeneous cells is estimated as $p_{cell} \sim \exp(-10) = 4.5 \times 10^{-5}$. The time scale this event occurs just once is given by p_{cell}^{-1}, which is comparable to the whole simulation time steps. Since the separation of homogeneous cells is necessary for the evaporation-condensation process, this mechanism does not work in the simulations of the CPM, at least within the timescales of the simulations in this thesis.

Hence, the diffusion and coalescence of cell domains should be the dominant mechanism. For the diffusion and coalescence mechanism, the time dependence of domain size is written as $L(t) \sim t^{1/(\gamma+2)}$ (Eq. (4.40)). γ is related to the diffusion coefficient of the cluster of radius R, as is given by $D(R) \sim R^{-\gamma}$. For a spherical particle in liquid in three dimensions, $\gamma = 1$ from the Einstein-Stokes relation, which leads to the growth exponent $1/3$. If the diffusion-and-coalescence process works in the sorting process of the CPM, the obtained growth exponent in uneven mixtures can be reproduced by investigating the domain-size dependence of the diffusion coefficient $D(R)$. To calculate the diffusion coefficient in two-dimensional CPM, we have considered a cluster of M_0 cells of one type ($\tau = +1$) as the initial condition and measured the displacement with time over many trials. Figure 4.30 shows the average displacement of a cluster for various value of M_0. In the long time scale, the displacement of cell clusters obeys $\sqrt{\langle|\Delta\mathbf{r}|^2\rangle} \sim t^{\frac{1}{2}}$, which implies that cell clusters move diffusively. From these data, we have estimated the diffusion coefficient with the usual relation for the diffusive process, $\langle|\Delta\mathbf{r}|^2\rangle = 2Dt$. We calculated the D for two cases: one is a cluster of M_0 cells of $\tau = +1$ surrounded by cells of the other type, and the other is a cluster of M_0 cells of $\tau = +1$ surrounded by the medium. For the latter case, the cluster can diffuse freely in the space since the energy constraint of the second and third terms of the Hamiltonian (4.1) does not work for the medium. Interfacial interaction energy is assigned as $\tilde{J}_{++} = \tilde{J}_{--} = -300$ and $\tilde{J}_{+-} = -100$ for the former and as $\tilde{J}_{++} = -300$, $\tilde{J}_{mm} = 0$, $\tilde{J}_{+m} = -100$ for the latter, where m means the medium.

Figure 4.30B shows the result obtained for D as a function of M_0. For clusters surrounded by the medium, the D decreases with M as $D \sim M_0^{-1}$. This relation

is understood from the following discussion. Consider that the motion of each cell in the cluster is modeled as $\dot{\mathbf{r}}_i = \sum_j \mathbf{f}_{ij} + \boldsymbol{\xi}_i$, where $\mathbf{r}_i$ is the position of the cell i, $\mathbf{f}_{ij}$ is interactions between cells i and j, $\boldsymbol{\xi}_i$ is random force to cell i, and summation of j is taken over interacting neighbors. The motion of the cluster position, center of mass of cells, obeys $\dot{\mathbf{r}} = \frac{d}{dt}(\frac{1}{M_0}\sum_i \mathbf{r}_i) = \frac{1}{M_0}\sum_i \boldsymbol{\xi}_i = \frac{1}{\sqrt{M_0}}\boldsymbol{\xi}$, where the random variable $\boldsymbol{\xi}$ has the same statistical property with $\boldsymbol{\xi}_i$. Here the summation of interacting forces is canceled out since we assumed $\mathbf{f}_{ij} = -\mathbf{f}_{ji}$. The relation $D \sim M_0^{-1}$ is then reproduced as $\langle|\Delta\mathbf{r}|^2\rangle = \frac{1}{M_0}\langle|\boldsymbol{\xi}|^2\rangle = 2(\frac{D_0}{M_0})t = 2Dt$, where $\langle|\Delta\mathbf{r}|^2\rangle$ is the average displacement of the cluster and D_0 is the intensity of noise, given as $\langle|\boldsymbol{\xi}|^2\rangle = 2D_0$.

For clusters surrounded by cells of the other type, D decreases more slowly for small M_0, where the slope is around $-3/4$. However, as the M_0 increases, the slope becomes steeper and D seems to obey the relation $D \sim M_0^{-1}$ for relatively large M_0 ($M_0 > 10^2$). We have investigated the sorting and diffusion of a cluster in the CPM with the Neumann-neighborhood interactions (interactins with the four nearest sites) for the first term of the Hamiltonian (4.1). Because the simulation of Neumann-neighborhood interactions is susceptible to the lattice effect, we have also calculated the diffusion coefficient in the CPM with Moore-neighborhood interactions (interaction with the eight surrounding sites). Figure 4.31 shows the result. Also for the Moore-neighborhood interactions, D seems to obey the relation $D \sim M_0^{-1}$ for large M_0 although the slope of D for clusters surrounded by other cells seems to depend on V_0.

Why does M_0 dependence of D differ between the two cases (being surrounded by the medium and by other cells)? There is an additional energy barrier originating from the surroundings for the diffusion of a cluster surrounded by cells of other types, as compared to the case of a cluster surrounded by medium. In the case of small M_0, this additional energy barrier should change the kinetics of the cluster since the size of cluster is comparable to that of a single cell. On the other hand, in the case of large M_0, the effect of single-cell length scale probably becomes negligible since the length scale of the cluster is far from that of a single cell. Therefore the asymptotic behavior of diffusion to large M_0 should be $D \sim M_0^{-1}$ also for clusters surrounded by cells of other types.

Assuming that the clusters take a circular shape, the diffusion coefficient as a function of the cluster radius obeys $D \sim R^{-2}$ for $D \sim M_0^{-1}$. This leads to the growth exponent $n = 1/(\gamma + 2) = 1/4$. In the case of $\psi_0 = 0.8$, the estimated exponent from the simulations is $0.264 \leq n_{\text{eff}} \leq 0.269$ for $M = 512^2$ (M is total cell number in the system), and $n_{\text{eff}} \sim 0.272$ for $M = 768^2$ (see Table 4.2).

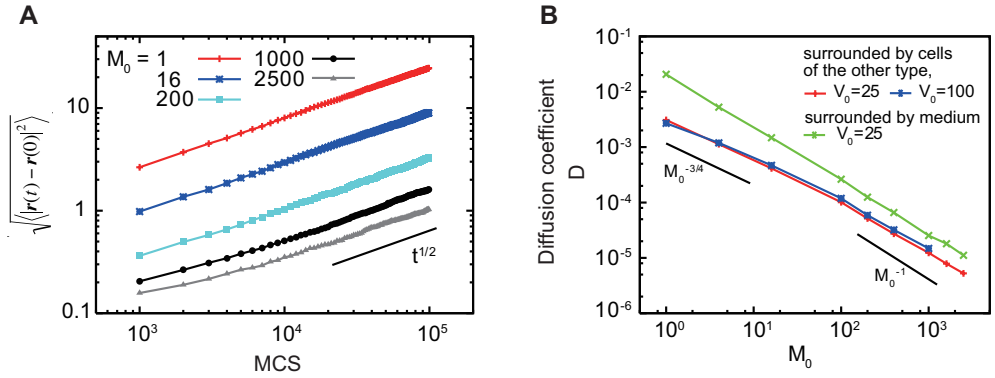

Figure 4.30: Diffusion of a cluster of cells for Neumann-neighborhood interactions. (A) Average displacement of a cluster. The data are averaged over 1000 trials for $M_0 <= 100$ and 400 trials for $M_0 > 100$. (B) Diffusion coefficient D as a function of M_0.

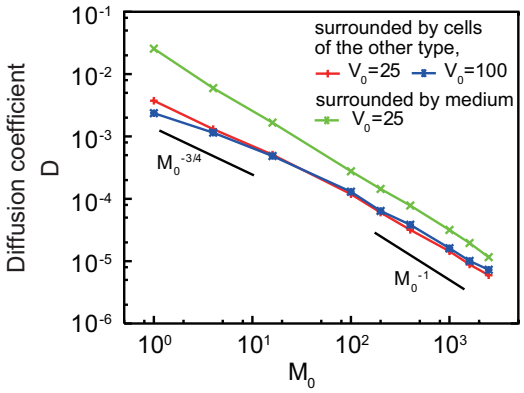

Figure 4.31: Diffusion of a cluster of cells for Moore-neighborhood interactions. Diffusion coefficient D as a function of M_0. D is estimated from the data averaged over 400 trials.

These values are compatible but slightly higher than $1/4$. This slight discrepancy is attributed to the M_0 dependence of D for a cluster surrounded by other cells (Fig. 4.30). The cluster radius R is related to M_0 as $R \simeq \sqrt{V_0 M_0/\pi}$. For the sorting simulation in Figure 4.24 and 4.25, the V_0 is set as $V_0 = 25$. The diffusion coefficient seems to obey $D \sim R^{-2}$ for $M_0 > 100$, which corresponds to $R > 28$.

In contrast, for small clusters with $R < 28$, the slope of $D(M_0)$ is around $-3/4$, which leads to the growth exponent $n = 2/7$. Since the characteristic correlation length of the sorting simulation is around $R(t) = 30$ at the most for $\psi_0 = 0.8$ (Fig. 4.25), it is feasible that the effective growth exponent increases to more than $1/4$. Indeed the effective exponent stays in the range $2/7 < n_{\text{eff}} < 1/4$ as expected from $D(M_0)$, which is consistent with the phenomenological explanation. Finally, we should note that a more extensive simulation is necessary since the data of $R(t)$ and $\gamma(t)$ is required over a longer time scale to evaluate the correct exponent.

4.5 Extended Cellular Potts Model with polarized motion

We have shown that the kinetics of the CPM exhibits the power-law growth in both cases, for the even and uneven mixture ratios of two cell types. Thus the domain-growth of the CPM proceeds much faster than previously believed [54,125]. However, the kinetics of the CPM remain slower than the experimental observations, in which the size of cellular domains grows linearly with time. Then, how does the difference in the sorting kinetics arise? One possibility is that the cells do not move randomly but show a directed motion via cell polarity and coordination among neighboring cells. So far, the spontaneous organization of the correlated motion of cells is reported in several systems such as the aggregates of *Dictyosterium* cells [150] and cultured epithelial cells [59]. Such movements are also observed in the sorting of hydra [155], which could accelerate the sorting process.

Hence we extended the model, to incorporate polarized movement of cells. The effective energy is now given by,

$$\mathcal{H} = \mathcal{H}_{\text{CPM}} - \lambda_P \sum \mathbf{u}_\sigma \cdot \mathbf{r}_\sigma. \tag{4.48}$$

The first term on the right-hand side represents the Hamiltonian of the original CPM (Eq. (4.1)). The second term is a new one incorporating a polarized motion of cells, where $\mathbf{u}_\sigma$ and $\mathbf{r}_\sigma$ are the polarity and center of mass of σ-th cell, respectively. This term refers to the fact that the cells tend to move toward the polarized directions. $\mathbf{u}_\sigma$ is updated depending on their own direction and the interactions

among surrounding cells. The update rule is given by,

$$\begin{aligned}\Delta\mathbf{u}_{\sigma,t+1} &= (1-|\mathbf{u}_{\sigma,t}|^2)\mathbf{u}_{\sigma,t} - \gamma_1 \sum_{\sigma'} L_{\sigma\sigma'}\Delta P_{\sigma\sigma'}\mathbf{n}_{\sigma\sigma'} \\ &\quad +\gamma_2 \sum_{\sigma'} A_{\tau\tau'} L_{\sigma\sigma'}\Delta\mathbf{u}_{\sigma\sigma',t} + \xi_{\sigma,t}. \end{aligned} \tag{4.49}$$

where $\Delta\mathbf{u}_{\sigma,t+1} = \mathbf{u}_{\sigma,t+1} - \mathbf{u}_{\sigma,t}$, $\Delta P_{\sigma\sigma'} = (P_{\sigma'} - P_\sigma)$, $\mathbf{n}_{\sigma\sigma'} = \frac{\mathbf{r}_{\sigma'}-\mathbf{r}_\sigma}{|\mathbf{r}_{\sigma'}-\mathbf{r}_\sigma|}$ and $\Delta\mathbf{u}_{\sigma\sigma',t} = (\mathbf{u}_{\sigma',t} - \mathbf{u}_{\sigma,t})$. $L_{\sigma\sigma'}$ refers to the length of interface between cells σ and σ' The first term of Equation (4.49) refers to the spontaneous cell polarization. This term makes cells take a polarized state, $|\mathbf{u}_{\sigma,t}| = 1$, without intercellular interactions. The second term expresses the effect of local pressure from neighboring cells directed to the normal to cell-cell interface. The pressure is defined as

$$P_\sigma \equiv -(\delta\mathcal{H}/\delta V_\sigma), \tag{4.50}$$

which is approximated by $P_\sigma \simeq -2\lambda_V(V_\sigma - V_0) - 2\lambda_L(L_\sigma - L_0)\sqrt{\pi/V_\sigma}$. Here we assume that the cells take a spherical shape of volume V_0. The third term in Equation (4.49) represents the tendency of the cells to correlate their polarity toward the same direction through mechanical and/or chemical signal transductions via cell adhesion. $A_{\tau\tau'}$ is the interaction strength between a pair of cells. The strength of the correlating cell polarities could be different based on the types of a pair of interacting cells. The fourth term refers to the noise with statistical characteristics $\langle\xi_\sigma\rangle = 0$ and $\langle\xi_{\sigma,t}\xi_{\sigma',t'}\rangle = D\delta_{\sigma\sigma'}\delta_{tt'}$. We set the parameters as $\gamma_1 = 10^{-4}$, $\gamma_2 = 10^{-5}$, $D = 10^{-4}$. Here, we extended the original CPM to describe polarized cellular movement. In this extended model, cell polarity and intercellular coupling of the polarities are phenomenologically incorporated. This model does not satisfy the detailed balance and thus assumes a non-equilibrium condition. This is because we have assumed that fluctuations in Eq. (4.48) and (4.49) arise independently. In addition, we should note that cellular movements and cell sorting process are originally far from the equilibrium.

We show the results of the numerical simulations for the following two cases:

case I. interactions with the same strength among all the cell types:

$A_{\tau\tau'} = A_0 = 10.0$

case II. interactions only between the same types of cells:

$A_{11} = A_{22} = 15$, $A_{12} = A_{21} = 0$

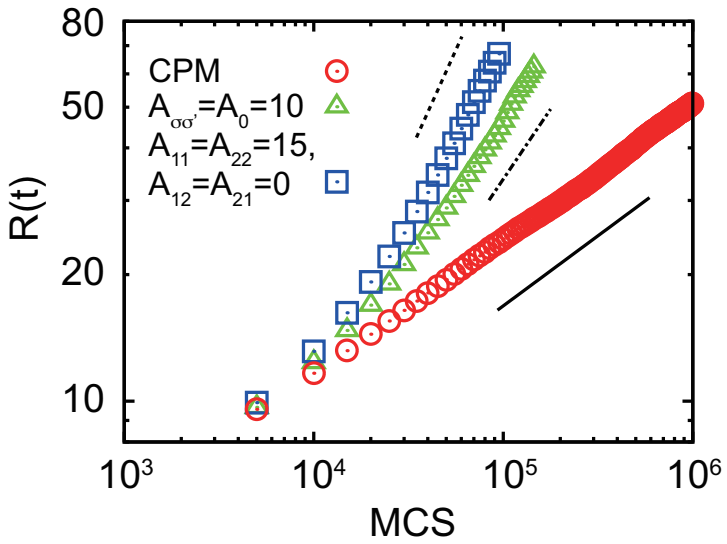

Figure 4.32: (A) Domain growth of the cell-sorting process in the extended model in two dimensions. The simulations are carried out with $M = 512^2$. Solid, broken, and dotted lines with the slopes $1/3$, $2/3$, and 1 are shown. (B) Correlated motion of neighboring cells.

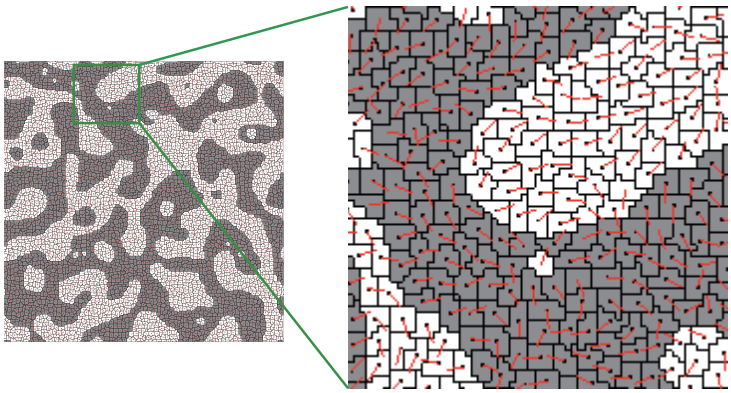

Figure 4.33: (B) Correlated motion of neighboring cells.

	CPM	extended CPM (case I)	extended CPM(case II)
R	0.34 ± 0.01 ($10^5 <$ MCS $< 10^6$)	0.68 ± 0.03 ($5 \times 10^4 <$ MCS $< 10^5$)	0.88 ± 0.12 ($5 \times 10^4 <$ MCS $< 10^5$)

Table 4.3: Effective growth exponents for the extended CPM

The time dependence of $R(t)$ for the two cases is shown along with the result of the CPM in Figure 4.32. The mixture ratio is set as $\psi_0 = 0$. As shown in the figure, the inclusion of polarized movement induces much faster growth of the domain size, compared to the result of the original CPM. Indeed, the inclusion induces the correlated motion of neighboring cells (shown in Fig 4.33).

We have estimated the growth exponents of $R(t)$ of the extended model, and the results are listed in Table 4.3. In case I, the domain growth in two-dimensional simulations results in the power-law growth with the exponent $n_{\text{eff}} = 0.68 \pm 0.03$. In case II, the domain growth in two-dimensional simulations results in the power-law with $n_{\text{eff}} = 0.88 \pm 0.12$. These exponents are much larger than the results of the original CPM, and the exponent of the case II is similar with the experimental observations. In the extended model, cells exhibit a polarized movement. Thus, our results indicate that the cooperative movement of cells is crucial for the quick progress of cell sorting.

4.6 Discussion

In this chapter, we have numerically investigated the kinetics of cell sorting. First, we re-examined the growth kinetics of the CPM and showed that the model exhibits not a logarithmic, but power-law growth in domain size. We have observed two regimes of power-law growth in the CPM, one has the growth exponent $n \simeq 0.33$ for the mixture ratio $50 : 50$, and the other has the exponent $n \simeq 0.26$ for uneven mixtures. Second, we extended the model to incorporate polarized and correlated movement of cells. The extended model exhibited a domain growth faster than that of the original CPM. The obtained exponent is $n \simeq 0.68$ and 0.88, depending on the interactions among neighboring cells. The results indicate that the active and collective movement is crucial for the quick progress of the sorting process, which could contribute to the developmental robustness in tissue morphogenesis.

Two power-law regimes of the CPM

The growth exponent of even mixture is close to that of the model B, where the order parameter is transported diffusively. This exponent is consistent with a view that each cell moves diffusively via random ruffling of cell surfaces in the CPM [53, 126]. The other growth exponent of uneven mixtures seems to come from the diffusion-and-coalescence mechanism of domain growth for circular domains. The size dependence of the diffusion coefficient has a power-law dependence, $D(R) \propto R^{-2}$ for large clusters (Fig. 4.30), which should lead to the growth exponent $n = 1/4$. Still, we could not rule out the possibility that the growth exponent of uneven mixtures might also approach $n = 1/3$ after a much longer time scale. We should note that we have paid attention to the sorting kinetics observed within the simulation time scale, and we believe that the different dominant mechanisms result in the distinct sorting kinetics for even and uneven mixture ratio.

From the experimental point of view, the size dependence of the diffusion coefficient is probably easier to measure than the domain growth kinetics. By measuring the diffusion coefficient of the cell cluster, it will be possible to estimate the driving force for the cell cluster, and check whether the diffusive motion of cells is dominant as in the CPM, or if there are other components to it. Since the reason for $D(R) \sim R^{-2}$ is quite natural, it could be a starting point to discuss the motion of a cell cluster. The kinetics of cell clusters is important for the understanding of metastasis and many developmental processes; thus, further investigation of numerical models and experiments on the behavior of cell aggregates is needed.

Quick sorting behavior of cellular aggregates

As already mentioned, Beysens *et al.* reported that the sorting of the chick epithelial and retinal cells progresses with linear domain growth (Fig. 4.9) [14]. This is much faster than the kinetics of the original CPM. From our analysis, correlated movement of neighboring cells is implicated to contribute to this quick progress of cell sorting. In the case of the hydra aggregates of endodermal and ectodermal cells [155], such a cellular flow has been observed during the sorting process. Another possibility of the linear growth is that it arises not from the collective movement of cells but from the hydrodynamic effect of the culture medium surrounding cells. However, this is not plausible since the estimated viscosity of the cell aggregate is much larger than the usual liquid by orders of magnitude around $10^7 \sim 10^8$ [14, 41].

If the correlated movement of cells is necessary for the quick cell sorting and rearrangement, the cell motility and adhesive property should affect the macroscopic behavior of the tissue. For chick neural retina aggregates in three dimensions, the shape relaxation time of the deformed aggregates was estimated [127]. It is expected to be proportional to the aggregate radius if the chick-cell aggregates behave similarly with hydra-cell aggregates [156]. Instead, the power-law dependence with the slope $3/2$ was obtained, that is $\tau(R) \propto R^{3/2}$. This indicates that the chick neural retina aggregates behave slower than hydra endodermal aggregate. Cell types might introduce a crucial difference in the kinetics such as cellular rearrangement and sorting, in the tissue morphogenesis.

Cellular aggregates as complex active fluid

Actin networks and cell populations are assumed to behave as a complex active fluid [81, 162, 190]. For example, the spontaneous ordering of a directed movement is observed in a sheet of fibroblasts [59], and the spontaneous ordering of a rotational motion is observed in aggregates of Dictyosterium cells [150]. An interfacial pattern such as viscous-fingering via active movement toward the vacancy emerged in the epithelial wound healing of MDCK cells [146]. In addition to such *in vitro* experiments, Schotz *et at.* [163] indicated that the robust velocity profiles observed in the epiboly of zebrafish embryo cannot be explained by adopting the usual Newtonian fluid. Since the zebrafish cells show the active flow of cell motion in the epiboly, the properties of cell populations as an active fluid could be indeed important for such developmental processes.

Chapter 5

Summary and concluding remarks

Here, we studied how biological systems achieve the elaborate coordination seen in various developmental processes. First, we studied the temporal expression patterning of neural stem cells in *Drosophila* neurogenesis (chapter 2). Comparing the expression patterns of empirical data and of numerical models, we identified the requisite regulations and predicted an unknown factor to reproduce known expression profiles. From the analysis of the expression stability of the networks, the *Drosophila* temporal patterning network was noted to have a regulatory module to achieve robust sequential expression. We found that dynamic expression patterns in development could be also regulated in the single-cell level regulation embedded in network architecture. Since intercellular interactions are important in many developmental processes, we next studied the robust differentiation strategy via intercellular signaling (chapter 3). A proposed mechanism to produce cell diversity is based on the self-consistent tuning of the bifurcation parameter of dynamical systems. As a simple biologically applicable example, we showed that the bistability generated by one of the most simple network motif, positive-feedback, was shown to lead to different regulation behaviors of populations by the inclusion of intercellular interactions. This indicates that in some cases, the single-cell level behavior is tuned to meet the population-level requirements in development. These strategies to make developmental systems robust via chemical networks. The physical and mechanical properties of tissues should also be important for morphogenesis. As cell aggregates are considered to behave like a fluid, we focused on the conditions under which they could be assumed to be so. For this, we investigated the segregation kinetics of cell sorting of the original and extended versions of the Cellular Potts Model (chapter 4). The results of the original CPM demonstrated the power-law behavior of the model; the ran-

dom movement of cells alone is not enough to explain the fast sorting process of the experiments. In contrast, the extended model shows fast sorting, which indicates that the collective movement of cells is necessary for the emergence of "the hydrodynamic effects" in cell aggregates.

To summarize, we have studied the strategies underlying robust development at several hierarchical levels. Further work is required to understand, and, more importantly, bridge the molecular, cellular, and tissue-level descriptions. We hope that the work in this thesis will provide some insights for further investigations.

Bibliography

[1] Gregor B Adams and David T Scadden. The hematopoietic stem cell in its place. *Nat Immunol*, 7(4):333–7, Apr 2006.

[2] M Akam. The molecular basis for metameric pattern in the drosophila embryo. *Development*, 101(1):1–22, 1987.

[3] Bruce Alberts, Alexander Johnson, Julian Lewis, Martin Raff, Keith Roberts, and Peter Walter. *Molecular biology of the cell, 4th edition*. Garland Science, 4th edition edition, 2002.

[4] FJ Alexander, S Chen, and DW Grunau. Hydrodynamic spinodal decomposition: Growth kinetics and scaling functions. *Physical Review B*, 48(1):634–637, 1993.

[5] Uri Alon. *An introduction to systems biology: design principles of biological circuits*. Chapman & Hall, 2006.

[6] Elisa Alvarez-Curto, Shweta Saran, Marcel Meima, Jenny Zobel, Claire Scott, and Pauline Schaap. camp production by adenylyl cyclase g induces prespore differentiation in dictyostelium slugs. *Development*, 134(5):959–66, Mar 2007.

[7] JG Amar, FE Sullivan, and RD Mountain. Monte carlo study of growth in the two-dimensional spin-exchange kinetic ising model. *Physical Review B*, 37(1):196–208, 1988.

[8] Fumio Arai, Atsushi Hirao, Masako Ohmura, Hidetaka Sato, Sahoko Matsuoka, Keiyo Takubo, Keisuke Ito, Gou Young Koh, and Toshio Suda. Tie2/angiopoietin-1 signaling regulates hematopoietic stem cell quiescence in the bone marrow niche. *Cell*, 118(2):149–61, Jul 2004.

[9] NJ Armstrong, KJ Painter, and JA Sherratt. A continuum approach to modelling cell–cell adhesion. *Journal of Theoretical Biology*, 243(1):98–113, 2006.

[10] N Barkai and S Leibler. Robustness in simple biochemical networks. *Nature*, 387(6636):913–7, 1997.

[11] S Bastea and JL Lebowitz. Domain growth in computer simulations of segregating two-dimensional binary fluids. *Phys. Rev. E*, 52(4):3821–3826, 1995.

[12] Julio M Belmonte, Gilberto L Thomas, Leonardo G Brunnet, Rita M. C De Almeida, and Hugues Chaté. Self-propelled particle model for cell-sorting phenomena. *Physical Review Letters*, 100(24):4, Jun 2008.

[13] M Benoit, D Gabriel, G Gerisch, and H E Gaub. Discrete interactions in cell adhesion measured by single-molecule force spectroscopy. *Nat Cell Biol*, 2(6):313–7, Jun 2000.

[14] DA Beysens, G Forgacs, and JA Glazier. Cell sorting is analogous to phase ordering in fluids. *Proceedings of the National Academy of Sciences*, 97(17):9467–9471, 2000.

[15] K Binder. Theory for the dynamics of" clusters." ii. critical diffusion in binary systems and the kinetics of phase separation. *Physical Review B*, 15(9):4425–4447, 1977.

[16] K Binder. Theory of first-order phase transitions. *Rep. on progress in physics*, 50(7):783–859, 1987.

[17] AJ Bray. Universal scaling function for domain growth in the glauberising chain. *Journal of Physics A: Mathematical and General*, 23:L67–L72, 1990.

[18] AJ Bray. Theory of phase-ordering kinetics. *Advances in Physics*, 43(3):357–459, 1994.

[19] T Brody and WF Odenwald. Programmed transformations in neuroblast gene expression during drosophila cns lineage development. *Dev Biol*, 226(1):34–44, 2000.

[20] Laura M Calvi. Osteoblastic activation in the hematopoietic stem cell niche. *Annals of the New York Academy of Sciences*, 1068:477–88, Apr 2006.

[21] Alan B Cantor and Stuart H Orkin. Transcriptional regulation of erythropoiesis: an affair involving multiple partners. *Oncogene*, 21(21):3368–76, May 2002.

[22] EE Caygill and LA Johnston. Temporal regulation of metamorphic processes in drosophila by the let-7 and mir-125 heterochronic microrna. *Curr Biol*, 18(13):943–50, 2008.

[23] AC Cerny, G Bucher, R Schroder, and M Klingler. Breakdown of abdominal patterning in the tribolium kruppel mutant jaws. *Development*, 132(24):5353–5363, 2005.

[24] A Chakrabarti, R Toral, and JD Gunton. Late stages of spinodal decomposition in a three-dimensional model system. *Physical Review B*, 39(7):4386–4394, 1989.

[25] A Chakrabarti, R Toral, and JD Gunton. Late-stage coarsening for off-critical quenches: Scaling functions and the growth law. *Phys. Rev. E*, 47(5):3025–3038, 1993.

[26] H Chen and A Chakrabarti. Hydrodynamic effects on domain growth in off-critical polymer blends. *The Journal of Chemical Physics*, 108:6006, 1998.

[27] YC Chou and WI Goldburg. Phase separation and coalescence in critically quenched isobutyric-acid—water and 2, 6-lutidine—water mixtures. *Physical Review A*, 20(5):2105–2113, 1979.

[28] Yeh-Shiu Chu, William A Thomas, Olivier Eder, Frederic Pincet, Eric Perez, Jean Paul Thiery, and Sylvie Dufour. Force measurements in e-cadherin-mediated cell doublets reveal rapid adhesion strengthened by actin cytoskeleton remodeling through rac and cdc42. *The Journal of Cell Biology*, 167(6):1183–94, Dec 2004.

[29] S Ciliberti, OC Martin, and A Wagner. Robustness can evolve gradually in complex regulatory gene networks with varying topology. *PLoS Comput Biol*, 3(2):e15, 2007.

[30] MD Cleary and CQ Doe. Regulation of neuroblast competence: multiple temporal identity factors specify distinct neuronal fates within a single early competence window. *Genes Dev*, 20(4):429–34, 2006.

[31] A Coniglio and M Zannetti. Multiscaling in growth kinetics. *EPL (Europhysics Letters)*, 10:575–580, 1989.

[32] Eric H Davidson, Jonathan P Rast, Paola Oliveri, Andrew Ransick, Cristina Calestani, Chiou-Hwa Yuh, Takuya Minokawa, Gabriele Amore, Veronica Hinman, Cesar Arenas-Mena, Ochan Otim, C Titus Brown, Carolina B Livi, Pei Yun Lee, Roger Revilla, Alistair G Rust, Zheng jun Pan, Maria J Schilstra, Peter J C Clarke, Maria I Arnone, Lee Rowen, R Andrew Cameron, David R McClay, Leroy Hood, and Hamid Bolouri. A genomic regulatory network for development. *Science*, 295(5560):1669–78, Mar 2002.

[33] D G Davies, M R Parsek, J P Pearson, B H Iglewski, J W Costerton, and E P Greenberg. The involvement of cell-to-cell signals in the development of a bacterial biofilm. *Science*, 280(5361):295–8, Apr 1998.

[34] Smadar Ben-Tabou de Leon and Eric H Davidson. Gene regulation: gene control network in development. *Annual review of biophysics and biomolecular structure*, 36:191, Jan 2007.

[35] Andrew W Duncan, Frédérique M Rattis, Leah N Dimascio, Kendra L Congdon, Gregory Pazianos, Chen Zhao, Keejung Yoon, J Michael Cook, Karl Willert, Nicholas Gaiano, and Tannishtha Reya. Integration of notch and wnt signaling in hematopoietic stem cell maintenance. *Nat Immunol*, 6(3):314–22, Mar 2005.

[36] Lluís Espinosa, Julia Inglés-Esteve, Cristina Aguilera, and Anna Bigas. Phosphorylation by glycogen synthase kinase-3 beta down-regulates notch activity, a link for notch and wnt pathways. *J Biol Chem*, 278(34):32227–35, Aug 2003.

[37] R Farhadifar, JC Röper, B Aigouy, S Eaton, and F Jülicher. The influence of cell mechanics, cell-cell interactions, and proliferation on epithelial packing. *Current Biology*, 17(24):2095–2104, 2007.

[38] JE Farrell and OT Valls. Spinodal decomposition in a two-dimensional fluid model. *Physical Review B*, 40(10):7027–7039, 1989.

[39] J E Ferrell and E M Machleder. The biochemical basis of an all-or-none cell fate switch in xenopus oocytes. *Science*, 280(5365):895–8, May 1998.

[40] Malcolm E Fisher, Harry V Isaacs, and Mary E Pownall. efgf is required for activation of xmyod expression in the myogenic cell lineage of xenopus laevis. *Development*, 129(6):1307–15, Mar 2002.

[41] G Forgacs, RA Foty, Y Shafrir, and MS Steinberg. Viscoelastic properties of living embryonic tissues: a quantitative study. *Biophysical Journal*, 74(5):2227–2234, 1998.

[42] G Forgacs and S Newman. Biological physics of the developing embryo. *Cambridge University Press*, Jan 2005.

[43] R Foty, G Forgacs, and C Pfleger. Liquid properties of embryonic tissues: Measurement of interfacial tensions. *Physical Review Letters*, Jan 1994.

[44] RA Foty, CM Pfleger, G Forgacs, and MS Steinberg. Surface tensions of embryonic tissues predict their mutual envelopment behavior. *Development*, 122(5):1611–1620, 1996.

[45] M Freeman and J B Gurdon. Regulatory principles of developmental signaling. *Annu. Rev. Cell. Dev. Biol.*, 18:515–39, Jan 2002.

[46] K Fujimoto, S Ishihara, and K Kaneko. Network evolution of body plans. *PLoS One*, 3(7):e2772, 2008.

[47] H Furukawa. A dynamic scaling assumption for phase separation. *Advances in Physics*, 34(6):703–750, Jan 1985.

[48] H Furukawa. Role of inertia in the late stage of the phase separation of a fluid. *Physica A Statistical Mechanics and its Applications*, 204:237–245, 1994.

[49] C Furusawa and K Kaneko. Emergence of rules in cell society: differentiation, hierarchy, and stability. *Bull. Math. Biol.*, 60(4):659–87, Jul 1998.

[50] Chikara Furusawa and Kunihiko Kaneko. Origin of multicellular organisms as an inevitable consequence of dynamical systems. *Anat. Rec.*, 268(3):327–42, Nov 2002.

[51] Jordi Garcia-Ojalvo, Michael B Elowitz, and Steven H Strogatz. Modeling a synthetic multicellular clock: repressilators coupled by quorum sensing. *Proc Natl Acad Sci USA*, 101(30):10955–60, Jul 2004.

[52] Scott F. Gilbert. *Developmental Biology, 8th edition*. Sinauer Associates Inc., 2006.

[53] J Glazier and F Graner. Simulation of the differential adhesion driven rearrangement of biological cells. *Physical review E, Statistical physics, plasmas, fluids, and related interdisciplinary topics*, 47(3):2128–2154, Mar 1993.

[54] F Graner and J Glazier. Simulation of biological cell sorting using a two-dimensional extended potts model. *Phys. Rev. Lett.*, Jan 1992.

[55] I Greenwald and G M Rubin. Making a difference: the role of cell-cell interactions in establishing separate identities for equivalent cells. *Cell*, 68(2):271–81, Jan 1992.

[56] R Grosskortenhaus, BJ Pearson, A Marusich, and CQ Doe. Regulation of temporal identity transitions in drosophila neuroblasts. *Dev Cell*, 8(2):193–202, 2005.

[57] R Grosskortenhaus, KJ Robinson, and CQ Doe. Pdm and castor specify late-born motor neuron identity in the nb7-1 lineage. *Genes Dev*, 20(18):2618–27, 2006.

[58] J B Gurdon, P Lemaire, and K Kato. Community effects and related phenomena in development. *Cell*, 75(5):831–4, Dec 1993.

[59] H Haga. Collective movement of epithelial cells on a collagen gel substrate. *Biophysical Journal*, 88(3):2250–2256, Dec 2004.

[60] R S Hartley, R E Rempel, and J L Maller. In vivo regulation of the early embryonic cell cycle in xenopus. *Developmental Biology*, 173(2):408–19, Feb 1996.

[61] T Hashimoto, M Itakura, and H Hasegawa. Late stage spinodal decomposition of a binary polymer mixture. i. critical test of dynamical scaling on scattering function. *The Journal of Chemical Physics*, 85:6118, 1986.

[62] T Hashimoto, M Itakura, and N Shimidzu. Late stage spinodal decomposition of a binary polymer mixture. ii. scaling analyses on q (τ) and i (τ). *The Journal of Chemical Physics*, 85:6773, 1986.

[63] Jonne Helenius, Carl-Philipp Heisenberg, Hermann E Gaub, and Daniel J Muller. Single-cell force spectroscopy. *Journal of Cell Science*, 121(Pt 11):1785–91, Jun 2008.

[64] T Hirashima, Y Iwasa, and Y Morishita. Dynamic modeling of branching morphogenesis of ureteric bud in early kidney development. *Journal of Theoretical Biology*, 2009.

[65] R M Hochmuth. Micropipette aspiration of living cells. *J Biomech*, 33(1):15–22, Jan 2000.

[66] PC Hohenberg and BI Halperin. Theory of dynamic critical phenomena. *Reviews of Modern Physics*, 49(3):435–479, 1977.

[67] J Holtfreter. Experimental studies on the development of the pronephros. *Rev. Can. Biol.*, 3:220, Jan 1944.

[68] H Honda. Geometrical models for cells in tissues. *International review of cytology*, Jan 1983.

[69] H Honda, M Tanemura, and T Nagai. A three-dimensional vertex dynamics cell model of space-filling polyhedra simulating cell behavior in a cell aggregate. *Journal of Theoretical Biology*, 226(4):439–453, 2004.

[70] N A Hopper, A J Harwood, S Bouzid, M Véron, and J G Williams. Activation of the prespore and spore cell pathway of dictyostelium differentiation by camp-dependent protein kinase and evidence for its upstream regulation by ammonia. *EMBO J*, 12(6):2459–66, Jun 1993.

[71] K Humayun and AJ Bray. Non-equilibrium dynamics of the ising model for t less-than/equal-totc. *Journal of Physics A: Mathematical and General*, 24:1915–1930, 1991.

[72] D Huse. Corrections to late-stage behavior in spinodal decomposition: Lifshitz-slyozov scaling and .... *Physical Review B*, Jan 1986.

[73] Kaoru S Imai, Michael Levine, Nori Satoh, and Yutaka Satou. Regulatory blueprint for a chordate embryo. *Science*, 312(5777):1183–7, May 2006.

[74] NT Ingolia. Topology and robustness in the drosophila segment polarity network. *PLoS Biol*, 2(6):e123, 2004.

[75] Harry V Isaacs, Anne E Deconinck, and Mary E Pownall. Fgf4 regulates blood and muscle specification in xenopus laevis. *Biol Cell*, 99(3):165–73, Mar 2007.

[76] S Ishihara, K Fujimoto, and T Shibata. Cross talking of network motifs in gene regulation that generates temporal pulses and spatial stripes. *Genes Cells*, 10(11):1025–38, 2005.

[77] S Ishihara and T Shibata. Mutual interaction in network motifs robustly sharpens gene expression in developmental processes. *J Theor Biol*, 252(1):131–44, 2008.

[78] Eri Ishiko, Itaru Matsumura, Sachiko Ezoe, Karin Gale, Jun Ishiko, Yusuke Satoh, Hirokazu Tanaka, Hirohiko Shibayama, Masao Mizuki, Takumi Era, Tariq Enver, and Yuzuru Kanakura. Notch signals inhibit the development of erythroid/megakaryocytic cells by suppressing gata-1 activity through the induction of hes1. *J Biol Chem*, 280(6):4929–39, Feb 2005.

[79] T Isshiki, B Pearson, S Holbrook, and CQ Doe. Drosophila neuroblasts sequentially express transcription factors which specify the temporal identity of their neuronal progeny. *Cell*, 106(4):511–21, 2001.

[80] J Jaeger, M Blagov, D Kosman, KN Kozlov, Manu, E Myasnikova, S Surkova, CE Vanario-Alonso, M Samsonova, DH Sharp, and J Reinitz. Dynamical analysis of regulatory interactions in the gap gene system of drosophila melanogaster. *Genetics*, 167(4):1721–37, 2004.

[81] F Jülicher, K Kruse, J Prost, and JF Joanny. Active behavior of the cytoskeleton. *Physics Reports*, 449(1-3):3–28, 2007.

[82] Jos Käfer, Takashi Hayashi, Athanasius F M Marée, Richard W Carthew, and François Graner. Cell adhesion and cortex contractility determine cell patterning in the drosophila retina. *Proc Natl Acad Sci USA*, 104(47):18549–54, Nov 2007.

[83] R Kambadur, K Koizumi, C Stivers, J Nagle, SJ Poole, and WF Odenwald. Regulation of pou genes by castor and hunchback establishes layered compartments in the drosophila cns. *Genes Dev*, 12(2):246–60, 1998.

[84] MI Kanai, M Okabe, and Y Hiromi. seven-up controls switching of transcription factors that specify temporal identities of drosophila neuroblasts. *Dev Cell*, 8(2):203–13, 2005.

[85] K Kaneko. *Life: an introduction to complex systems biology*. Springer, 2006.

[86] K Kaneko. Evolution of robustness to noise and mutation in gene expression dynamics. *PLoS One*, 2(5):e434, 2007.

[87] K Kaneko and T Yomo. Cell division, differentiation and dynamic clustering. *Physica D*, 75:89–102, Jan 1994.

[88] K Kaneko and T Yomo. Isologous diversification: a theory of cell differentiation. *Bull. Math. Biol.*, Jan 1997.

[89] K Kaneko and T Yomo. Isologous diversification for robust development of cell society. *Journal of Theoretical Biology*, Jan 1999.

[90] R Kay and C Thompson. Cross-induction of cell types in dictyostelium: evidence that dif-1 is made by prespore cells. *Development*, Jan 2001.

[91] VM Kendon, ME Cates, I Pagonabarraga, JC Desplat, and P Bladon. Inertial effects in three-dimensional spinodal decomposition of a symmetric binary fluid mixture: a lattice boltzmann study. *Journal of Fluid Mechanics*, 440:147–203, 2001.

[92] VM Kendon, JC Desplat, P Bladon, and ME Cates. 3d spinodal decomposition in the inertial regime. *Physical Review Letters*, 83(3):576–579, 1999.

[93] T Keyes and I Oppenheim. Bilinear hydrodynamics and the stokes-einstein law. *Physical Review A*, 8(2):937–949, 1973.

[94] H Kitano. Biological robustness. *Nat Rev Genet*, 5(11):826–837, 2004.

[95] A Koseska, E Volkov, A Zaikin, and J Kurths. Inherent multistability in arrays of autoinducer coupled genetic oscillators. *Phys. Rev. E*, Jan 2007.

[96] G Krausch, CA Dai, EJ Kramer, and FS Bates. Real space observation of dynamic scaling in a critical polymer mixture. *Physical Review Letters*, 71(22):3669–3672, 1993.

[97] M Krieg, Y Arboleda-Estudillo, P.-H Puech, J Käfer, F Graner, D. J Müller, and C.-P Heisenberg. Tensile forces govern germ-layer organization in zebrafish. *Nat Cell Biol*, 10(4):429–436, Apr 2008.

[98] A Kunisato, S Chiba, and E Nakagami-Yamaguchi. ... 1 preserves purified hematopoietic stem cells ex vivo and accumulates side population cells .... *Blood*, Jan 2003.

[99] Katharina P Landsberg, Reza Farhadifar, Jonas Ranft, Daiki Umetsu, Thomas J Widmann, Thomas Bittig, Amani Said, Frank Jülicher, and Christian Dahmann. Increased cell bond tension governs cell sorting at the drosophila anteroposterior compartment boundary. *Current Biology*, pages 1–36, Oct 2009.

[100] M Laradji, S Toxvaerd, and OG Mouritsen. Molecular dynamics simulation of spinodal decomposition in three-dimensional binary fluids. *Physical Review Letters*, 77(11):2253–2256, 1996.

[101] KY Lau, S Ganguli, and C Tang. Function constrains network architecture and dynamics: a case study on the yeast cell cycle boolean network. *Phys Rev E*, 75(5 Pt 1):051907, 2007.

[102] M Levin and E Davidson. Gene regulatory networks for development. *Proc Natl Acad Sci USA*, 102(14):4936–4942, 2005.

[103] F Li, T Long, Y Lu, Q Ouyang, and C Tang. The yeast cell-cycle network is robustly designed. *Proc Natl Acad Sci USA*, 101(14):4781–6, 2004.

[104] H Li and A Popadic. Analysis of nubbin expression patterns in insects. *Evolution & Development*, 6(5):310–324, 2004.

[105] I Lifshitz. The kinetics of precipitation from supersaturated solid solutions. *Journal of Physics and Chemistry of Solids*, Jan 1961.

[106] PZ Liu and TC Kaufman. Kruppel is a gap gene in the intermediate germband insect oncopeltus fasciatus and is required for development of both blastoderm and germ band-derived segments. *Development*, 131(18):4567–4579, 2004.

[107] M Loose and R Patient. A genetic regulatory network for xenopus mesendoderm formation. *Developmental Biology*, Jan 2004.

[108] K Luo, W Gronski, and C Friedrich. Morphology and dynamics of phase-separating fluids with viscosity asymmetry. *Macromolecular Theory and Simulations*, 13(4):365–373, 2004.

[109] W Ma, L Lai, Q Ouyang, and C Tang. Robustness and modular design of the drosophila segment polarity network. *Mol Syst Biol*, 2:70, 2006.

[110] H Maamar, A Raj, and D Dubnau. Noise in gene expression determines cell fate in bacillus subtilis. *Science*, Jan 2007.

[111] TT Maeda, I Ajioka, and K Nakajima. Computational cell model based on autonomous cell movement regulated by cell-cell signalling successfully recapitulates the" inside and outside" pattern of cell sorting. *BMC Systems Biology*, 1(1):43, 2007.

[112] EK Mann, S Henon, D Langevin, J Meunier, and L Léger. Hydrodynamics of domain relaxation in a polymer monolayer. *Phys. Rev. E*, 51(6):5708–5720, 1995.

[113] Manu, S Surkova, AV Spirov, VV Gursky, H Janssens, AR Kim, O Radulescu, CE Vanario-Alonso, DH Sharp, M Samsonova, and J Reinitz. Canalization of gene expression and domain shifts in the drosophila blastoderm by dynamical attractors. *PLoS Comput Biol*, 5(3):e1000303, 2009.

[114] AFM Maree, VA Grieneisen, and P Hogeweg. Ii. 2 the cellular potts model and biophysical properties of cells, tissues and morphogenesis. *Single-cell-based models in biology and medicine*, page 107, 2007.

[115] AFM Marée and P Hogeweg. How amoeboids self-organize into a fruiting body: Multicellular coordination in dictyostelium discoideum. *Proceedings of the National Academy of Sciences*, 98(7):3879, 2001.

[116] HH McAdams and A Arkin. Simulation of prokaryotic genetic circuits. *Annu Rev Biophys Biomol Struct*, 27:199–224, 1998.

[117] D McMillen, N Kopell, J Hasty, and J Collins. Synchronizing genetic relaxation oscillators by intercell signaling. *Proceedings of the National Academy of Sciences of the . . .* , Jan 2002.

[118] R Merks, S Brodsky, M Goligorksy, S Newman, and J Glazier. Cell elongation is key to in silico replication of in vitro vasculogenesis and subsequent remodeling. *Developmental Biology*, 289(1):44–54, Jan 2006.

[119] U Mettler, G Vogler, and J Urban. Timing of identity: spatiotemporal regulation of hunchback in neuroblast lineages of drosophila by seven-up and prospero. *Development*, 133(3):429–37, 2006.

[120] M San Miguel, M Grant, and JD Gunton. Phase separation in two-dimensional binary fluids. *Physical Review A*, 31(2):1001–1005, 1985.

[121] R Milo, S Itzkovitz, N Kashtan, R Levitt, and S Shen-.... Superfamilies of evolved and designed networks. *Science*, Jan 2004.

[122] R Milo, S Shen-Orr, S Itzkovitz, and N Kashtan. Network motifs: Simple building blocks of complex networks. *Science*, Jan 2002.

[123] T Mizuguchi and M Sano. Proportion regulation of biological cells in globally coupled nonlinear systems. *Physical Review Letters*, Jan 1995.

[124] A Mochizuki, Y Iwasa, and Y Takeda. A stochastic model for cell sorting and measuring cell–cell adhesion. *Journal of Theoretical Biology*, 179(2):129–146, 1996.

[125] J Mombach, J Glazier, and R Raphael. ... differential adhesion models and cell sorting in the presence and absence of fluctuations. *Physical Review Letters*, Jan 1995.

[126] JCM Mombach and JA Glazier. Single cell motion in aggregates of embryonic cells. *Phys Rev Lett*, 76:3032, 1996.

[127] JCM Mombach, D Robert, F Graner, G Gillet, GL Thomas, M Idiart, and JP Rieu. Rounding of aggregates of biological cells: Experiments and simulations. *Physica A: Statistical Mechanics and its Applications*, 352(2-4):525–534, 2005.

[128] T Murakami, T Hijikata, M Matsukawa, H Ishikawa, and H Yorifuji. Zebrafish protocadherin 10 is involved in paraxial mesoderm development and somitogenesis. *Dev. Dyn.*, 235(2):506–514, 2006.

[129] J Newport and M Kirschner. A major developmental transition in early xenopus embryos: I. characterization and timing of .... *Cell*, Jan 1982.

[130] J Newport and M Kirschner. A major developmental transition in early xenopus embryos: Ii. control of the onset of .... *Cell*, Jan 1982.

[131] E Nigg. Mitotic kinases as regulators of cell division and its checkpoints. *Nat Rev Mol Cell Biol*, Jan 2001.

[132] B Novak. Numerical analysis of a comprehensive model of m-phase control in xenopus oocyte extracts and intact .... *Journal of Cell Science*, Jan 1993.

[133] KE Novik and PV Coveney. Spinodal decomposition of off-critical quenches with a viscous phase using dissipative particle dynamics in two and three spatial dimensions. *Phys. Rev. E*, 61(1):435–448, 2000.

[134] T Novotny, R Eiselt, and J Urban. Hunchback is required for the specification of the early sublineage of neuroblast 7-3 in the drosophila central nervous system. *Development*, 129(4):1027–36, 2002.

[135] N Ouchi, J Glazier, J Rieu, A Upadhyaya, and Y Sawada. Improving the realism of the cellular potts model in simulations of biological cells. *Physica A: Statistical Mechanics and its Applications*, 329(3-4):451–458, Nov 2003.

[136] N Oviedo, P Newmark, and A Sanchez .... Allometric scaling and proportion regulation in the freshwater planarian schmidtea .... *Dev. Dyn.*, Jan 2003.

[137] E Palsson and HG Othmer. A model for individual and collective cell movement in dictyosteliumdiscoideum. *Proceedings of the National Academy of Sciences*, 97(19):10448, 2000.

[138] Ewa Paluch and Carl-Philipp Heisenberg. Biology and physics of cell shape changes in development. *Current Biology*, 19(17):R790–R799, Jan 2009.

[139] N H Patel, D C Hayward, S Lall, N R Pirkl, D DiPietro, and E E Ball. Grasshopper hunchback expression reveals conserved and novel aspects of axis formation and segmentation. *Development*, 128(18):3459–72, 2001.

[140] BJ Pearson and CQ Doe. Specification of temporal identity in the developing nervous system. *Annu Rev Cell Dev Biol*, 20:619–47, 2004.

[141] Aimin Peng, Andrea L Lewellyn, and James L Maller. Undamaged dna transmits and enhances dna damage checkpoint signals in early embryos. *Mol Cell Biol*, 27(19):6852–62, Oct 2007.

[142] TJ Perkins, J Jaeger, J Reinitz, and L Glass. Reverse engineering the gap gene network of drosophila melanogaster. *PLoS Comput Biol*, 2(5):e51, 2006.

[143] F Perrot, P Guenoun, T Baumberger, D Beysens, Y Garrabos, and B Le Neindre. Nucleation and growth of tightly packed droplets in fluids. *Physical Review Letters*, 73(5):688–691, 1994.

[144] R Phillips, J Kondev, and J Theriot. *Physical biology of the cell*. Garland Science, 2008.

[145] Jamie Pinnell, Paul S Lindeman, Sierra Colavito, Chris Lowe, and Robert M Savage. The divergent roles of the segmentation gene hunchback. *Integr Comp Biol*, 46(4):519–532, 2006.

[146] M Poujade, E Grasland-Mongrain, A Hertzog, J Jouanneau, P Chavrier, B Ladoux, A Buguin, and P Silberzan. Collective migration of an epithelial monolayer in response to a model wound. *Proc Natl Acad Sci USA*, 104(41):15988–93, Oct 2007.

[147] S Puri and B Dünweg. Temporally linear domain growth in the segregation of binary fluids. *Physical Review A*, 45(10):6977–6980, 1992.

[148] Freddy Radtke, Anne Wilson, Stephane J C Mancini, and H Robson Macdonald. Notch regulation of lymphocyte development and function. *Nat Immunol*, 5(3):247–53, Mar 2004.

[149] I Ràfols, A Amagai, Y Maeda, H K MacWilliams, and Y Sawada. Cell type proportioning in dictyostelium slugs: lack of regulation within a 2.5-fold tolerance range. *Differentiation*, 67(4-5):107–16, Jun 2001.

[150] W Rappel, A Nicol, A Sarkissian, and H Levine. Self-organized vortex state in two-dimensional dictyostelium dynamics. *Physical Review Letters*, Jan 1999.

[151] Frédérique Marie Rattis, Carlijn Voermans, and Tannishtha Reya. Wnt signaling in the stem cell niche. *Curr Opin Hematol*, 11(2):88–94, Mar 2004.

[152] Matteo Rauzi, Pascale Verant, Thomas Lecuit, and Pierre-François Lenne. Nature and anisotropy of cortical forces orienting drosophila tissue morphogenesis. *Nat Cell Biol*, 10(12):1401–10, Dec 2008.

[153] L Rayleigh. On the capillary phenomena of jets. *Proceedings of the Royal Society of London*, Jan 1879.

[154] L Rayleigh. On the instability of cylindrical fluid surfaces. *Philosophical Magazine*, 34:145, 1892.

[155] JP Rieu, N Kataoka, and Y Sawada. Quantitative analysis of cell motion during sorting in two-dimensional aggregates of dissociated hydra cells. *Phys. Rev. E*, 57(1):924–931, 1998.

[156] JP Rieu and Y Sawada. Hydrodynamics and cell motion during the rounding of two dimensional hydra cell aggregates. *Eur. Phys. J. B*, 27(1):167–172, 2002.

[157] TM Rogers and RC Desai. Numerical study of late-stage coarsening for off-critical quenches in the cahn-hilliard equation of phase separation. *Physical Review B*, 39(16):11956–11964, 1989.

[158] TM Rogers, KR Elder, and RC Desai. Numerical study of the late stages of spinodal decomposition. *Physical Review B*, 37(16):9638–9649, 1988.

[159] C Roland and M Grant. Monte carlo renormalization-group study of spinodal decomposition: Scaling and growth. *Physical Review B*, Jan 1989.

[160] M Sato-Maeda, M Uchida, and F Graner. Quantitative evaluation of tissue-specific cell adhesion at the level of a single cell pair. *Developmental Biology*, 1994.

[161] NJ Savill and P Hogeweg. Modelling morphogenesis: from single cells to crawling slugs. *Journal of Theoretical Biology*, 184(3):229–235, 1997.

[162] Eva-Maria Schoetz. *Dynamics and Mechanics of Zebrafish Embryonic Tissues*. VDM Verlag, 2008.

[163] Eva-Maria Schötz, Rebecca D Burdine, Frank Jülicher, Malcolm S Steinberg, Carl-Philipp Heisenberg, and Ramsey A Foty. Quantitative differences in tissue surface tension influence zebrafish germ layer positioning. *HFSP J.*, 2(1):42, Jan 2008.

[164] MD Schroeder, M Pearce, J Fak, H Fan, U Unnerstall, E Emberly, N Rajewsky, ED Siggia, and U Gaul. Transcriptional control in the segmentation gene network of drosophila. *PLoS Biol*, 2(9):E271, 2004.

[165] Wei Sha, Jonathan Moore, Katherine Chen, Antonio D Lassaletta, Chung-Seon Yi, John J Tyson, and Jill C Sible. Hysteresis drives cell-cycle transitions in xenopus laevis egg extracts. *Proc Natl Acad Sci USA*, 100(3):975–80, Feb 2003.

[166] Shai S Shen-Orr, Ron Milo, Shmoolik Mangan, and Uri Alon. Network motifs in the transcriptional regulation network of escherichia coli. *Nat. Genet.*, 31(1):64–8, May 2002.

[167] Ken Shimuta, Nobushige Nakajo, Katsuhiro Uto, Yoshimasa Hayano, Kenji Okazaki, and Noriyuki Sagata. Chk1 is activated transiently and targets cdc25a for degradation at the xenopus midblastula transition. *EMBO J*, 21(14):3694–703, Jul 2002.

[168] A Shinozaki and Y Oono. Spinodal decomposition in 3-space. *Phys. Rev. E*, 48(4):2622–2654, 1993.

[169] E Siggia. Late stages of spinodal decomposition in binary mixtures. *Physical Review A*, Jan 1979.

[170] P Smolen, DA Baxter, and JH Byrne. Modeling transcriptional control in gene networks–methods, recent results, and future directions. *Bull Math Biol*, 62(2):247–92, 2000.

[171] H J Standley, A M Zorn, and J B Gurdon. eFGF and its mode of action in the community effect during Xenopus myogenesis. *Development*, 128(8):1347–57, Apr 2001.

[172] M Steinberg. Differential adhesion in morphogenesis: a modern view. *Current Opinion in Genetics & Development*, 17(4):281–286, Aug 2007.

[173] M S Steinberg. Mechanism of tissue reconstruction by dissociated cells. II. time-course of events. *Science*, 137:762–3, 1962.

[174] M S Steinberg. On the mechanism of tissue reconstruction by dissociated cells. I. population kinetics, differential adhesiveness. and the absence of directed migration. *Proc Natl Acad Sci USA*, 48:1577–82, 1962.

[175] M S Steinberg. On the mechanism of tissue reconstruction by dissociated cells. III. free energy relations and the reorganization of fused, heteronomic tissue fragments. *Proc Natl Acad Sci USA*, 48(10):1769–76, 1962.

[176] A Stollewerk and P Simpson. Evolution of early development of the nervous system: a comparison between arthropods. *Bioessays*, 27(9):874–883, 2005.

[177] Gürol M Süel, Jordi Garcia-Ojalvo, Louisa M Liberman, and Michael B Elowitz. An excitable gene regulatory circuit induces transient cellular differentiation. *Nature*, 440(7083):545–50, Mar 2006.

[178] Gemma Swiers, Roger Patient, and Matthew Loose. Genetic regulatory networks programming hematopoietic stem cells and erythroid lineage specification. *Developmental Biology*, 294(2):525–40, Jun 2006.

[179] L Snchez and D Thieffry. Segmenting the fly embryo: a logical analysis of the pair-rule cross-regulatory module. *J Theor Biol*, 224(4):517–37, 2003.

[180] Tetsuya Tabata and Yuki Takei. Morphogens, their identification and regulation. *Development*, 131(4):703–12, Feb 2004.

[181] GM Technau, C Berger, and R Urbach. Generation of cell diversity and segmental pattern in the embryonic central nervous system of drosophila. *Dev Dyn*, 235(4):861–9, 2006.

[182] U Technau and TW Holstein. Cell sorting during the regeneration of hydra from reaggregated cells. *Developmental biology(Print)*, 151(1):117–127, 1992.

[183] CS Thummel. Molecular mechanisms of developmental timing in c. elegans and drosophila. *Dev Cell*, 1(4):453–65, 2001.

[184] S Tomotika. On the instability of a cylindrical thread of a viscous liquid surrounded by another .... *Proceedings of the Royal Society of London. Series A*, Jan 1935.

[185] KD Tran and CQ Doe. Pdm and castor close successive temporal identity windows in the nb3-1 lineage. *Development*, 135(21):3491–9, 2008.

[186] J Trinkaus and P Groves. Differentiation in culture of mixed aggregates of dissociated tissue cells. *Proceedings of the National Academy of Sciences*, Jan 1955.

[187] John J Tyson, Katherine C Chen, and Bela Novak. Sniffers, buzzers, toggles and blinkers: dynamics of regulatory and signaling pathways in the cell. *Current Opinion in Cell Biology*, 15(2):221–31, Apr 2003.

[188] Ekkehard Ullner, Alexei Zaikin, Evgenii I Volkov, and Jordi García-Ojalvo. Multistability and clustering in a population of synthetic genetic oscillators via phase-repulsive cell-to-cell communication. *Physical Review Letters*, 99(14):148103, Oct 2007.

[189] OT Valls and JE Farrell. Spinodal decomposition in a three-dimensional fluid model. *Phys. Rev. E*, 47(1):36–39, 1993.

[190] T Vicsek, A Czirók, E Ben-Jacob, and I Cohen. Novel type of phase transition in a system of self-driven particles. *Physical Review Letters*, Jan 1995.

[191] G von Dassow, E Meir, EM Munro, and GM Odell. The segment polarity network is a robust developmental module. *Nature*, 406(6792):188–92, 2000.

[192] C H. Waddington. *The Strategy of the Genes: A Discussion of some Aspects of theoretical Biology*. George Allen & Unwin, 1957.

[193] A Wagner. Circuit topology and the evolution of robustness in two-gene circadian oscillators. *Proc Natl Acad Sci USA*, 102(33):11775–80, 2005.

[194] Jeffrey G Williams. Transcriptional regulation of dictyostelium pattern formation. *EMBO Rep*, 7(7):694–8, Jul 2006.

[195] C Wolff, R Sommer, R Schröder, G Glaser, and D Tautz. Conserved and divergent expression aspects of the drosophila segmentation gene hunchback in the short germ band embryo of the flour beetle tribolium. *Development*, 121(12):4227–36, 1995.

[196] NC Wong and CM Knobler. Light scattering studies of phase separation in isobutyric acid+ water mixtures. *The Journal of Chemical Physics*, 69:725, 1978.

[197] NC Wong and CM Knobler. Light-scattering studies of phase separation in isobutyric acid+ water mixtures: Hydrodynamic effects. *Physical Review A*, 24(6):3205–3211, 1981.

[198] R H Xu, K T Ault, J Kim, M J Park, Y S Hwang, Y Peng, D Sredni, and H f Kung. Opposite effects of fgf and bmp-4 on embryonic blood formation: roles of pv.1 and gata-2. *Developmental Biology*, 208(2):352–61, Apr 1999.

[199] JH Yao, KR Elder, H Guo, and M Grant. Theory and simulation of ostwald ripening. *Physical Review B*, 47(21):14110–14125, 1993.

[200] G K Yasuda and G Schubiger. Temporal regulation in the early embryo: is mbt too good to be true? *Trends Genet*, 8(4):124–7, Apr 1992.

[201] M Zajac, GL Jones, and JA Glazier. Simulating convergent extension by way of anisotropic differential adhesion. *Journal of Theoretical Biology*, 222(2):247–259, 2003.